# ENHANCED REMOVAL OF PHARMACEUTICALS AND PERSONAL CARE PRODUCTS (PPCPs) USING SUNLIGHT-DRIVEN PHOTOCATALYST (g-C<sub>3</sub>N<sub>4</sub>/BiNbO<sub>4</sub>)

# PHUAH ZI SONG

UNIVERSITI TUNKU ABDUL RAHMAN

# ENHANCED REMOVAL OF PHARMACEUTICALS AND PERSONAL CARE PRODUCTS (PPCPs) USING SUNLIGHT-DRIVEN PHOTOCATALYST (g-C<sub>3</sub>N<sub>4</sub>/BiNbO<sub>4</sub>)

#### PHUAH ZI SONG

A project report submitted in partial fulfilment of the requirements for the award of the degree of Bachelor of Civil Engineering (Environmental) with Honours

Faculty of Engineering and Green Technology
Universiti Tunku Abdul Rahman

#### **DECLARATION**

I hereby declare that this project report is based on my original work except for citations and quotations which have been duly acknowledged. I also declare that it has not been previously and concurrently submitted for any other degree or award at UTAR or other institutions.

Signature:

Name : PHUAH ZI SONG

ID No. : 20AGB03541

Date : 30 April 2025

iii

APPROVAL FOR SUBMISSION

I certify that this project report entitled "ENHANCED REMOVAL OF

PHARMACEUTICALS AND PERSONAL CARE PRODUCTS (PPCPs) USING

SUNLIGHT-DRIVEN PHOTOCATALYST (g-C<sub>3</sub>N<sub>4</sub>/BiNbO<sub>4</sub>)" was prepared by

PHUAH ZI SONG has met the required standard for submission in partial fulfilment

of the requirements for the award of Bachelor of Civil Engineering (Environmental)

with Honours at Universiti Tunku Abdul Rahman.

Approved by,

Signature :

Supervisor: Ir. Ts. Dr. Leong Kah Hon

Date : 30 April 2025

The copyright of this report belongs to the author under the terms of the copyright Act 1987 as qualified by Intellectual Property Policy of Universiti Tunku Abdul Rahman. Due acknowledgement shall always be made of the use of any material contained in, or derived from, this report.

© 2025, Phuah Zi Song. All right reserved.

#### **ACKNOWLEDGEMENTS**

I wish to extend my deepest thanks to everyone whose support has been instrumental in the successful completion of this project. I am especially grateful to Universiti Tunku Abdul Rahman for providing both the opportunity to undertake this research and the essential facilities that enabled its efficient execution. It has been a privilege to meet so many kind-hearted individuals and professionals who offered their guidance throughout my journey.

I would like to express my heartfelt appreciation to my final year project supervisor, Ir. Ts. Dr. Leong Kah Hon. Despite his demanding schedule, he generously devoted time to listen, advise, and steer me in the right direction, ensuring that I could complete my project successfully. I also owe a great debt of gratitude to my moderator, ChM. Ts. Dr. Lam Sze Mun, and my academic advisor Chm. Dr. Wong Lai Peng for their patient guidance and invaluable insights.

I am forever indebted to my parents, whose unwavering support and belief in my abilities have given me the courage to overcome life's challenges and strive beyond my limits.

Finally, my sincere thanks go to all the lab officers—Ms. Amelia Ng Suk Ting, Ms. Nor Raihanah Binti Rahani, Puan Nurul Hidayah, Mr. Yong Tzyy Jeng, Puan Ropidah Hamimi Binti Mohd Zain, and Mr. Tamilvanan A/L Muniandi—for their technical assistance during my research, as well as to my friends for their words of encouragement in times of hardship, with a special mention to my senior, Camelia Ng Choi Lam, whose guidance was particularly invaluable.

# ENHANCED REMOVAL OF PHARMACEUTICALS AND PERSONAL CARE PRODUCTS (PPCPs) USING SUNLIGHT-DRIVEN PHOTOCATALYST (g-C<sub>3</sub>N<sub>4</sub>/BiNbO<sub>4</sub>)

#### **ABSTRACT**

Oxytetracycline (OTC) is increasingly recognized as an emerging contaminant among pharmaceuticals and personal care products (PPCPs), posing significant risks to both human health and the environment by potentially disrupting the central nervous and digestive systems. Conventional treatment methods have proven inadequate for degrading OTC due to its unique chemical properties. This study investigates the degradation of OTC using a g-C<sub>3</sub>N<sub>4</sub>/BiNbO<sub>4</sub> composite photocatalyst. The photocatalyst was comprehensively characterized by FESEM-EDX, XRD, FTIR, and UV-Vis DRS to examine its morphology, elemental composition, microstructure, crystal structure, functional groups, and bandgap energy. FTIR analysis confirmed the presence of functional groups such as O-H, C-N, and C=N within the composite. UV-Vis DRS analysis determined the bandgap energies of pure BiNbO<sub>4</sub> and the optimized g-C<sub>3</sub>N<sub>4</sub>/BiNbO<sub>4</sub> composite to be 2.87 eV and 2.85 eV, respectively. Moreover, photocatalytic experiments revealed that the composite containing 0.3g-C<sub>3</sub>N<sub>4</sub>/BiNbO<sub>4</sub> achieved an impressive removal efficiency of 98% within 180 minutes. These findings underscore the potential of the g-C<sub>3</sub>N<sub>4</sub>/BiNbO<sub>4</sub> photocatalyst as an environmentally friendly solution for degrading various organic pollutants under sunlight irradiation.

Keywords: Oxytetracycline, emerging contaminants, g-C<sub>3</sub>N<sub>4</sub>/BiNbO<sub>4</sub> composite, UV–Vis diffuse reflectance spectroscopy (UV-Vis DRS), bandgap energy

Subject area: QD701-731 Photochemistry

## TABLE OF CONTENTS

DECLARA	ATION		ii
APPROVA	L FOR S	SUBMISSION	iii
ACKNOW	LEDGE	MENTS	v
ABSTRAC	CT		vi
TABLE O	F CONTI	ENTS	vii
LIST OF T	<b>TABLES</b>		ix
LIST OF F	FIGURES		X
LIST OF S	SYMBOL	S / ABBREVIATIONS	xiii
LIST OF A	APPEND	ICES	xvi
СНАРТЕ	₹		
	.•		
4	INTER	ODUCTION	
1		ODUCTION	1
	1.1	Background Study	1
	1.2	Problem Statement	4
	1.3	Aims and Objectives	5
	1.4	Scope of Study	5
2	LITE	RATURE REVIEW	6
	2.1	Pharmaceuticals and Personal Care Products (P	PCPs) 6
		2.1.1 Oxytetracycline (OTC)	7
	2.2	Conventional Treatment Method	9
	2.3	Advanced Oxidation Process	11
	2.4	Photocatalysis	12
	2.5	Heterojunction Photocatalyst	15
		2.5.1 BiNbO <sub>4</sub> Coupled with g-C <sub>3</sub> N <sub>4</sub>	16

			viii
	2.6	Sustainable Development Goal (SDGs)	18
	2.7	Summary	23
3	RESE	ARCH METHODOLOGY	25
	3.1	Materials	26
	3.2	Apparatus	27
	3.3	Synthesis of BiNbO <sub>4</sub>	28
	3.4	Synthesis of g-C <sub>3</sub> N <sub>4</sub>	28
	3.5	Coupling of g-C <sub>3</sub> N <sub>4</sub> / BiNbO <sub>4</sub>	29
	3.6	Characterisation	30
	3.7	Photocatalytic Degradation of Oxytetracycline (OTC)	32
	3.8	Detection of Active Radical Species	33
	3.9	Stability of Photocatalyst	33
4	RESU	LTS AND DISCUSSION	34
	4.1 Ch	aracterization of GCN/BNO Coupled Photocatalysts	34
		4.1.1 FESEM-EDX Analysis	34
		4.1.2 X-Ray Diffraction Analysis	44
		4.1.3 FTIR Analysis	46
		4.1.4 UV-Vis DRS Analysis	48
	4.2	Photocatalytic Degradation of OTC under Sunlight	50
	4.3	Degradation Kinetics Model	52
	4.4	Determination of Active Radical Species	53
	4.5	Cycling Test	55
	4.6	Charge Transfer Mechanism	56
	4.7	Operational Cost Estimation	58
5	CONC	CLUSION	59
	5.1	Conclusion	59
	5.2	Recommendations	60
REFI	ERENC	ES	61
APPE	ENDICE	CS	70

# LIST OF TABLES

TABLE	PAGE	
2.1	Various Photocatalyst Used for Degrading OTC	8
2.2	Various Conventional Treatment Method for OTC Removal	10
3.1	List of Materials Used in This Study	26
3.2	List of Equipment Used in This Study	27
3.3	Characterisation for g-C <sub>3</sub> N <sub>4</sub> / BiNbO <sub>4</sub>	30
4.1	Cost Estimation of g-C <sub>3</sub> N <sub>4</sub> for synthesising 0.3GCN/BNO	58
4.2	Cost Estimation of BiNbO <sub>4</sub> for synthesising 0.3GCN/BNO	58
5.1	$g\text{-}C_3N_4$ based heterojunction for the removal of tetracycline	70
5.2	Comparison of OTC degradation by using various photocatalyst	71

# LIST OF FIGURES

FIGURE	TITLE	PAGE
1.1	The Structure of g-C <sub>3</sub> N <sub>4</sub>	3
1.2	Band Structures of BiNbO <sub>4</sub>	4
2.1	Oxytetracycline, OTC	7
2.2	Schematic of Photocatalytic Activity Mechanism	12
2.3	Band Gap on Different Types of Materials	13
2.4	Different possibilities of reactions. (A) Reduction. (B) Oxidation. (C) Redox (D) No reaction	14
2.5	Design and fabrication of heterojunction photocatalysts for energy conversion and pollutant degradation	15
2.6	Phase Change of BiNbO <sub>4</sub>	17
2.7	SDG 3	18
2.8	SDG 6	19
2.9	SDG 9	20
2.10	SDG 12	21
2.11	SDG 14	22
3.1	Flow Chart of Experimental Methodologies	25
4.1	FESEM Image of g-C <sub>3</sub> N <sub>4</sub> with 5,000 magnifications	35
4.2	FESEM Image of g-C <sub>3</sub> N <sub>4</sub> with 10,000 magnifications	36

4.3	a) EDX Analysis of g-C <sub>3</sub> N <sub>4</sub> ; b) Element mapping of C; c) Element mapping of N.	36
4.4	FESEM Image of BiNbO <sub>4</sub> with 5,000 magnifications	37
4.5	FESEM Image of BiNbO <sub>4</sub> with 10,000 magnifications	38
4.6	a) EDX Analysis of BiNbO <sub>4</sub> ; b) Element mapping of O; c) Element mapping of Bi; d) Element mapping of Nb.	38
4.7	FESEM Image of 0.3 GCN/BNO with 5,000 magnifications	39
4.8	FESEM Image of 0.3 GCN/BNO with 10,000 magnifications	40
4.9	FESEM Image of 0.5 GCN/BNO with 5,000 magnifications	40
4.10	FESEM Image of 0.5 GCN/BNO with 10,000 magnifications	41
4.11	FESEM Image of 0.7 GCN/BNO with 5,000 magnifications	41
4.12	FESEM Image of 0.7 GCN/BNO with 10,000 magnifications	42
4.13	a) EDX Analysis of 0.3 GCN/BNO; b) Element mapping of C; c) Element mapping of N; d) Element mapping of O; e) Element mapping of Bi; f) Element mapping of Nb	42
4.14	a) EDX Analysis of 0.5 GCN/BNO; b) Element mapping of C; c) Element mapping of N; d) Element mapping of O; e) Element mapping of Bi; f) Element mapping of Nb	43
4.15	a) EDX Analysis of 0.7 GCN/BNO; b) Element mapping of C; c) Element mapping of N; d) Element mapping of O; e) Element mapping of Bi; f) Element mapping of Nb	43
4.16	XRD patterns of Pure BNO, Pure GCN, and Different Ratio of GCN/BNO	45

4.17	Different Ratio of GCN/BNO	47
4.18	(a) UV-Vis DRS Spectrum of GCN, BNO, and composites of GCN/BNO and (b) Band Gap by Tauc Plot	49
4.19	Dark reaction for 20ppm OTC	51
4.20	Light reaction for 20ppm OTC	51
4.21	Non-linear kinetic models for the degradation of OTC using 0.3GCN/BNO	52
4.22	Effect of scavenging agent on degradation of OTC	54
4.23	Result for Three Cycling Tests using 0.3GCN/BNO	55
4.24	Schematic diagram of charge transfer in $g$ - $C_3N_4/BiNbO_4$ heterostructures under visible light irradiation	57
5.1	Synthesis of $g\text{-}C_3N_4$ from urea using calcination method	72
5.2	Synthesis of BiNbO <sub>4</sub> using simple solvothermal method	73
5.3	Coupling of g-C3N4 and BiNbO4 using simple physical mixing method	73

#### LIST OF SYMBOLS / ABBREVIATIONS

°C degree Celsius

eV electron volt

nm nanometre

mL millilitre

ms<sup>-1</sup> millimetre per second

mgL<sup>-1</sup> milligram per litre

rpm revolutions per minute

mM millimolar

M molar

ppm parts per million

rpm revolutions per minute

wt.% weight percentage

C carbon

N nitrogen

O oxygen

Nb niobium

Bi bismuth

H<sub>2</sub>O water

CO<sub>2</sub> carbon dioxide

TiO<sub>2</sub> titanium dioxide

g-C<sub>3</sub>N<sub>4</sub> graphitic carbon nitride

BiNbO<sub>4</sub> bismuth niobate

Bi<sub>5</sub>Nb<sub>3</sub>O<sub>15</sub> bismuth niobium oxide

Bi(NO<sub>3</sub>)<sub>3</sub>.5H<sub>2</sub>O bismuth (III) nitrate pentahydrate

Nb<sub>2</sub>O<sub>5</sub> niobium pentoxide

NbO<sub>6</sub> niobium (VI) oxide

C<sub>2</sub>H<sub>3</sub>NaO<sub>2</sub> sodium acetate anhydrous

HNO<sub>3</sub> nitric acid

K<sub>2</sub>Cr<sub>2</sub>O<sub>7</sub> potassium dichromate

•OH hydroxyl radicals

e<sup>-</sup> electron

h<sup>+</sup> hole

C–N nitrile functional group

N–H amine

O–H hydroxyl functional group

C-NH-C amine

 $R_{\infty}$  diffuse reflectance at a specific wavelength

 $\alpha$  absorption coefficient

h Plank's constant

v light frequency

A proportional constant

 $E_g$  band gap energy

C speed of light

 $\lambda$  wavelength

 $q_t$  adsorption capacity

 $C_i$  initial concentration

*C<sub>e</sub>* equilibrium concentration

V volume

m mass of absorbent

R<sup>2</sup> correlation coefficient

 $x^2$  chi-square

PPCPs pharmaceuticals and personal care products

OTC oxytetracycline

AOPs advanced oxidation processes

UV ultraviolet

AC activated carbon

VB valence band

CB conduction band

BG band gap

EG ethylene glycol

PEG polyethylene glycol

IPA isopropyl alcohol

BQ p-Benzoquinone

TEA triethylamine

SDGs sustainable development goals

FESEM field emission scanning electron microscopy

EDX energy dispersive x-ray spectroscopy

HRTEM high-resolution transmission electron microscopy

XRD X-ray diffraction

FTIR Fourier transform infrared spectroscopy

UV-Vis DRS ultraviolet-visible diffuse reflectance spectroscopy

EDS energy dispersive spectroscope

SAED selected area electron diffraction

PL photoluminescence

ICDD International Centre for Diffraction Data

## LIST OF APPENDICES

APPENDIX		TITLE	PAGE
A	Tables		70
В	Figures		72

#### **CHAPTER 1**

#### INTRODUCTION

#### 1.1 Background Study

Recent decades have seen significant advancements in the science and technology sectors. As a result, concerns over environmental issues linked to water pollution from pharmaceuticals and personal care products (PPCPs) have grown, driven by the widespread use of these substances. Various PPCPs, including oxytetracycline (OTC), have been found in water sources, with much of them being discharged into aquatic environments. OTC, a commonly used antibiotic for treating bacterial infections in both humans and animals, is only partially absorbed by the body, with the remainder entering water bodies. The presence of OTC in water poses risks to humans and other organisms due to its toxicity, potential for bioaccumulation, and persistence. Prolonged exposure can lead to antibiotic resistance and ecological disruption (Kim et al., 2021). Unfortunately, conventional treatment methods struggle to effectively remove OTC because of its complex molecular structure, highlighting the urgent need for innovative treatments with high removal efficiency.

Advanced oxidation processes (AOPs) offer highly efficient techniques for breaking down organic pollutants by generating reactive radicals, such as hydroxyl radicals (•OH), which are powerful oxidizers that break down pollutants into water (H<sub>2</sub>O) and carbon dioxide (CO<sub>2</sub>) under sunlight. Heterogeneous photocatalysis is a widely recognized, eco-friendly, cost-effective, non-toxic, and stable approach for removing various organic contaminants using photocatalysts (Wang et al., 2020). Although titanium dioxide (TiO<sub>2</sub>) has been commonly used as a photocatalyst, it has

several drawbacks, including limited activity in the UV region, a high recombination rate, and a tendency to agglomerate, prompting the need for alternative photocatalysts (Hu et al., 2019).

Graphitic carbon nitride (g-C<sub>3</sub>N<sub>4</sub>) is a polymer semiconductor photocatalyst that contains both chemical and thermal stability. It is well known for its abundant resources and desirable photocatalytic performance, as it is composed of plentiful carbon and nitrogen elements and can be efficiently produced in large quantities using affordable precursors such as urea, melamine, and thiourea (Low et al., 2014; Zhang et al., 2015). Moreover, its 2.7–2.8 eV band gap and thermal stability up to 600 °C render it highly suitable for a wide range of functional nanomaterial applications (Shiraishi 49 et al., 2014; Fang et al., 2015; Liang et al., 2015; Zhang et al., 2016; Cui et al., 2016). Nonetheless, its photocatalytic performance is hampered by a relatively modest 2.7 eV band gap and a pronounced tendency for photogenerated charge carriers to recombine rapidly (Mamba, et al., 2016). This arises from electron delocalization driven by the intrinsic tri-s-triazine units (Figure 1.1) within the g-C<sub>3</sub>N<sub>4</sub> framework, resulting in increased recombining rate of charge carrier within the structure. To overcome these limitations, coupling g-C<sub>3</sub>N<sub>4</sub> with other semiconductors has been shown to be an effective strategy for increasing its performance.

On the other hand, bismuth niobate (BiNbO<sub>4</sub>) is an effective photocatalyst due to its distinctive features, such as its responsiveness to visible light, attributed to the Bi 6s orbital in the valence band sitting above the O-2p orbital, reducing the band gap and enabling activation under visible light (Luo et al., 2022). BiNbO<sub>4</sub> exists in α or β forms with different lattice structures, band energies, and photocatalytic activities as shown in **Figure 1.2**. The α phase has a band gap range of 2.6 eV-2.8 eV, while the β phase ranges from 3.2 eV to 3.4 eV, and phase transitions can be influenced by synthesis conditions (Alcântara et al., 2018). During phase transitions, derivatives like Bi<sub>5</sub>Nb<sub>3</sub>O<sub>15</sub> and Bi<sub>3</sub>NbO<sub>7</sub> can appear, with structures that promote electron accumulation and reactive sites, leading to superior photocatalytic activity compared to bulk BiNbO<sub>4</sub> (Tahara et al., 2007; Li et al., 2010). Synthesis via citrate sol-gel and calcination at various temperatures demonstrated reversible phase changes, with distinct phases forming at specific temperatures (Zhai et al., 2011; Xu et al., 2013). Optimized synthesis through solvothermal methods, using polyhydroxy alcohol and a coordinating polymer, generated a solar-responsive BiNbO<sub>4</sub> variant featuring a 2.33

eV band gap and outstanding photocatalytic performance (Kiran et al., 2020). Combining BiNbO<sub>4</sub> with g-C<sub>3</sub>N<sub>4</sub> further extended charge-carrier lifetime and increased charge trapping sites, enhancing photocatalytic activity compared to individual materials.

In this study, the performance of the coupled photocatalysts (g-C<sub>3</sub>N<sub>4</sub>/ BiNbO<sub>4</sub>) was examined through the degradation of oxytetracycline (OTC) under sunlight irradiation. This combination aims to leverage the stability and electron mobility of BiNbO<sub>4</sub> with the visible light absorption and photocatalytic efficiency of g-C<sub>3</sub>N<sub>4</sub> resulting in a more effective photocatalytic system for environmental applications. Sunlight is used to conduct photocatalysis because it provides a sustainable and abundant source of energy, making the process environmentally friendly and costeffective (El Golli et al., 2023). Unlike artificial light sources, sunlight covers a broad spectrum, including ultraviolet (UV) and visible light, which is ideal for activating photocatalysts like g-C<sub>3</sub>N<sub>4</sub> and BiNbO<sub>4</sub>. g-C<sub>3</sub>N<sub>4</sub>, with its narrow bandgap, is particularly effective in absorbing visible light, which constitutes most of the sunlight (Ham et al., 2023). This allows for better utilization of the solar spectrum in driving photocatalytic reactions. The use of sunlight also reduces energy consumption, aligning the process with green chemistry principles by minimizing the carbon footprint associated with traditional pollutant degradation methods (Wang et al., 2015). In addition, sunlight-driven photocatalysis mimics natural degradation processes, making it more compatible with large-scale environmental applications like wastewater treatment, where relying on a free, renewable energy source is highly advantageous (Ma et al., 2022).

Figure 1.1: The Structure of g-C<sub>3</sub>N<sub>4</sub> (Fidan et al., 2021)

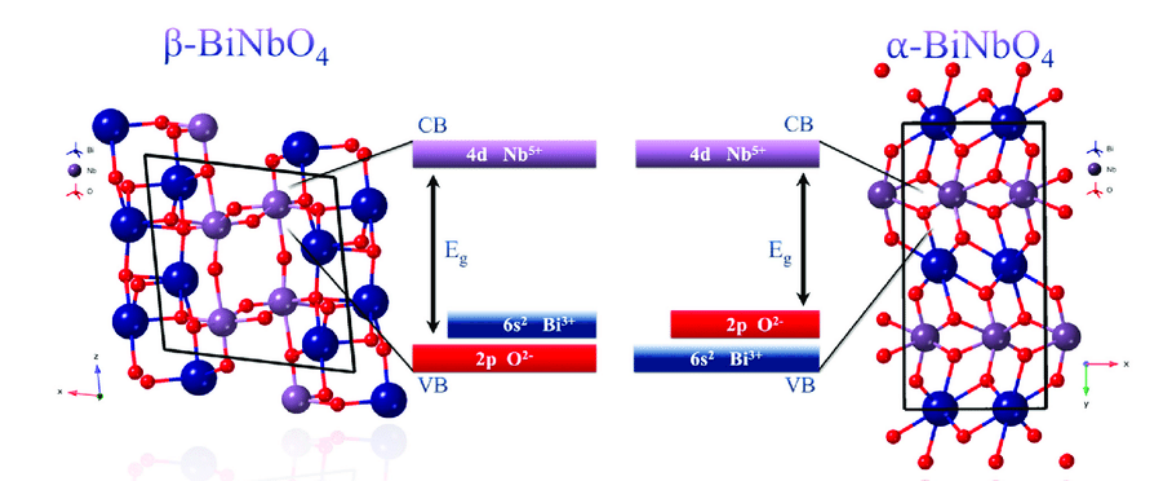


Figure 1.2: Band Structures of BiNbO<sub>4</sub> (Bakiro, et al., 2019)

#### 1.2 Problem Statement

Oxytetracycline (OTC) is an antibiotic that falls under the category of pharmaceutical and personal care products (PPCPs). The detection of residual OTC in aquatic environments has been observed owing to its chemical properties and widespread usage (Wang et al., 2020). Conventional treatment methods are not suitable for effectively removing OTC. The low efficiency of conventional treatments has made them unfavourable for degrading OTC due to their high costs, long processing times, and the production of secondary pollutants. Therefore, photocatalysis as an advanced oxidation process is suitable for degrading OTC. However, graphitic carbon nitride (g-C<sub>3</sub>N<sub>4</sub>) as a photocatalyst has some drawbacks as well. It has a moderate band gap and a high recombination rate of photo-generated charge carriers. By coupling it with bismuth niobate (BiNbO<sub>4</sub>) also known as BNO, its photocatalytic performance can be improved by utilising a wider range of the solar spectrum and enhancing the separation of charge carriers. BiNbO4 was selected because its conduction/valence band edges align well with those of g-C<sub>3</sub>N<sub>4</sub> to drive efficient interfacial charge transfer and suppress recombination, outperforming more common photocatalysts such as TiO<sub>2</sub> or BiVO<sub>4</sub>. Thus, g-C<sub>3</sub>N<sub>4</sub>/BiNbO<sub>4</sub> as a modified heterojunction photocatalyst is proposed for effectively degrading OTC.

#### 1.3 Aims and Objectives

The main objectives of this study are:

- 1) To synthesise g-C<sub>3</sub>N<sub>4</sub>/BiNbO<sub>4</sub> through the sol-gel method.
- 2) To study the physical and chemical properties of g-C<sub>3</sub>N<sub>4</sub>/BiNbO<sub>4</sub> through various characterisations.
- 3) To evaluate the photocatalytic activity of the synthesised g-C<sub>3</sub>N<sub>4</sub>/BiNbO<sub>4</sub> through the degradation of oxytetracycline (OTC) under sunlight irradiation.

#### 1.4 Scope of Study

This study aims to explore the photocatalytic activity of the g-C<sub>3</sub>N<sub>4</sub>/BiNbO<sub>4</sub> composite in degrading OTC under sunlight. Various characterisations, including FESEM-EDX, HRTEM, XRD, FTIR, and UV-Vis DRS, will be performed to assess the sample's parameters and its effectiveness as a heterojunction photocatalyst. Additionally, the optimal performance of the g-C<sub>3</sub>N<sub>4</sub>/BiNbO<sub>4</sub> composites will be identified through photocatalytic degradation to determine the best ratio of g-C<sub>3</sub>N<sub>4</sub> to BiNbO<sub>4</sub>. Moreover, scavenging and cycling tests will be conducted after successful photocatalytic degradation to analyse the dominant active radical species in the photocatalysis process and the photocatalyst's stability, respectively.

#### **CHAPTER 2**

#### LITERATURE REVIEW

#### 2.1 Pharmaceuticals and Personal Care Products (PPCPs)

Pharmaceuticals and Personal Care Products (PPCPs) encompass a broad range of chemical compounds, including medications and personal care items. These products are widely used globally and are known to enter aquatic ecosystems from various sources, such as domestic wastewater (Kuroda & Kobayashi, 2020). They have been detected in numerous aquatic environments, as well as in solids and sediments, raising concerns about their potential harmful effects on human health and the environment (Jiao et al., 2022).

PPCPs can pose significant risks to human health and the environment due to their ability to bioaccumulate in organisms, disrupt endocrine systems, and contribute to antibiotic resistance. Despite partial or complete degradation, PPCPs persist in the environment and are considered pseudo-persistent due to their continuous release. Their removal is challenging because they are present in trace amounts and are difficult to detect and quantify (Yun-Ya Yang, Gurpal S. Toor, and Alexander J. Reisinger, 2021). PPCPs can survive for long periods and resist conventional wastewater treatment methods, allowing these compounds to persist in treated effluent and potentially accumulate in the environment (Madhura et al., 2020). However, advanced oxidation processes (AOPs) have been shown to be effective in eliminating PPCPs from aquatic environments (Jiao et al., 2022).

#### 2.1.1 Oxytetracycline (OTC)

Oxytetracycline (OTC) is a broad-spectrum antibiotic that belongs to the tetracycline class. It is widely used in human medicine for treating various bacterial infections and in veterinary medicine for preventing and controlling diseases in livestock and aquaculture. Its extensive usage has led to its pervasive presence in the environment, particularly in aquatic ecosystems (Kim et al., 2021).

OTC is commonly detected in water bodies due to its extensive use and incomplete metabolism in humans and animals. After administration, a significant portion of OTC is excreted unchanged or as active metabolites, which then enter wastewater treatment systems and, subsequently, natural water bodies. Traditional wastewater treatment plants are often ineffective in fully removing OTC, resulting in its persistent presence in the environment. This persistence is attributed to OTC's chemical stability and resistance to biodegradation.

The environmental presence of OTC raises concerns due to its potential adverse effects on aquatic organisms and ecosystems. Studies have shown that OTC can bioaccumulate in aquatic species, leading to toxic effects such as impaired growth, reproduction, and development (Elia et al., 2014). Moreover, the presence of OTC in the environment may promote the emergence of antibiotic-resistant bacteria, which poses a serious risk to public health (Li et al., 2021).

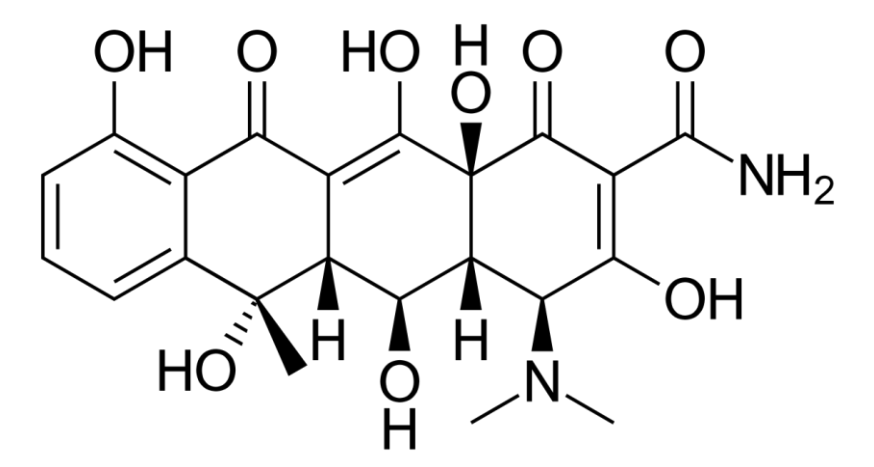


Figure 2.1: Oxytetracycline, OTC

**Table 2.1: Various Photocatalyst Used for Degrading OTC** 

Photocatalyst	<b>Light Source</b>	Results	Reference
2D/2D g-C <sub>3</sub> N <sub>4</sub> /CuO	Visible Light	100% removal of OTC in	(Wang et al.,
		10 minutes in PMS/Vis	2021)
		System	
g-C <sub>3</sub> N <sub>4</sub> /BiOCl/Cds	Visible Light	99% removal of OTC	(Senasu et al.,
		after 4 hours	2023)
$g$ - $C_3N_4$ / $CuVA$	LED Light	80% removal of OTC	(Wee et al., 2024)
		after 6 hours	
$g\text{-}C_3N_4/MnFe_2O_4$	Visible Light	•90% removal of OTC	(Li et al., 2024)
		within 1 minutes	
		• 100% removal of OTC	
		after five cycling	
$g\text{-}C_3N_4/\text{ LaFeO}_3\left(2\%\right)$	Visible Light	90% removal of 40mg/L	(Xu et al., 2020)
		OTC within 160 minutes	
$2D/2D$ $20g-C_3N_4/$	Visible LED	87% removal of OTC	(Majumdar, Gosh,
Bi <sub>4</sub> NbO <sub>8</sub> Cl	Light	after 60 minutes	& Pal, 2021)
$g-C_3N_4/Fe_3O_4$	UV Light	99.8% removal of 5mg/L	(Mahmoudi et al.,
		OTC after 60 minutes	2024)
CoFe@NSC	Visible Light	90% removal of 50mg/L	(Zhang et al.,
		OTC after 150 minutes	2021)
TiO <sub>2</sub> /5A zeolite	UV Light	100% removal of 50mg/L	(Zhao et al., 2014)
		OTC after 150 minutes	
$ZnO/ZrO_2$	UV Light	69% removal of 10mg/L	(Vaizoğullar,
		OTC after 120 minutes	2019)
g-C <sub>3</sub> N <sub>4</sub> /Br (15%)	Visible Light	75% removal of 10mg/L	(Hong et al.,
		OTC after 120 minutes	2019)

#### 2.2 Conventional Treatment Method

Conventional wastewater treatment methods, including biological treatment, sedimentation, filtration, and chemical coagulation, are inadequate for effectively removing oxytetracycline (OTC) from water bodies due to the drug's chemical stability and persistence in the environment. OTC's molecular structure makes it resistant to breakdown by standard treatments, resulting in its continued presence in treated wastewater. Biological treatments have low removal efficiency for OTC, as its antibiotic properties inhibit microbial activity essential for degradation (Sponza & Celebi, 2012). Conventional methods often lead to incomplete degradation, forming harmful intermediate products (Tang et al., 2023). Physical treatments like filtration and sedimentation are ineffective against dissolved OTC, leaving it in treated effluent (Hassanzadeh et al., 2017). This persistence raises significant public health concerns by contributing to antibiotic resistance, highlighting a critical gap in current wastewater treatment practices.

Given the complex structure, the inherent limitations of conventional wastewater treatment methods render them unsuitable for the effective removal of OTC. The chemical stability of OTC, low removal efficiency of biological treatments, incomplete degradation, inefficacy of physical treatments, and the risk of antibiotic resistance all contribute to the inadequacy of these traditional approaches. Advanced oxidation processes, particularly photocatalysis, offer a promising alternative, capable of addressing these challenges and ensuring the complete and safe degradation of OTC in wastewater (Pelosato et al., 2022).

**Table 2.2: Various Conventional Treatment Method for OTC Removal** 

Method	Removal	Remarks	Reference
	Efficiency		
Activated Carbon	59.3% removal of	Addition of activated	(Molina-Amaya et
Adsorption	10mg/mL OTC at	carbon (AC) to chitosan	al., 2024)
	pH 6-7, 30°C	biocomposite, contact	
		time 2 hrs at 100 rpm, 4g	
		biocomposite/L solution,	
		low efficiency	
Biological	80% removal of	Soybean seeds used as	(Boonsaner &
Treatment	105mg/kg OTC in	absorbent for remediation	Hawker, 2010)
	soil after 10 days	in Thailand; long time	
		taken	
	<b>-</b> 10/		~~
_		3000 mg/L sludge at pH	
Process	ppb of OTC	7; low efficiency	2011)
Anaerobic	60% removal of	Long time taken; Low	(Arikan et al.,
Digester	10mg/L OTC in		2006)
Digester	64 days at pH 7,	cinciency	2000)
	35°C		
	33 C		
Ozonation	99% removal of	In 5 to 30 minutes	(Li et al., 2008)
		ozonation, produce more	,
	_	toxic products then initial	
	at pH 11	material.	

#### 2.3 Advanced Oxidation Process

Advanced Oxidation Processes (AOPs) refer to a set of chemical treatment techniques specifically designed to efficiently eliminate organic contaminants from wastewater. This is accomplished through oxidation, wherein organic pollutants interact with potent oxidants like hydroxyl radicals (·OH) (Deng & Zhao, 2015). AOPs rely on the generation of hydroxyl radicals within the water matrix, which are extremely strong oxidants capable of oxidising a wide variety of substances found in water (Feijoo et al., 2023). The reaction rate of this oxidation process is typically controlled by diffusion, leading to the hydroxyl radical's general reactivity upon formation. This results in the rapid and effective breakdown of pollutants into smaller inorganic molecules (American Water Chemicals, 2023).

Additionally, methods such as photocatalysis, ozonation, and electrolysis are examples of AOPs. In this study, photocatalysis will be employed to degrade OTC. Photocatalysis, a light-driven AOP, is especially appealing due to the abundance of solar light, its relatively low cost, and its high efficiency (Félicien Mazille and Dorothee Spuhler, 2020). These methods utilise the generation of highly reactive species, such as hydroxyl radicals, to achieve complete degradation of OTC into harmless by-products. Unlike conventional methods, AOPs offer the potential for thorough mineralisation, ensuring that OTC and its by-products are fully broken down, thus providing a more effective and sustainable solution for wastewater treatment (Feijoo et al., 2023).

#### 2.4 Photocatalysis

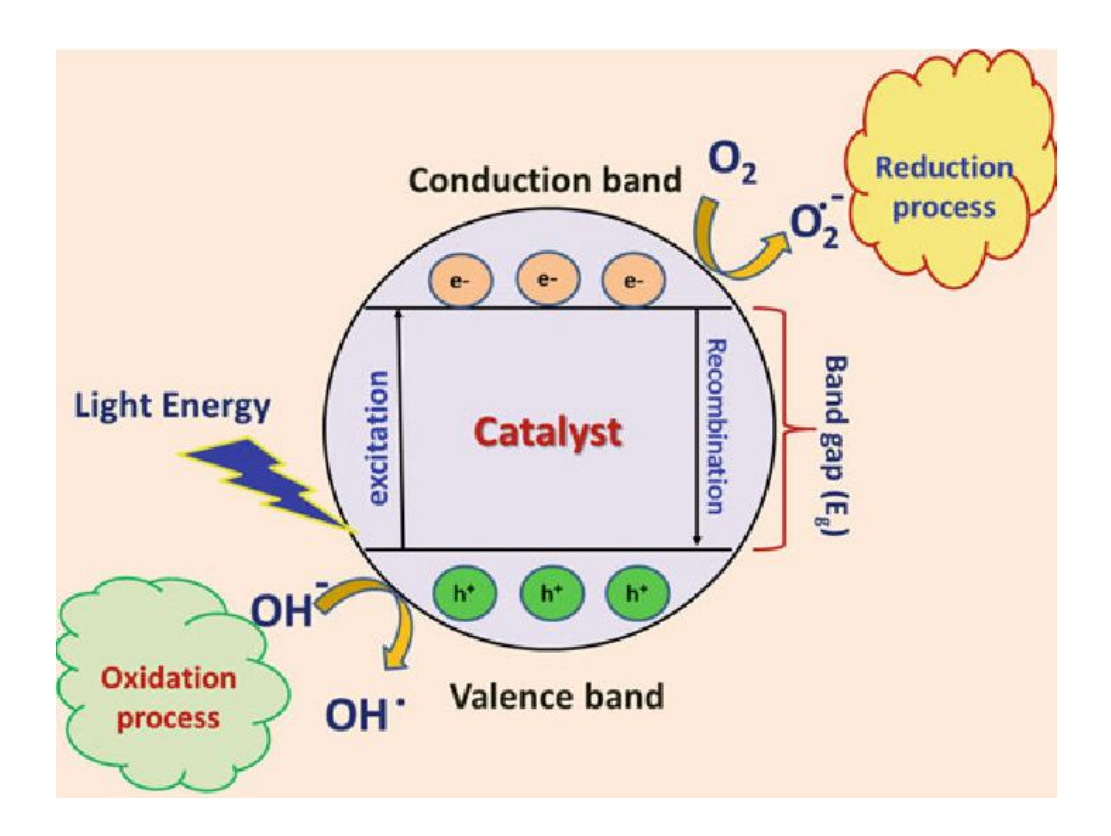


Figure 2.2: Schematic of Photocatalytic Activity Mechanism (Saravanan, Gracia & Steven, 2017)

Photocatalysis employs light energy to activate a photocatalyst, thereby accelerating chemical reactions—particularly the oxidation of organic contaminants in wastewater. Upon illumination with photons of an appropriate wavelength, an electron in the photocatalyst's valence band absorbs this energy and is promoted to the conduction band, leaving behind a hole in the valence band (Saravanan, Gracia, & Stephen, 2017). These photogenerated electrons and holes then migrate to the catalyst's surface, where they react with water or oxygen to generate reactive species such as hydroxyl radicals (·OH), which oxidize the organic pollutants (Saravanan, Gracia, & Stephen, 2017).

For effective photocatalysis, the energy levels of the VB and CB must align with the redox potentials of the photocatalytic reaction to ensure the photocatalyst can facilitate the reaction efficiently (Li and Wu, 2015). The band gap energy, defined as the difference between the VB and CB, is crucial for this process. Figure 2.1 illustrates the basic concept of photocatalysis (Saravanan R. and Gracia, 2017). The efficiency of photocatalysis can be hindered by the recombination of excited electrons and holes before they participate in the photocatalytic reaction. Therefore, minimising the

recombination rate is essential to enhance photocatalytic activity (Xia et al., 2023). This can be achieved using heterojunction photocatalysts, which facilitate the transfer of excited carriers between two different photocatalysts, thereby reducing the recombination rate (Gao et al., 2019).

According to Ameta et al. (2018), photocatalytic reactions can be categorised into two types based on the physical state of the reactants:

- **1. Homogeneous photocatalysis:** This is observed when the semiconductor and the reactant coexist in the same phase, whether that phase is gas, solid, or liquid.
- **2. Heterogeneous photocatalysis:** This describes situations in which the semiconductor and reactant occupy different phases.

According to Ameta et al. (2018), the term band gap describes the energy separation between the valence band and conduction band. Materials are then grouped into three categories based on their band-gap values:

- 1. Metal or Conductor: Band gap less than 1.0 eV.
- 2. Semiconductor: Band gap between 1.5 and 3.0 eV.
- 3. Insulator: Band gap greater than 5.0 eV.

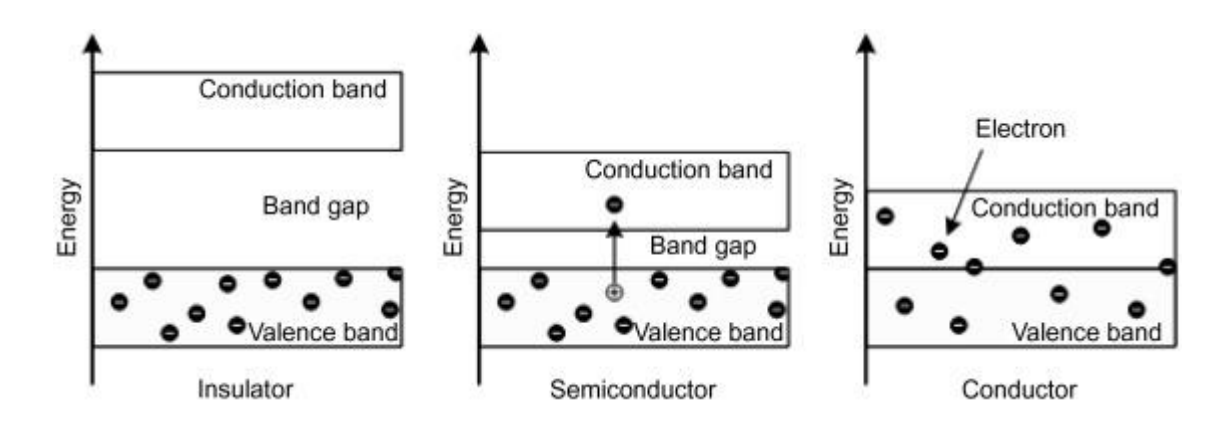


Figure 2.3: Band Gap on Different Types of Materials (Ameta et al., 2018)

Semiconductors can act as efficient photocatalysts because they can conduct electricity at room temperature when exposed to light. When illuminated with light of adequate energy, electrons in the valence band absorb photons and become excited, transitioning to the conduction band and leaving holes in the valence band. This process generates an electron-hole pair, known as the photo-excitation state. In this state, the excited electron can participate in reduction reactions by transferring to an acceptor, while the hole can oxidize donor molecules. A defining characteristic of photocatalysis is its ability to drive both oxidation and reduction processes simultaneously. The fate of these excited charge carriers is determined by the relative energy levels of the semiconductor's conduction and valence bands compared to the redox potentials of the target substrate. Depending on these energy alignments, there are four possible interaction scenarios between the semiconductor and the substrate:

- **(A) Reduction occurs:** The redox potential of the substrate is positioned below the conduction band of the semiconductor.
- **(B) Oxidation occurs:** The redox potential of the substrate exceeds the energy level of the semiconductor's valence band.
- **(C)** Both reduction and oxidation occur: The substrate's redox potential is situated below the conduction band and above the valence band of the semiconductor.
- **(D)** No reaction occurs (neither oxidation nor reduction): The redox potential of the substrate falls within the range between the semiconductor's conduction and valence bands.

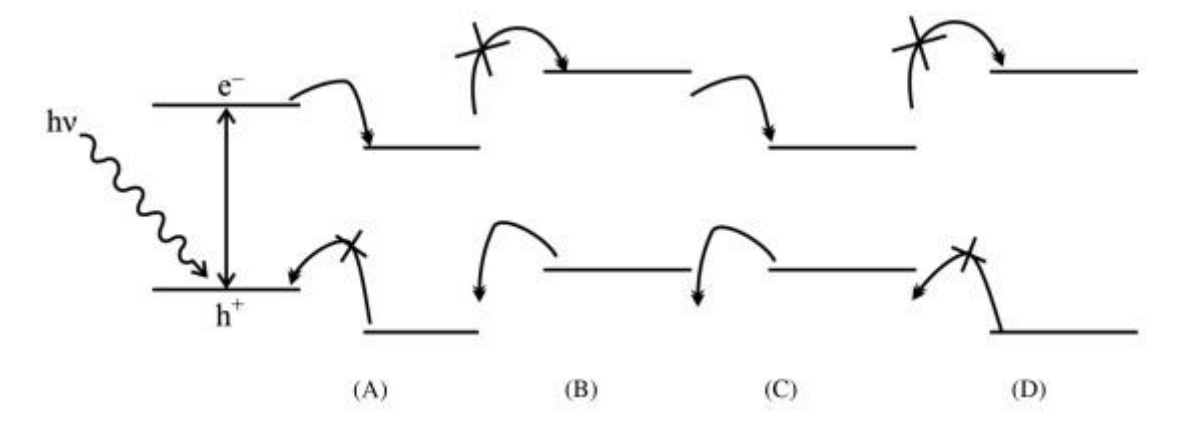


Figure 2.4: Different possibilities of reactions. (A) Reduction. (B) Oxidation. (C)

Redox (D) No reaction (Ameta et al., 2018)

#### 2.5 Heterojunction Photocatalyst

A heterojunction photocatalyst involves coupling two semiconductor photocatalysts with complementary properties to form a heterojunction. The primary function of heterojunction photocatalysts is to facilitate the transfer of photogenerated carriers between two different semiconductor materials, thereby suppressing the recombination rate and enhancing the efficiency of the photocatalytic process (Goodarzi et al., 2023). The photocatalytic activity of a heterojunction photocatalyst is primarily influenced by its band alignment. An optimal band gap structure and band alignment can improve photocatalytic activity by promoting the separation and transfer of photogenerated carriers. Additionally, the photocatalytic performance can be enhanced by expanding the light absorption range (Low et al., 2017).

In this study, g-C<sub>3</sub>N<sub>4</sub> and BiNbO<sub>4</sub> will be combined to form a heterojunction photocatalyst. This combination is anticipated to improve the photocatalytic performance of BiNbO<sub>4</sub> by reducing its band gap energy and minimizing electron-hole recombination, thus boosting overall efficiency.

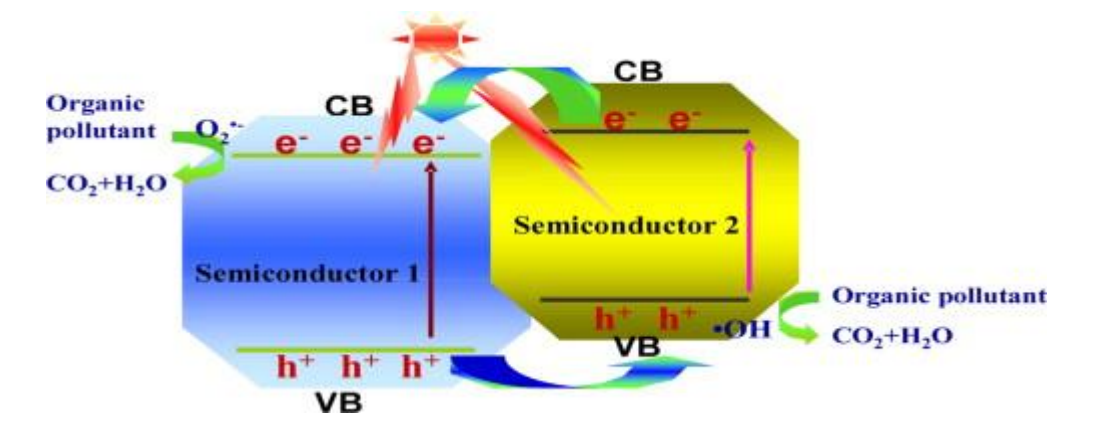


Figure 2.5: Design and fabrication of heterojunction photocatalysts for energy conversion and pollutant degradation (Yu., et al., 2014)

#### 2.5.1 BiNbO<sub>4</sub> Coupled with g-C<sub>3</sub>N<sub>4</sub>

Bismuth niobate (BiNbO<sub>4</sub>) is an effective photocatalyst due to its distinctive features, making it a strong candidate for high efficiency photocatalysis. BiNbO<sub>4</sub> is notable for its responsiveness to visible light, mainly because the Bi 6s orbital in the valence band (VB) sits above the O-2p orbital, which narrows the band gap (BG) and renders it responsive to visible light (Luo et al., 2022). BiNbO<sub>4</sub> typically adopts either the  $\alpha$  or  $\beta$ polymorphic form and respectively possessing orthorhombic and triclinic lattice structures. These phases have different band energies and photocatalytic activities, with the  $\alpha$  phase having a BG range of 2.6 eV-2.8 eV and the  $\beta$  phase ranging from 3.2 eV to 3.4 eV. The phase transitions between  $\alpha$  and  $\beta$  forms can be influenced by temperature and pressure during synthesis (Alcântara et al., 2018). Furthermore, two primary derivatives, Bi<sub>5</sub>Nb<sub>3</sub>O<sub>15</sub> and Bi<sub>3</sub>NbO<sub>7</sub>, can form during phase transitions. Its oxygen-deficient, fluorite-type lattice of Bi<sub>3</sub>NbO<sub>7</sub> facilitates electron accumulation and enhances charge-carrier separation. The aurivillius structure of Bi<sub>5</sub>Nb<sub>3</sub>O<sub>15</sub>, with intergrowth of (Bi<sub>2</sub>O<sub>2</sub>) nanosheets between perovskite slabs, offers additional reactive sites and aligns its conduction band and valence band edges with those of BiNbO<sub>4</sub>, leading to higher photocatalytic activity compared to bulk BiNbO<sub>4</sub> (Tahara et al., 2007; Li et al., 2010).

When prepared by the citrate sol–gel method and calcined at temperatures from 550 °C to 1150 °C, bismuth niobate underwent a phase transition (Zhai et al., 2011). At 550°C, the intermediate Bi<sub>5</sub>Nb<sub>3</sub>O<sub>15</sub> appeared, while at 600°C, the  $\beta$  phase emerged and existed alongside with Bi<sub>5</sub>Nb<sub>3</sub>O<sub>15</sub>. At 750°C, the pure  $\beta$  phase was observed, and above 750°C, the  $\alpha$  phase began to form, becoming pure at 900°C. This indicated that Bi<sub>5</sub>Nb<sub>3</sub>O<sub>15</sub> undergoes a reversible  $\alpha$ – $\beta$ – $\alpha$  phase transition (Zhai et al., 2011; Xu et al., 2013). It was also shown that  $\alpha$  and  $\beta$  phases coexist within the same crystal, extending light absorption to 460 nm with a band gap of 2.6 eV and enhancing the crystal's properties relative to bulk BiNbO<sub>4</sub> (450 nm, E<sub>g</sub> = 2.7 eV) (Mahdi et al., 2022). Building on these findings, the synthesis of bismuth niobate was fined-tuned to maximize its solar-driven photocatalytic performance by varying the post-solvothermal calcination temperature from 300 °C to 900 °C. The solvothermal route was selected for its advantage of lower reaction temperatures, enhanced precursor mixing in the liquid

phase, and the ability to produce uniformly sized nanoparticles with controlled morphology (Kiran et al., 2020). By co-using ethylene glycol (EG) as a polyhydroxy alcohol and polyethylene glycol (PEG) as a coordinating polymer, metal-ion mobility was curtailed, and premature salt precipitation was prevented through stable metal-polymer complex formation. This method produced a highly efficient solar light-active BiNbO<sub>4</sub> variant with a band gap of 2.33 eV and superior photocatalytic activity compared to the α-phase (orthorhombic BiNbO<sub>4</sub>). Combining BiNbO<sub>4</sub> with g-C<sub>3</sub>N<sub>4</sub> further extended charge-carrier lifetime and increased charge trapping sites, resulting in improved photocatalytic activity compared to the individual materials.

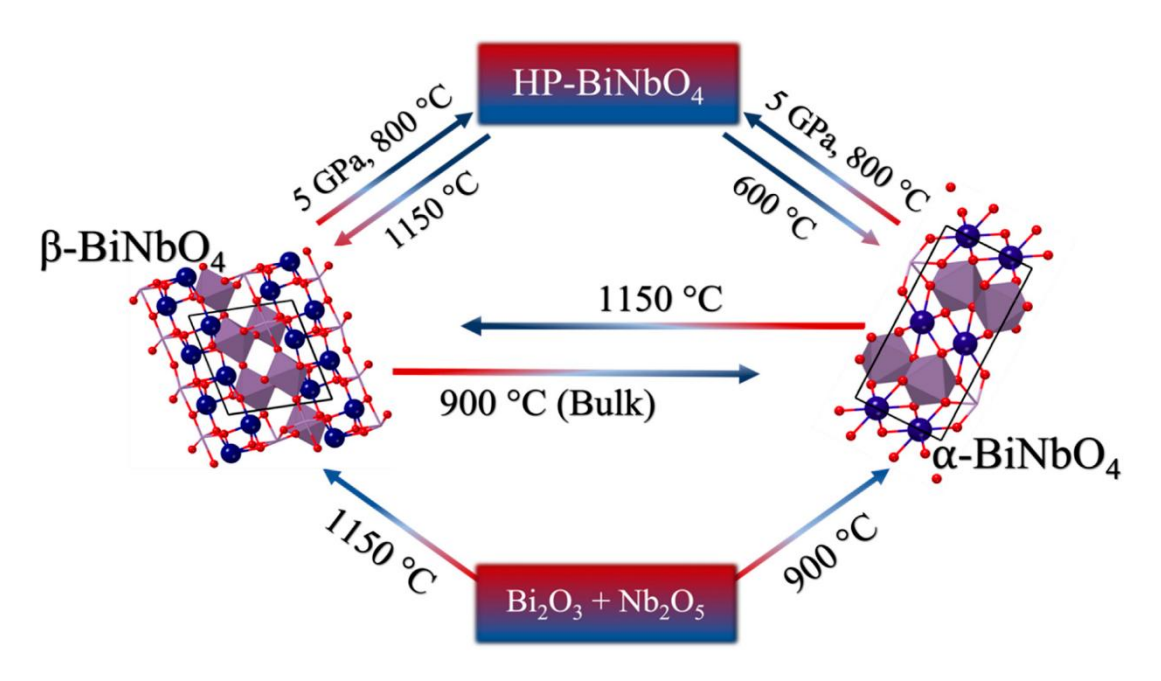


Figure 2.6: Phase Change of BiNbO<sub>4</sub> (Bakiro, et al., 2019)

#### 2.6 Sustainable Development Goal (SDGs)

#### SDG 3: Good Health and Well-being

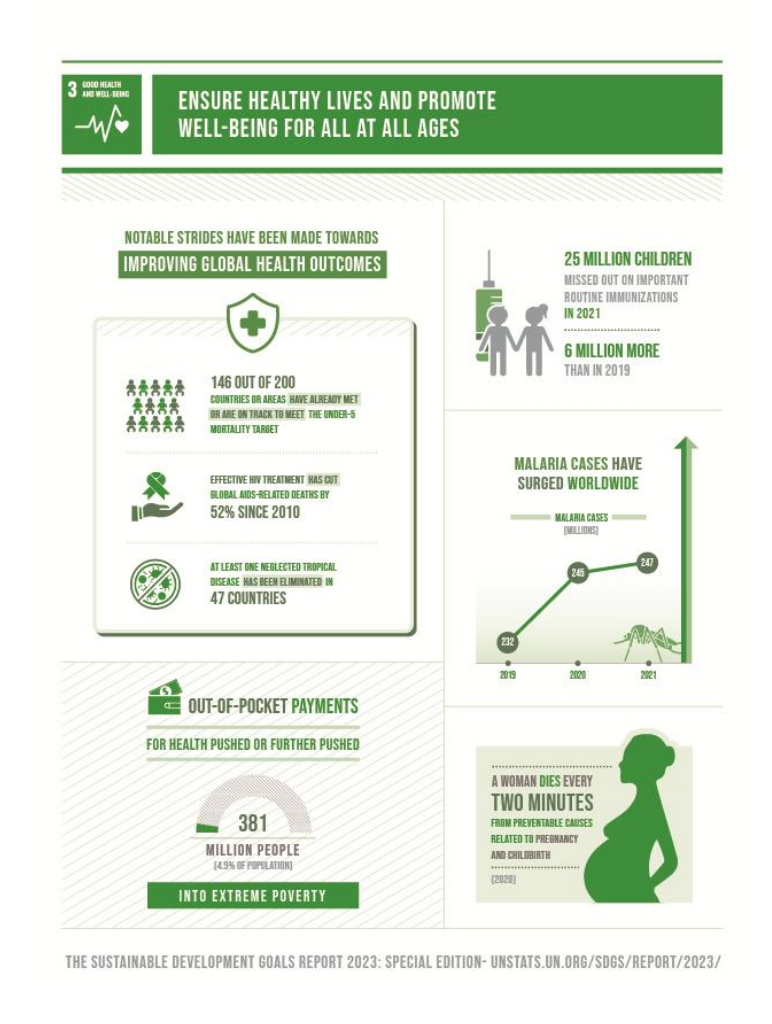


Figure 2.7: SDG 3 (UN – DESA, 2023)

Pharmaceuticals, such as oxytetracycline, are widely used in veterinary and human medicine, leading to their pervasive presence in water bodies due to improper disposal or excretion. These pharmaceutical residues in the environment can lead to the development of antibiotic-resistant bacteria, posing a significant threat to public health.

This project addresses this challenge by developing a photocatalytic material (BiNbO<sub>4</sub>/g-C<sub>3</sub>N<sub>4</sub>) capable of degrading oxytetracycline in water. By reducing the concentration of this antibiotic in water bodies, your research directly contributes to mitigating the risks associated with antibiotic resistance, thereby promoting better health outcomes. This aligns with the objective of SDG 3 to ensure healthy lives and promote well-being for all, at all ages.

#### SDG 6: Clean Water and Sanitation

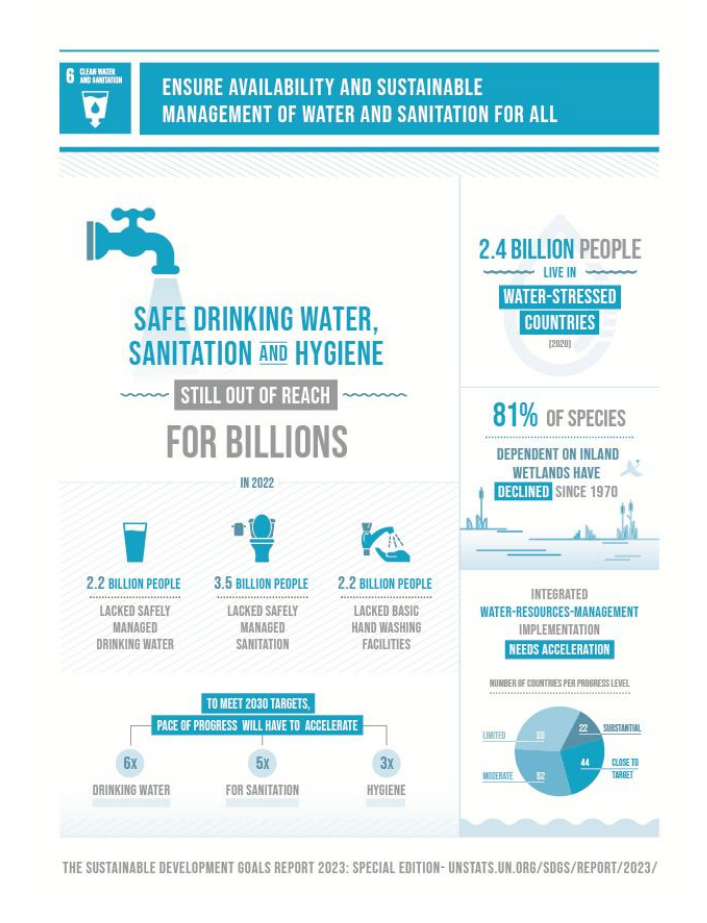


Figure 2.8: SDG 6 (UN – DESA, 2023)

SDG 6 emphasizes the need for clean water, which is essential for health and well-being. Pharmaceutical contaminants like oxytetracycline can persist in water sources, leading to environmental and health hazards. Conventional water treatment methods often fail to remove such micropollutants effectively.

The development of an efficient photocatalytic material for degrading oxytetracycline represents a significant advancement in water purification technology. BiNbO<sub>4</sub>/g-C<sub>3</sub>N<sub>4</sub>, as synthesised in this project, offers a sustainable solution to remove harmful antibiotics from water sources, contributing to the provision of safe drinking water. This innovation supports the goal of achieving universal access to safe and affordable drinking water (SDG 6.1) and improving water quality by reducing pollution (SDG 6.3).

## BUILD RESILIENT INFRASTRUCTURE, PROMOTE INCLUSIVE AND SUSTAINABLE INDUSTRIALIZATION AND FOSTER INNOVATION GLOBAL MANUFACTURING **ENERGY-RELATED** GROWTH SLOWED FROM CO2 EMISSIONS DUE TO REACHED 2021 7.4% 36.8 BILLION METRIC TONS IN 2022 A RECORD HIGH MEDIUM-HIGH 🎹 HIGH-TECHNOLOGY INDUSTRIES EXPERIENCED = STRONG GROWTH IN 2022 LDCs ARE LIKELY TO MISS THEIR 2030 TARGET **BUT WITH REGIONAL VARIATION** OF DOUBLING MANUFACTURING SHARE OF GDP SHARE IN TOTAL MANUFACTURING MANUFACTURING VALUE AS A SHARE OF GOP IN LDGs 95% OF THE WORLD HAS MOBILE BROADBAND ACCESS [3G OR HIGHER] (2022) BUT COVERAGE IS ONLY 82% IN SUB-SAHARAN AFRICA AND 68% IN OCEANIA THE SUSTAINABLE DEVELOPMENT GOALS REPORT 2023: SPECIAL EDITION- UNSTATS.UN.ORG/SDGS/REPORT/2023/

## SDG 9: Industry, Innovation, and Infrastructure

Figure 2.9: SDG 9 (UN – DESA, 2023)

SDG 9 highlights the need to develop robust infrastructure, support inclusive and sustainable industrial growth, and encourage innovation. The environmental challenges posed by pharmaceutical contaminants require innovative solutions in water treatment and pollution control technologies.

This research contributes to SDG 9 by innovating in the field of photocatalysis. The synthesis of BiNbO<sub>4</sub>/g-C<sub>3</sub>N<sub>4</sub> represents a novel approach to tackling pharmaceutical pollutants in water, contributing to the development of advanced materials that can be integrated into water treatment infrastructure. This innovation not only addresses current environmental issues but also lays the groundwork for future technologies that can be applied on an industrial scale, promoting sustainable industrial practices and resilient infrastructure in water management.

## **ENSURE SUSTAINABLE CONSUMPTION** AND PRODUCTION PATTERNS DESPITE CALLS FOR HIGH-INCOME COUNTRIES A PHASE-OUT LEAVE A LARGER ENVIRONMENTAL FOOTPRINT COMPARED TO FOSSIL FUEL SUBSIDIES -LOW-INCOME COUNTRIES RETURN AND NEARLY DOUBLED, TRIGGERED MATERIAL FOOTPRINT PER CAPITA IN HIGH-INCOME COUNTRIES IS BY GLOBAL CRISES 10 TIMES THAT OF LOW-INCOME COUNTRIES ON AVERAGE 120 KILOGRAMS OF FOOD PER YEAR SUSTAINABILITY 62 COUNTRIES + EU COMPANY INTRODUCED -SUSTAINABILITY **485 POLICIES** REPORTING HAS TRIPLED FOR SUSTAINABLE **SINCE 2016** THE SUSTAINABLE DEVELOPMENT GOALS REPORT 2023: SPECIAL EDITION- UNSTATS.UN.ORG/SDGS/REPORT/2023/

## SDG 12: Responsible Consumption and Production

Figure 2.10: SDG 12 (UN – DESA, 2023)

SDG 12 promotes sustainable practices in the production and consumption of goods, including the management of chemicals and waste. The widespread use of antibiotics like oxytetracycline in agriculture and medicine has led to significant environmental contamination, which needs to be managed responsibly.

The research on the synthesis of BiNbO<sub>4</sub>/g-C<sub>3</sub>N<sub>4</sub> for photocatalytic degradation contributes to responsible waste management by providing a method to effectively break down pharmaceutical pollutants in water. This innovation helps in reducing the environmental footprint of pharmaceutical waste, aligning with SDG 12's target of ensuring environmentally sound management of chemicals and all wastes throughout their life cycle (SDG 12.4). Moreover, by promoting the use of advanced, environmentally friendly materials for pollution control, this project encourages more sustainable consumption and production patterns.

#### SDG 14: Life Below Water

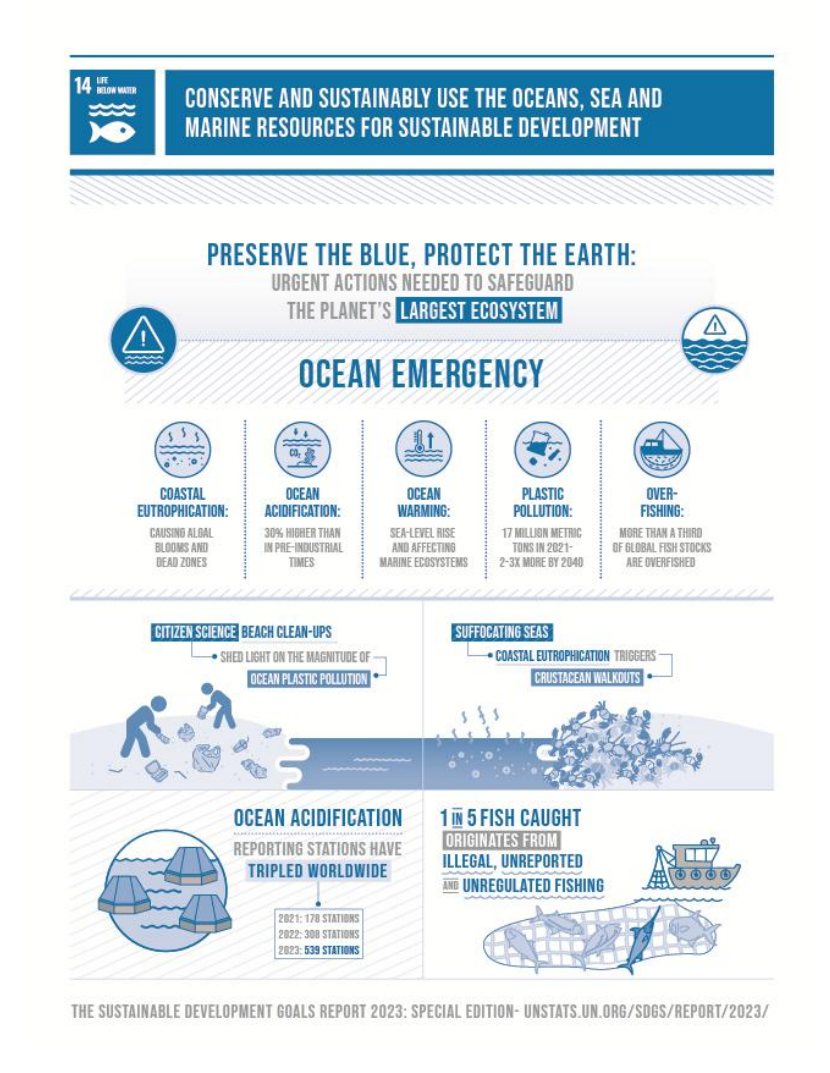


Figure 2.11: SDG 14 (UN – DESA, 2023)

SDG 14 is dedicated to preserving oceans, seas, and marine resources through sustainable practice. Contaminants like oxytetracycline pose a threat to aquatic life, leading to disruptions in marine ecosystems and the potential bioaccumulation of harmful substances in the food chain.

By developing a photocatalytic material that can degrade oxytetracycline, your project directly contributes to reducing the levels of harmful contaminants in aquatic environments. This reduction in pollutant levels helps protect marine biodiversity and maintains the health of aquatic ecosystems. Consequently, this research supports the SDG 14 targets of preventing and significantly reducing marine pollution (SDG 14.1) and conserving marine and coastal ecosystems (SDG 14.2).

#### 2.7 Summary

The literature review outlines the pervasive occurrence of pharmaceuticals and personal care products (PPCPs), notably oxytetracycline (OTC) in aquatic environments and highlights the inadequacy of conventional treatment methods (biological, physical and chemical) to fully remove these compounds due to their chemical stability and resistance to biodegradation. Advanced oxidation processes (AOPs), and particularly photocatalysis, emerge as promising alternatives because of their ability to generate highly reactive radicals under light irradiation, achieving deeper mineralisation of persistent pollutants.

Graphitic carbon nitride (g-C<sub>3</sub>N<sub>4</sub>) has been widely studied as a visible-light photocatalyst for degrading PPCPs like oxytetracycline (OTC), but its moderate band gap and rapid electron–hole recombination limit its standalone performance. To overcome these drawbacks, heterogeneous coupling of g-C<sub>3</sub>N<sub>4</sub> with various semiconductors (e.g., CuO, BiOCl/CdS, MnFe<sub>2</sub>O<sub>4</sub>, LaFeO<sub>3</sub>, Fe<sub>3</sub>O<sub>4</sub>, Bi<sub>4</sub>NbO<sub>8</sub>Cl) has been extensively explored, with many studies achieving >85–100% OTC removal under visible or UV light within minutes to hours as shown in **Table 2.1**, yet most rely on common oxides or sulfides.

Despite these advances, there remains a lack of systematic studies on g-C<sub>3</sub>N<sub>4</sub>/BiNbO<sub>4</sub> heterojunctions under realistic water-chemistry conditions. Little work has examined how synthesis parameters (e.g., BiNbO<sub>4</sub> phase composition) influence heterojunction performance. Addressing these gaps will be crucial for translating lab-scale successes into robust, field-ready PPCP treatment solutions. The g-C<sub>3</sub>N<sub>4</sub>/BiNbO<sub>4</sub> heterojunction photocatalyst also stands out for several novel reasons:

## 1. Visible-light activation & tuneable band gap:

BiNbO<sub>4</sub>'s Bi 6s–O 2p hybridized valence band narrows its band gap to  $\sim 2.3$ – 2.8 eV, enabling stronger absorption of solar radiation than many oxides and broadening the usable spectrum beyond what g-C<sub>3</sub>N<sub>4</sub> alone can harness .

#### 2. Optimal band alignment

The conduction and valence band edges of BiNbO<sub>4</sub> align complementarily with those of g-C<sub>3</sub>N<sub>4</sub>, fostering a type-II heterojunction that directs photogenerated

electrons and holes into separate materials, thereby markedly suppressing recombination and prolonging charge-carrier lifetimes.

## 3. Phase-engineerable structure

Controlled synthesis (e.g., solvothermal plus calcination) can tailor  $BiNbO_4$ 's  $\alpha/\beta$  phases and derivatives ( $Bi_5Nb_3O_{15}$ ,  $Bi_3NbO_7$ ), each offering unique light-absorption and charge-separation advantages. This structural tunability is less accessible in more rigid photocatalysts like  $TiO_2$  or  $BiVO_4$ .

By leveraging these attributes, g-C<sub>3</sub>N<sub>4</sub>/BiNbO<sub>4</sub> exhibits enhanced solar-driven photocatalytic activity and stability, positioning it as a particularly novel and effective composite for degrading OTC and, by extension, other PPCPs.

#### **CHAPTER 3**

#### RESEARCH METHODOLOGY

This chapter will discuss the experimental methods and materials employed in the study. The research's experimental process is illustrated in **Figure 3.1**.

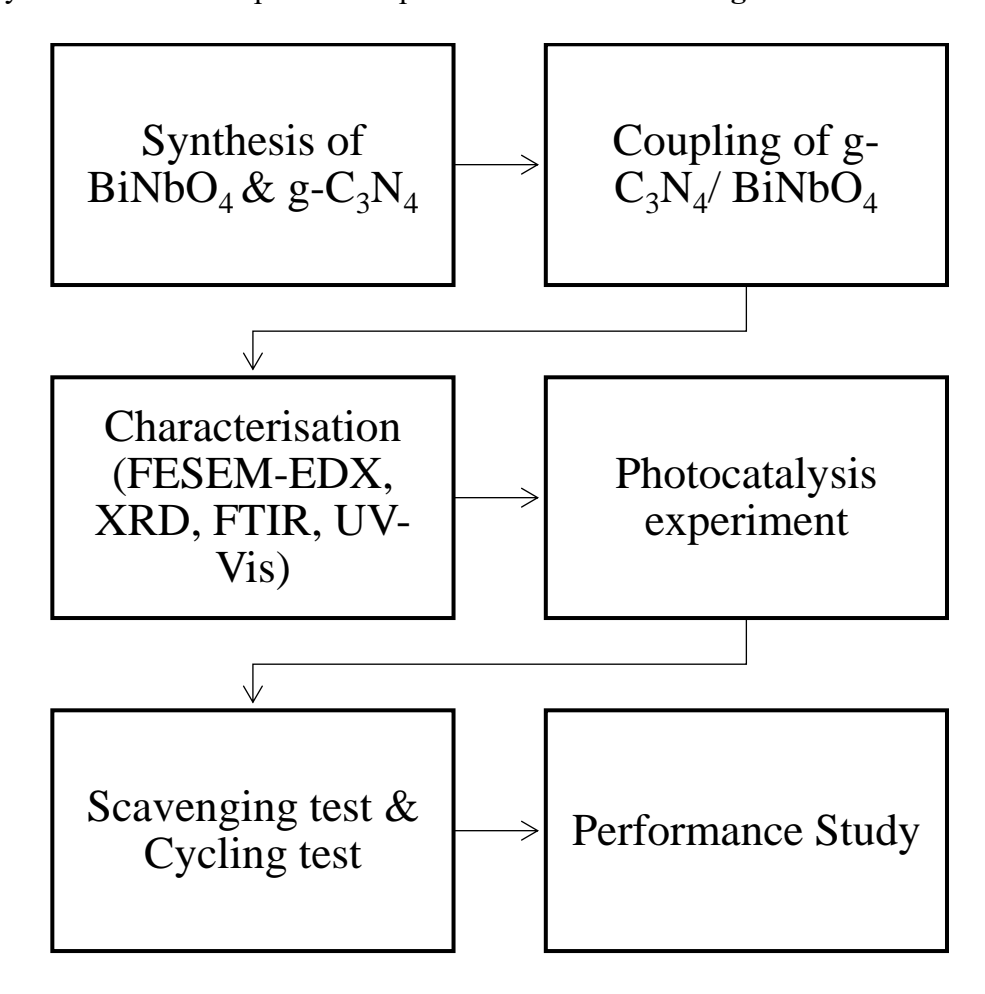


Figure 3.1: Flow Chart of Experimental Methodologies

## 3.1 Materials

**Table 3.1** presents a detailed list of the materials used in this work, including the chemicals involved. No further treatment is required prior to the application of the chemicals mentioned.

Table 3.1: List of Materials Used in This Study

Material	Purity (%)	Supplier	Remark(s)
Oxytetracycline			Pollutant
Bismuth (III) Nitrate	98.5	R&M Chemicals	Reactant
Pentahydrate,			
Bi(NO <sub>3</sub> ) <sub>3</sub> .5H <sub>2</sub> O			
Niobium Pentoxide,	99.99	Sigma-Aldrich	Reactant
$Nb_2O_5$			
Sodium acetate anhydrous,	99	Chemiz	Reactant
$C_2H_3NaO_2$			
Urea	99.5	Sigma-Aldrich	Reactant
Ethylene Glycol	99	R&M Chemicals	
Polyethylene Glycol 400	-	Chemiz	Reactant
(PEG 400)			
Nitric acid	65	R&M Chemicals	Reactant
Ethanol	95	HmbG Chemicals	Reactant
Potassium Dichromate	99.99	QReC	Scavenging
$(K_2Cr_2O_7)$			agent
Triethylamine (TEA)	98	Chemiz	Scavenging
			agent
Isopropyl alcohol (IPA)	99.9	DChemie	Scavenging
			agent
p-Benzoquinone	-	Sigma-Aldrich	Scavenging
			agent

# 3.2 Apparatus

**Table 3.2: List of Equipment Used in This Study** 

Equipment	Purpose	
Analytical balance	To measure the mass of an object.	
Chamber furnace	To provide heat treatment for curing materials.	
Centrifuge	To separate substances suspended in a liquid medium.	
Oven	To provide heat treatment and for drying process.	
Stirring hotplate	To stir and heat the solution immediately	
Ultrasonic bath	To provide ultrasonic treatment	
Spatula	To transfer materials	
Crucible	To contain materials during heat process in chamber	
	furnace	
Petri dish	To contain materials for drying process	
50 mL Centrifuge tube	To contain liquids during centrifugation	
500mL Beaker	To contain liquids and collecting samples	
Specimen Container	To contain samples and materials	

#### 3.3 Synthesis of BiNbO<sub>4</sub>

According to Shen et al. (2013), BNO was prepared via a straightforward solvothermal route and subsequent calcination. Bi(NO<sub>3</sub>)<sub>3</sub>·5H<sub>2</sub>O and Nb<sub>2</sub>O<sub>5</sub> (1:1 molar ratio) were dissolved together in 80 mL of ethylene glycol, then supplemented with 2 mL of polyethylene glycol and 7.2 g of sodium acetate. After stirring for 90 minutes, the mixture was transferred to a Teflon-lined autoclave and held at 200 °C for 22 hours. The pale-yellow precipitate was washed repeatedly with ethanol and ultrapure water, dried at 70 °C for 24 hours, and finally calcined at 500 °C. The calcined powder was once more rinsed with ultrapure water and oven-dried at 70 °C for an additional 24 hours.

## 3.4 Synthesis of g-C<sub>3</sub>N<sub>4</sub>

The g-C<sub>3</sub>N<sub>4</sub> synthesis was conducted using the thermal polymerisation method. Initially, 10 grams of urea were evenly spread in an evaporating dish and dried in an oven at 80 °C for at least 12 hours. The dried urea was then transferred to a crucible and heated in a chamber furnace at 550 °C for 4 hours. Aluminium foil is used to wrap the crucible and the lid before heating to prevent contamination, minimise the loss of volatile compounds, and protect the reactants from oxidation to ensure proper formation of g-C<sub>3</sub>N<sub>4</sub> with uniform properties for enhanced photocatalytic performance. The resulting yellowish product was washed three times with 0.1 M nitric acid (HNO<sub>3</sub>) and ultrapure water, using a centrifuge at 4000 rpm for 10 minutes to remove impurities like residual ammonia (Liu et al., 2011). Finally, the washed products were dried overnight in an oven at 80 °C for 24 hours. The dried g-C<sub>3</sub>N<sub>4</sub> was then finely ground using a ceramic mortar (Hak et al., 2020).

## 3.5 Coupling of g-C<sub>3</sub>N<sub>4</sub>/ BiNbO<sub>4</sub>

Three distinct composites were synthesized by combining BNO and GCN through simple physical mixing method, resulting in the composites labelled as 0.3 GCN/BNO, 0.5 GCN/BNO, and 0.7 GCN/BNO. Different ratios of g-C<sub>3</sub>N<sub>4</sub> are dissolve in 100mL of deionized water which is then sonicated with an ultra-sonicator for 30 minutes. The sonicated solution is then mixed with BiNbO<sub>4</sub> and stirred at room temperature for one hour. In the first composite, 0.3 GCN/BNO, 0.3 of g-C<sub>3</sub>N<sub>4</sub> and 1g of BiNbO<sub>4</sub> were used, indicating a lower proportion for g-C<sub>3</sub>N<sub>4</sub>. For the 0.5 GCN/BNO composite, 0.5g of g-C<sub>3</sub>N<sub>4</sub> and 1g BiNbO<sub>4</sub> are used. Conversely, in the 0.7 GCN/BNO composite, 0.7g of g-C<sub>3</sub>N<sub>4</sub> was used with 1g of BiNbO<sub>4</sub>, reflecting a greater concentration of g-C<sub>3</sub>N<sub>4</sub> in the mixture then the previous two composites. The precipitate of the solutions is then washed with deionized water using centrifugal method and then dried at 60°C for 24 hours to obtain the final products. This method allowed for the creation of composites with varying proportions of the two materials, enabling the study of how these different ratios impact the properties and performance of the resulting composites.

#### 3.6 Characterisation

**Table 3.3** shows the information of various characterisations done for analysing  $G_3N_4/BiNbO_4$  in this study.

Table 3.3: Characterisation for g-C<sub>3</sub>N<sub>4</sub>/ BiNbO<sub>4</sub>

Туре	Purpose	
Field emission scanning electron	To clarify the relationship between	
microscopy with energy dispersive x-	elemental composition and	
ray spectroscopy (FESEM-EDX)	morphological changes	
X-ray diffraction (XRD)	To identify the crystalline structure.	
Fourier transform infrared spectroscopy	To identify functional groups.	
(FTIR)		
Ultraviolet-Visible diffuse reflectance	To measure light absorption for plotting	
spectroscopy (UV-Vis DRS)	the band-gap energy and spectrum	
	graph.	

X-ray diffraction analysis was performed using a high-resolution X-ray diffractometer over a scan range of 5–90°, with a step size of 0.02°. The surface morphology was examined using a field emission scanning electron microscope with energy dispersive X-ray spectroscopy (FESEM-EDX). FTIR analysis was conducted to identify the functional groups present in the synthesised composites. The sample was placed on the ATR (attenuated total reflectance) crystal, and the infrared spectrum was recorded in the range of 4000–400 cm<sup>-1</sup>. The characteristic absorption peaks corresponding to different functional groups were analysed to confirm the chemical structure and composition of the materials. Solid and liquid-state light absorbance were measured using ultraviolet-visible diffuse reflectance spectroscopy (UV-Vis DRS) with an integrated sphere attachment. The materials' absorption spectra from 200 to 800 nm were plotted as a Kubelka–Munk graph, using the K–M function defined by Christy et al. (1995):

$$F(R_{\infty}) = \frac{(1 - R_{\infty})^2}{2R_{\infty}} \tag{3.1}$$

Where ' $R_{\infty}$ ' denotes the diffuse reflectance at a specific wavelength.

The Kubelka-Munk function (Eq. (3.1)) can then be substituted into the Tauc equation (Eq. (3.2)) by substituting  $\alpha$  with the corresponding functions to become (Eq. (3.3)), which is used to calculate the band gap energy (Zalfani et al., 2017).

$$(\alpha h v)^{1/n} = A(h v - E_g) \tag{3.2}$$

$$(F(R_{\infty})hv)^{1/n} = A(hv - E_g)$$
(3.3)

Where  $\alpha$  is the absorption coefficient, h is the Planck's constant (6.626 × 10<sup>-34</sup> Js), v is the light frequency, A is the proportional constant, and  $E_g$  is the band gap energy. The value of n is determined based on the type of optical transition exhibited by the semiconductor in question. For direct transitions, n is set to 1, while for indirect transitions, n is set to 2 (Yentür and Dükkancı, 2020). Accordingly, n in this study will be set to 2.

From the preceding equation, a graph of  $(F(R_{\infty})E)^n$  against E (Eq. (3.4)) is used to determine the band gap. is constructed to extract the band gap. Extrapolating the straight-line segment back to the E-axis yields the estimated band-gap value.

$$E(eV) = \frac{hc}{\lambda} \tag{3.4}$$

Where, h represents Planck's constant (6.626 ×  $10^{-34}$  Js), C is the speed of light (3.0 ×  $10^8$  ms<sup>-1</sup>) and  $\lambda$  is the wavelength (nm).

## 3.7 Photocatalytic Degradation of Oxytetracycline (OTC)

The ability of the synthesized materials to act as photocatalysts was determined via the solar-induced degradation of oxytetracycline (OTC). In a standard reaction, 0.1 g of the photocatalyst was introduced into 250 mL of a 20 ppm OTC solution. The stock solution was prepared by dissolving 20mg of OTC in 1 L of deionised water using a 1 L volumetric flask, which is then poured separately into 250 ml beakers. Before initiating solar photocatalysis, a dark reaction was conducted for one day to reach adsorption-desorption equilibrium. During the specified period, the samples will be kept in a dark box and only exposed to ambient light during collection at designated time intervals. Once equilibrium was achieved, the photocatalysis process began by exposing the beakers to sunlight irradiation. All solar experiments were conducted on the UTAR Kampar campus at Block E for 3 hours with a sunlight intensity of 1041 lux. Aliquots were withdrawn every 30 minutes, centrifuged, and the remaining OTC concentration determined by UV-vis spectrophotometry at 274 nm. To evaluate catalyst recyclability, the spent photocatalyst was rinsed with ultrapure water and ethanol, dried overnight at 80 °C, and its crystallinity reassessed to confirm structural integrity. A control experiment was also performed to quantify photolysis of OTC without catalyst.

#### 3.8 Detection of Active Radical Species

A scavenging test was conducted to identify the active radical species involved in the degradation of oxytetracycline (OTC) under sunlight irradiation. This test was necessary due to the presence of active species known to participate in the photocatalytic degradation of OTC. The aim was to assess the photocatalytic effectiveness of the specified photocatalyst in degrading the target pollutant. The active radical species generated during the photocatalytic degradation of OTC include •O<sub>2</sub>-, h<sup>+</sup>, •OH, and e<sup>-</sup>. p-Benzoquinone (BQ), isopropyl alcohol (IPA), and triethylamine (TEA) were used as scavenging agents to capture •O<sub>2</sub>-, h<sup>+</sup>, •OH, and e<sup>-</sup>, respectively. Each scavenging agent was individually examined for its impact on the photocatalytic degradation of BPA. The reaction was conducted using 0.1 mM BQ, 5 mM TEA, and 5 mM IPA solutions, with 10 ppm BPA and a catalyst concentration of 500 mgL<sup>-1</sup>. The results will be analysed by UV-Vis DRS as well.

## 3.9 Stability of Photocatalyst

The stability of the photocatalyst was assessed through a cycling test. In this study, three cycles of photocatalytic degradation were carried out using the same batch of photocatalyst. After each cycle, the photocatalyst was separated from the solution by centrifugation, then washed multiple times with deionised water, and dried overnight at 60°C. The results will be analysed using UV-Vis DRS to evaluate the photocatalyst's efficiency.

#### **CHAPTER 4**

#### RESULTS AND DISCUSSION

## 4.1 Characterization of GCN/BNO Coupled Photocatalysts

## 4.1.1 FESEM-EDX Analysis

FESEM was utilised to examine the microstructure and morphology of the photocatalysts, while EDX was employed to determine their elemental composition. The morphology of the samples was assessed, and the FESEM images represent pure BNO, GCN, and different weight ratios of GCN/BNO for a 10-ppm concentration of OTC.

## g-C<sub>3</sub>N<sub>4</sub>

To provide a comprehensive understanding of the synthesised nanosheets, a high-magnification FESEM image is included alongside the standard FESEM image of the g-C<sub>3</sub>N<sub>4</sub> nanosheets as an inset in **Figures 4.1 and 4.2**. These images offer a detailed visualisation of the nanosheets' surface morphology and structural characteristics. The photocatalyst exhibits a nanosheet microstructure with irregular shapes, like foils and tremella, a finding that aligns with the g-C<sub>3</sub>N<sub>4</sub> structure reported by other researchers (Hak et al., 2020; Hao et al., 2017). Additionally, the EDX spectra and elemental mapping images for carbon (C) and nitrogen (N) are presented in **Figure 4.3a**, providing further insights into the elemental composition and distribution. The EDX spectrum displays prominent peaks corresponding to C and N, with no additional peaks

indicative of impurities, underscoring the high purity of the synthesised g-C<sub>3</sub>N<sub>4</sub> nanosheets. The elemental mapping, shown in **Figures 4.3b** and **4.3c**, reveals a uniform distribution of C atoms (marked in red) and N atoms (marked in blue) across the nanosheets. This even dispersion of key elements not only confirms the successful synthesis of g-C<sub>3</sub>N<sub>4</sub> but also highlights the efficiency of the preparation method, ensuring the nanosheets' suitability for potential applications.

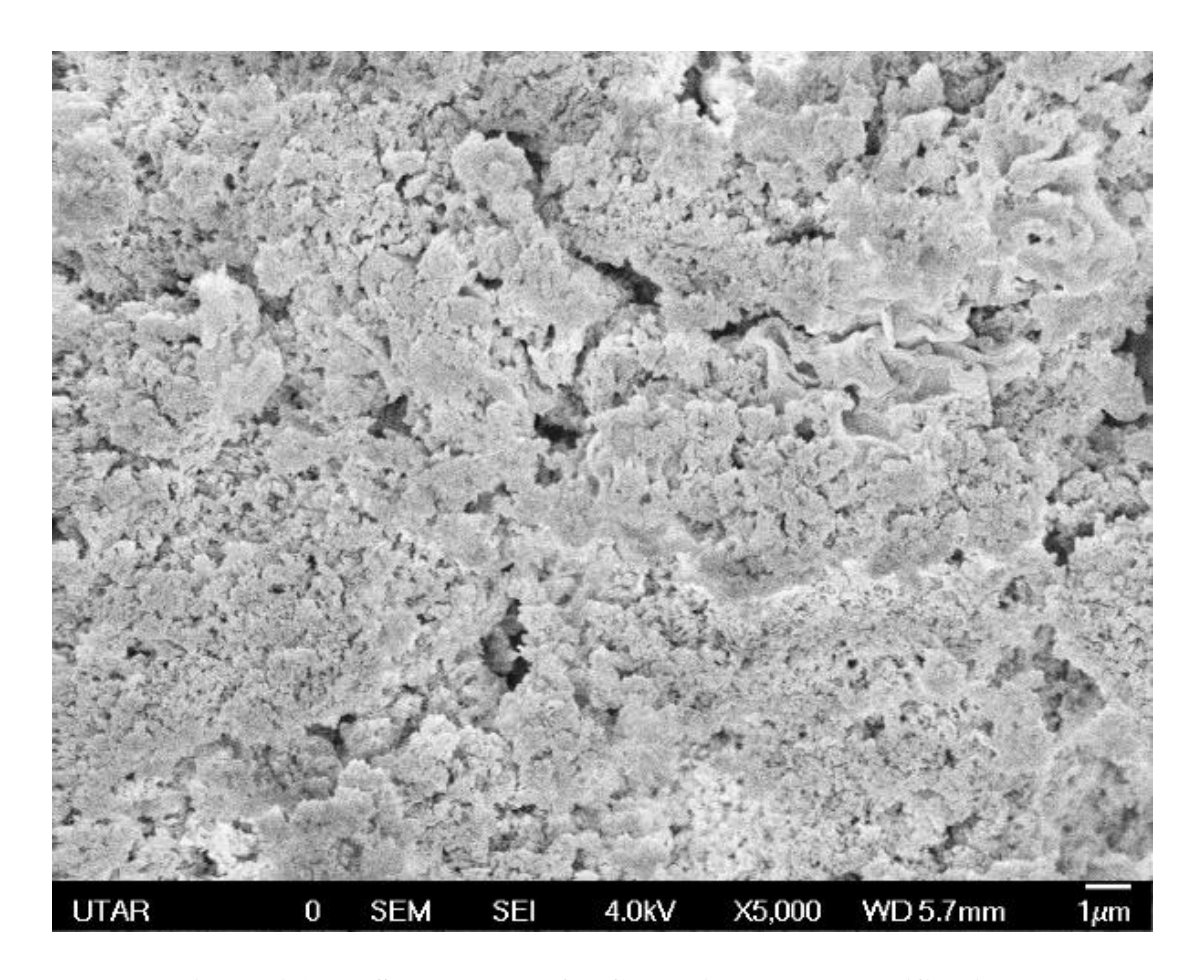


Figure 4.1: FESEM Image of g-C<sub>3</sub>N<sub>4</sub> with 5,000 magnifications

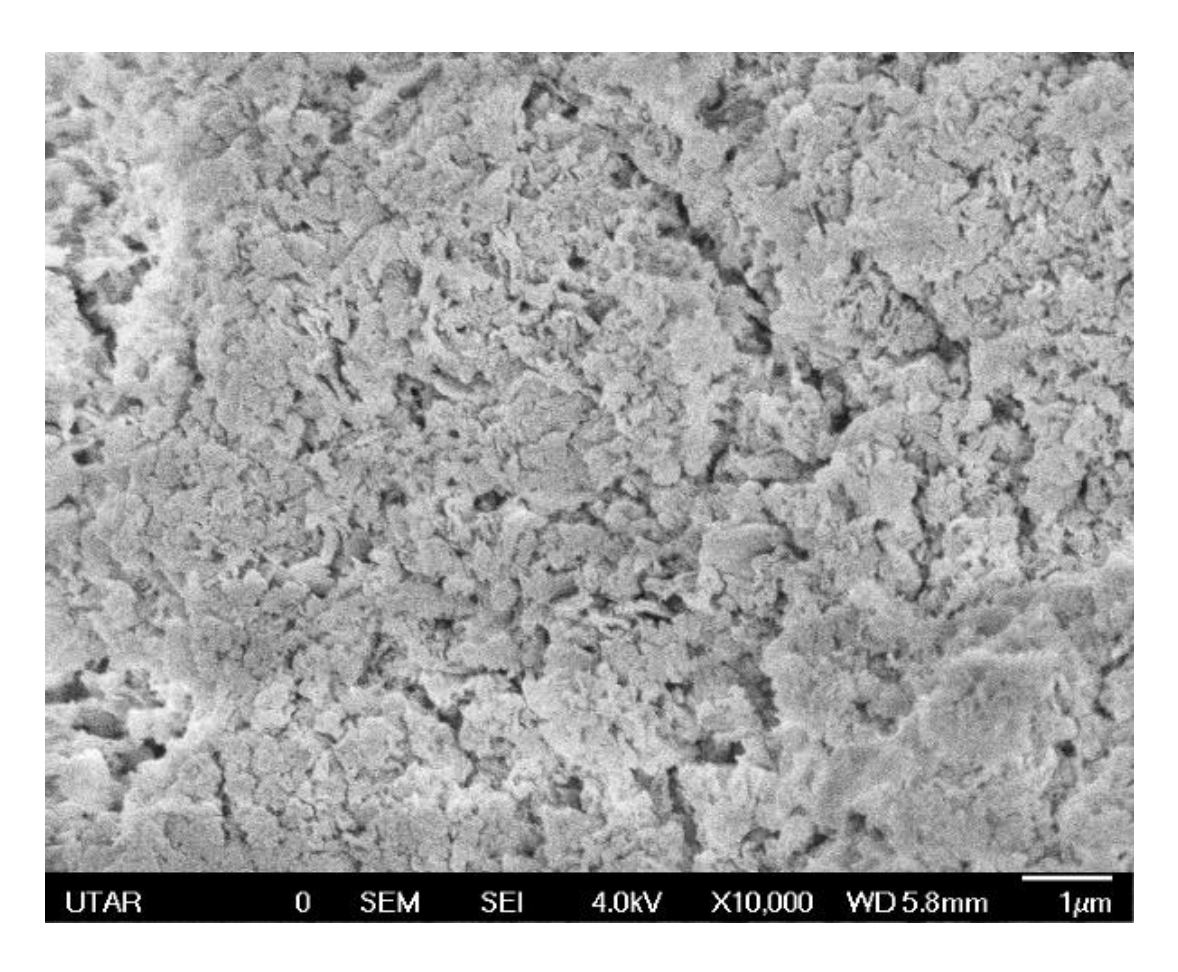


Figure 4.2: FESEM Image of g-C<sub>3</sub>N<sub>4</sub> with 10,000 magnifications

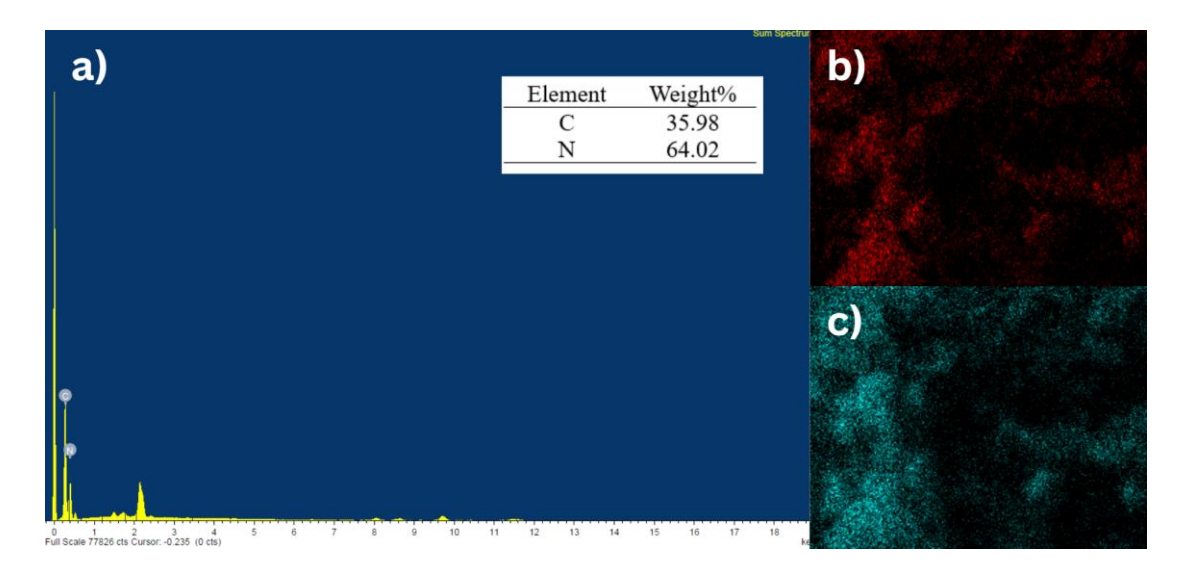


Figure 4.3: a) EDX Analysis of g-C<sub>3</sub>N<sub>4</sub>; b) Element mapping of C; c) Element mapping of N.

#### BiNbO<sub>4</sub>

The morphological features of pure BiNbO<sub>4</sub> were examined using FESEM analysis, as shown in **Figures 4.4 & 4.5**. The high-magnification FESEM image offers detailed insights into the nanosheet structures, highlighting their unique morphology. Additionally, the elemental mapping images and EDX spectra of the BiNbO<sub>4</sub> nanosheets are presented in **Figure 4.6a**. The photocatalyst exhibits a nanosheet microstructure with various morphologies, which may be attributed to its crystalline structure, as mentioned by Hao et al., 2017. The EDX spectrum reveals prominent peaks for oxygen (O), niobium (Nb), and bismuth (Bi), with no detectable impurities, confirming the high purity of the synthesised nanosheets. The elemental mapping, shown in **Figures 4.6b, 4.6c, and 4.6d**, further validates the distribution of these elements, with O atoms marked in red, Bi atoms in green, and Nb atoms in blue. The even distribution of these elements across the nanosheets, as seen in the mapping, supports the successful synthesis of pure BiNbO<sub>4</sub>. This uniform elemental dispersion aligns with the expected stoichiometry of BiNbO<sub>4</sub> and underscores the effectiveness of the synthesis method employed.

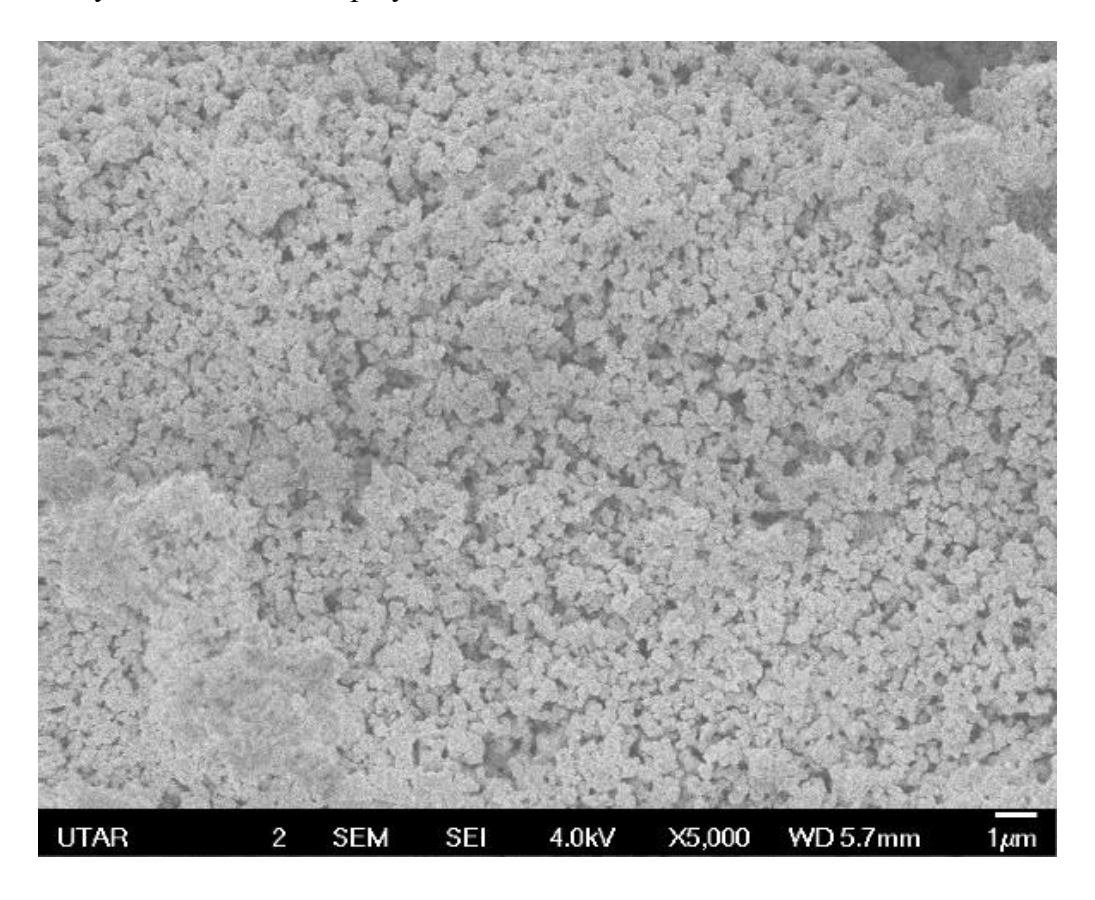


Figure 4.4: FESEM Image of BiNbO<sub>4</sub> with 5,000 magnifications

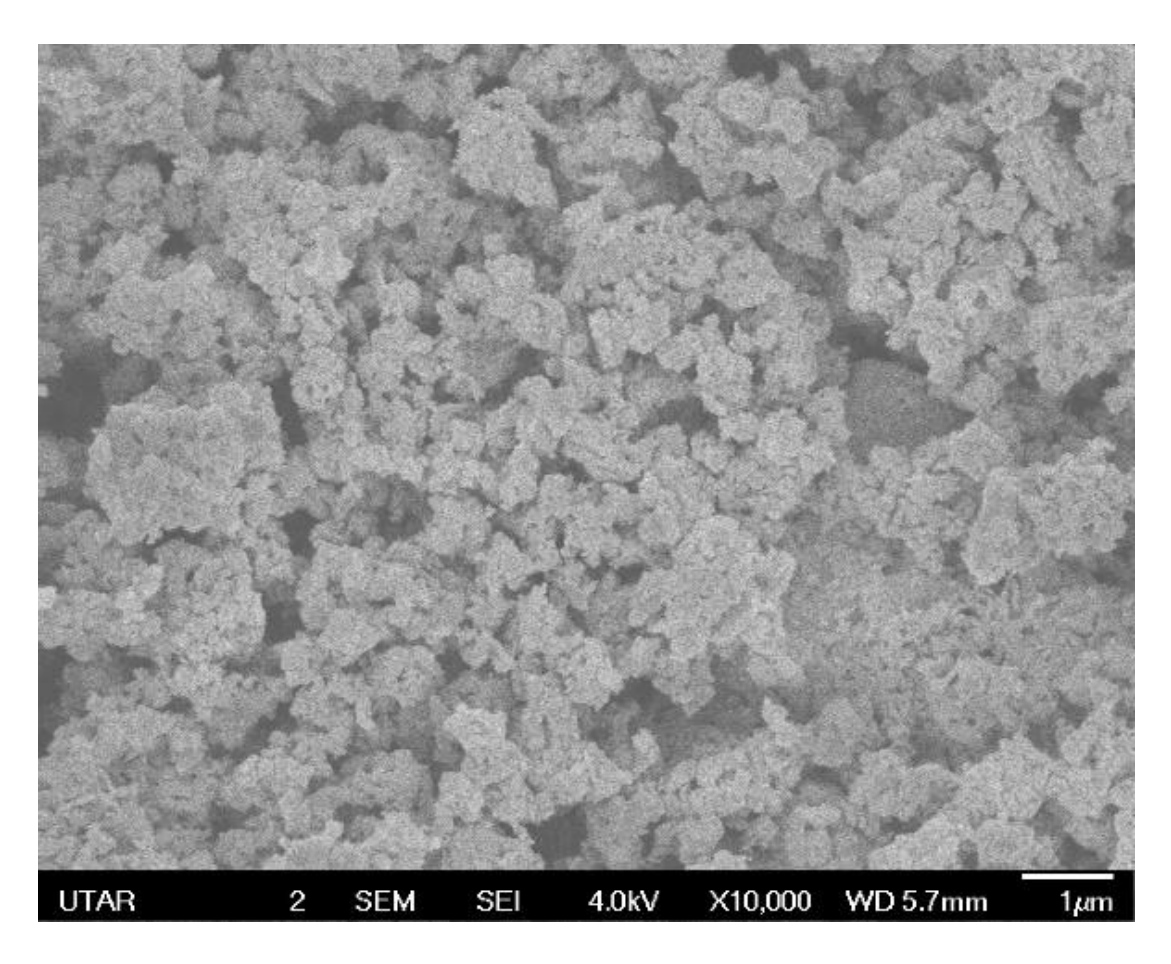


Figure 4.5: FESEM Image of BiNbO<sub>4</sub> with 10,000 magnifications

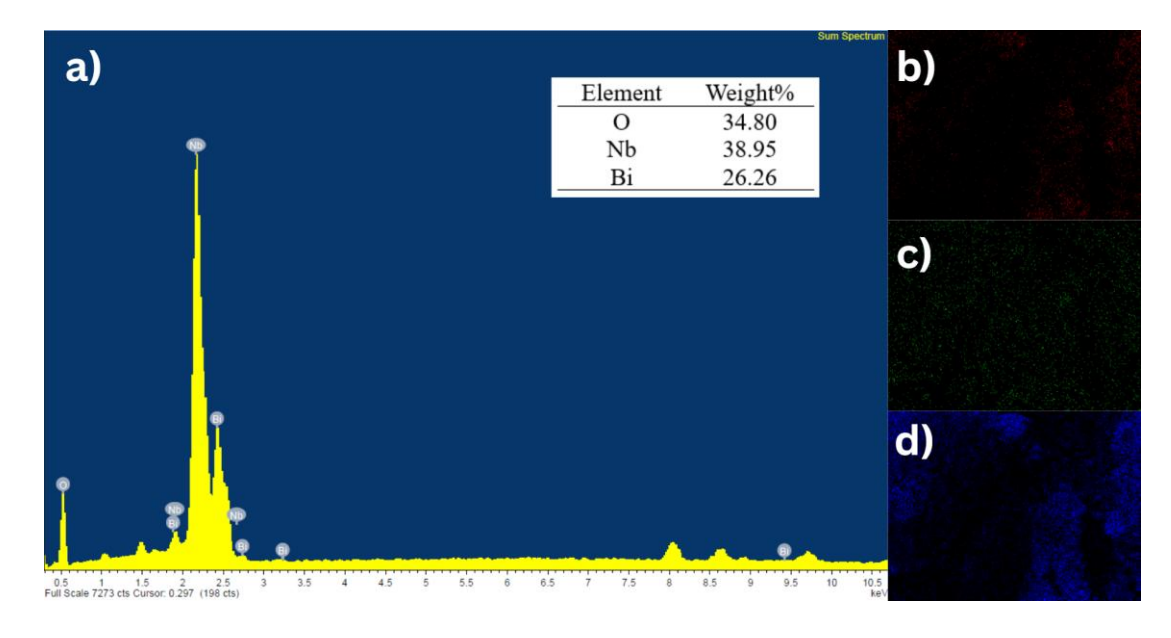


Figure 4.6: a) EDX Analysis of BiNbO<sub>4</sub>; b) Element mapping of O; c) Element mapping of Bi; d) Element mapping of Nb.

## Different Composites of g-C<sub>3</sub>N<sub>4</sub>/BiNbO<sub>4</sub>

The successful synthesis of nanostructured GCN/BNO with relatively uniform diameters is illustrated in the FESEM images of GCN/BNO nanosheets at various ratios, shown in Figures 4.7 to 4.12. High-magnification FESEM images, included as insets in these figures, provide additional details about the morphology and structural features of the synthesised nanosheets. It can be shown that the microstructure of the composites exhibits a mixing of irregular shapes of GCN nanoplates and irregular crystalline structure of BNO, which clearly indicated that both composites are coupled successfully. Figures 4.13a to 4.15a present the elemental mapping images and EDX spectra for the (x) GCN/BNO composites, where x = 0.3, 0.5, 0.7. The EDX spectra reveal intense peaks corresponding to carbon (C), nitrogen (N), oxygen (O), bismuth (Bi), and niobium (Nb), with no evidence of impurities, confirming the high purity of the synthesised composites. Elemental mapping, shown in the insets of Figures 4.13 to 4.15, highlights the distribution of C, N, O, Bi, and Nb atoms. The even and consistent mapping of these elements across the nanosheets further supports the effective synthesis of GCN/BNO and ensures their uniform composition, making them suitable for various applications.

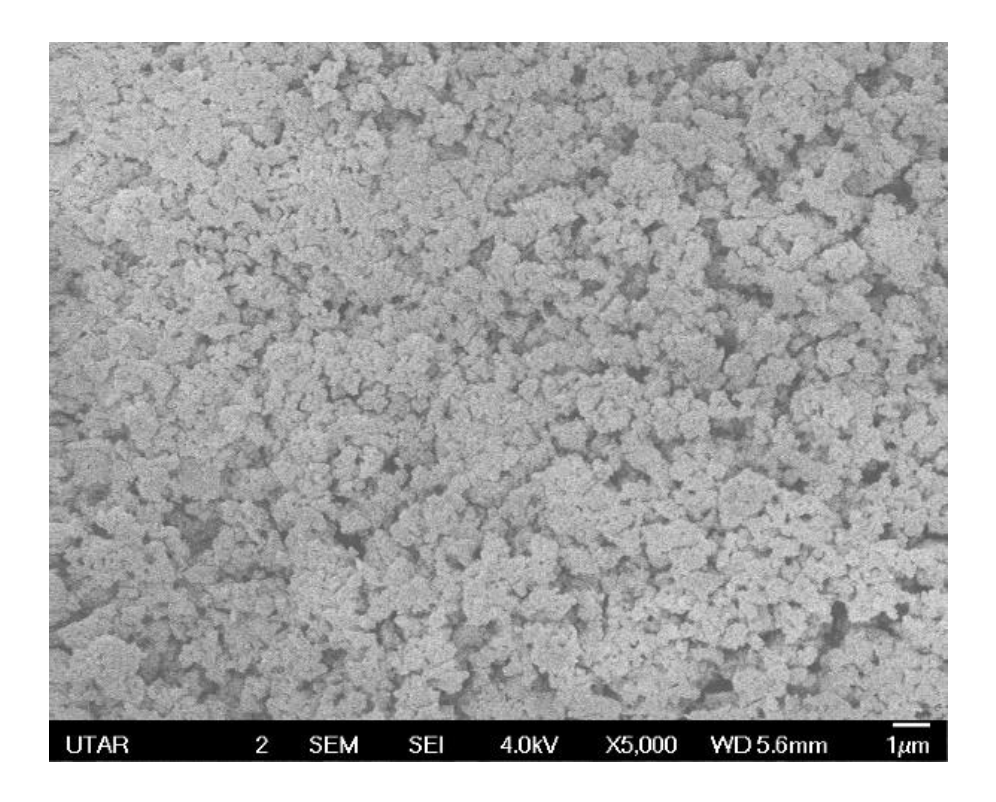


Figure 4.7: FESEM Image of 0.3 GCN/BNO with 5,000 magnifications

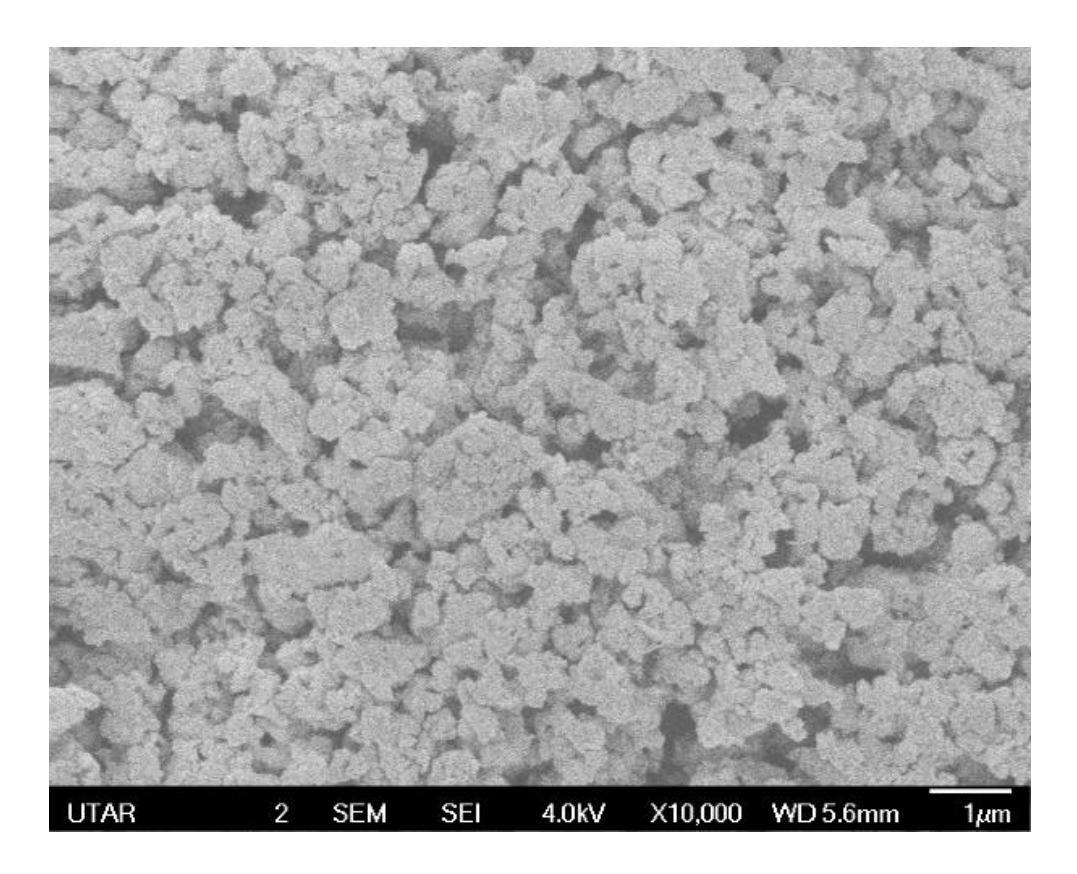


Figure 4.8: FESEM Image of 0.3 GCN/BNO with 10,000 magnifications

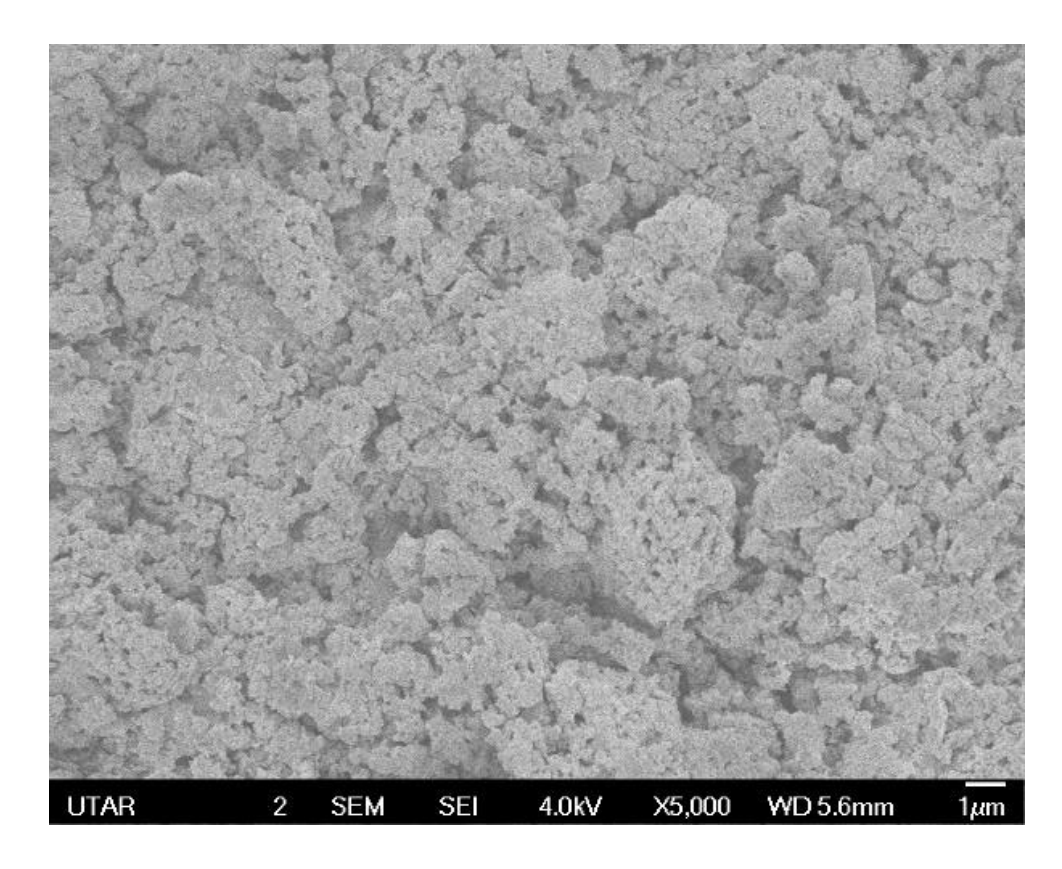


Figure 4.9: FESEM Image of 0.5 GCN/BNO with 5,000 magnifications

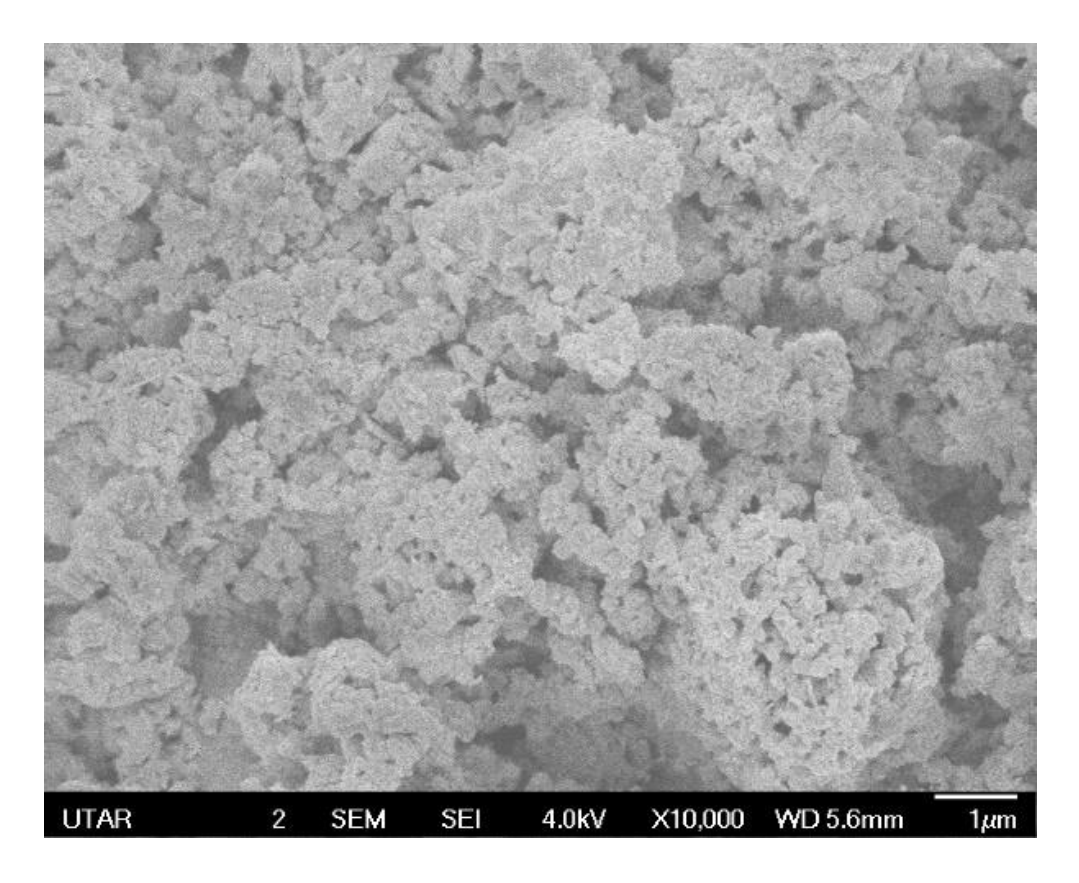


Figure 4.10: FESEM Image of 0.5 GCN/BNO with 10,000 magnifications

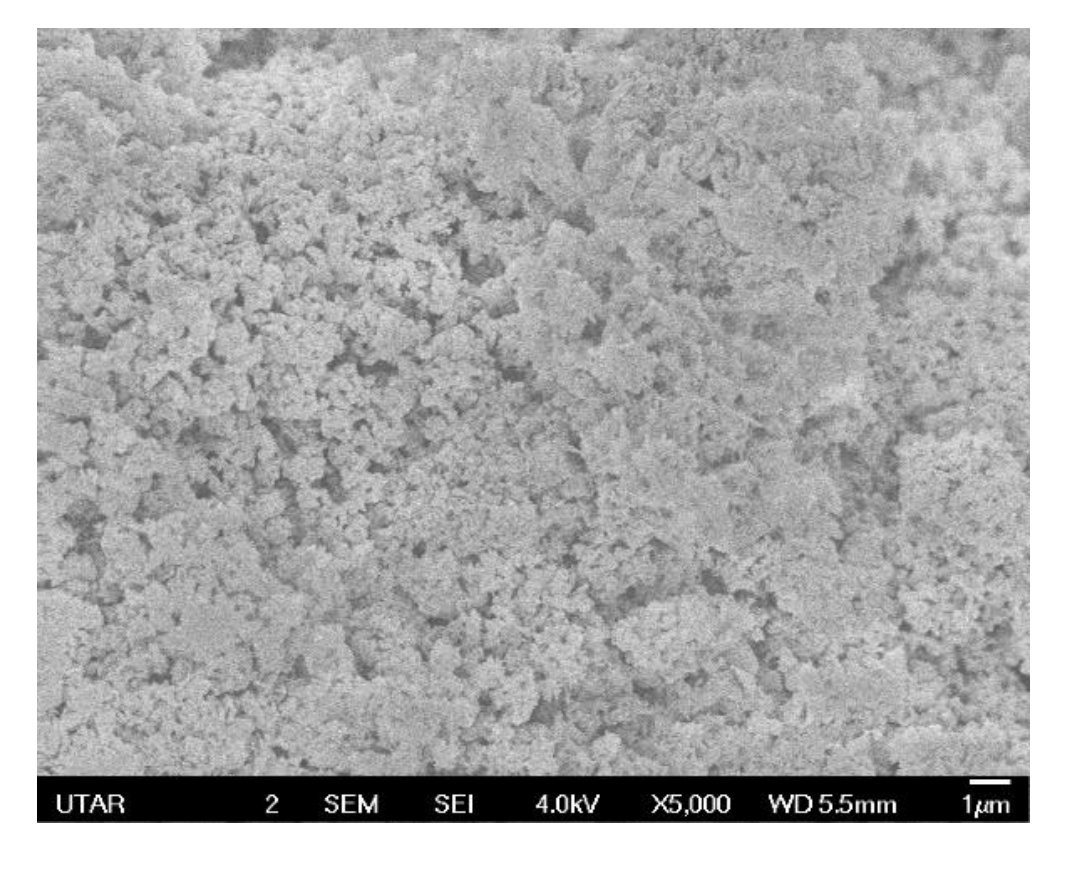


Figure 4.11: FESEM Image of 0.7 GCN/BNO with 5,000 magnifications

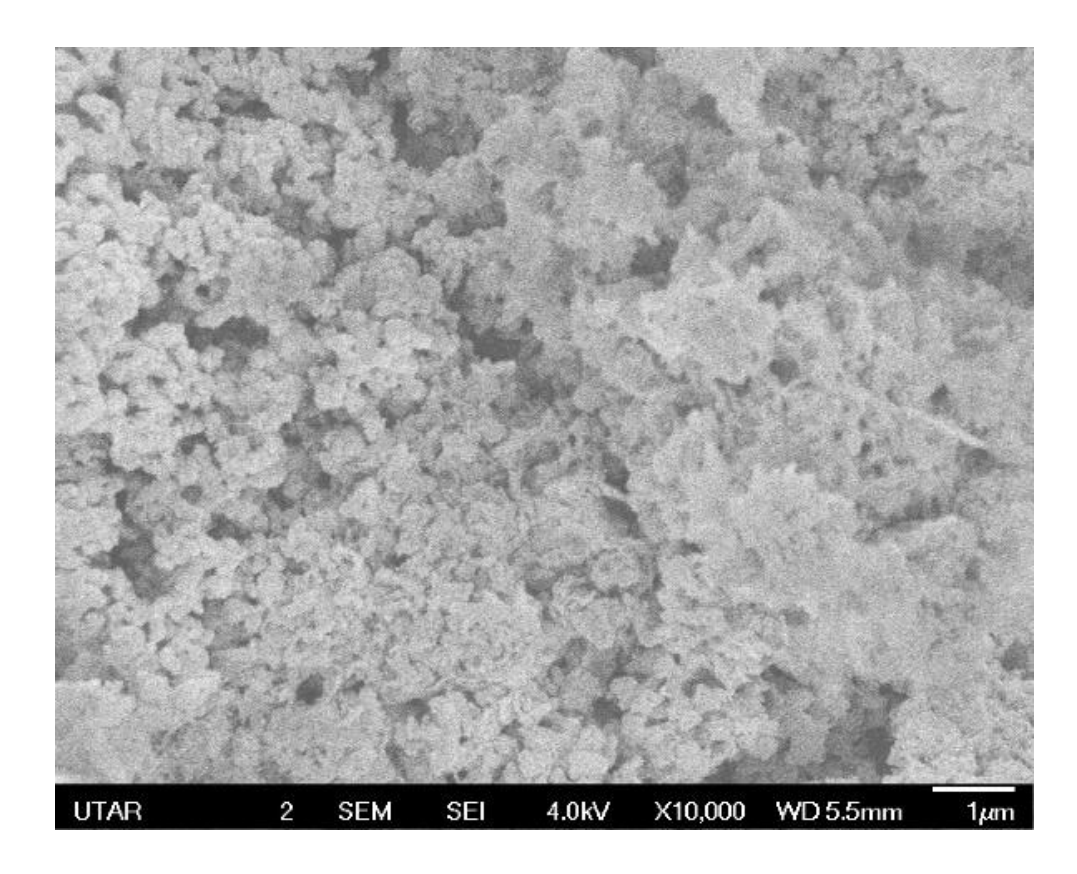


Figure 4.12: FESEM Image of 0.7 GCN/BNO with 10,000 magnifications

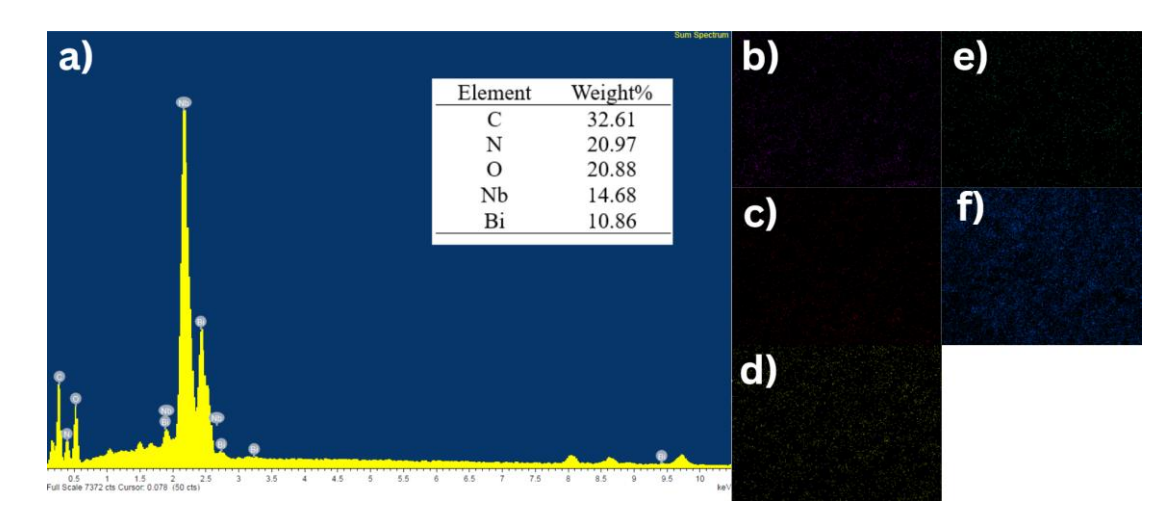


Figure 4.13: a) EDX Analysis of 0.3 GCN/BNO; b) Element mapping of C; c)

Element mapping of N; d) Element mapping of O; e) Element mapping of Bi; f)

Element mapping of Nb

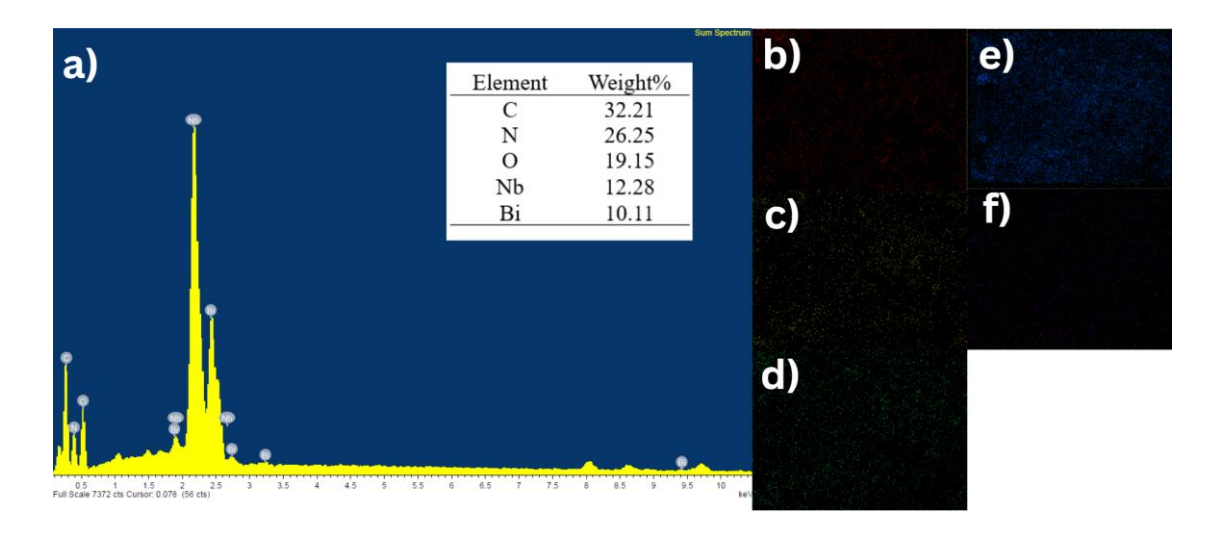


Figure 414: a) EDX Analysis of 0.5 GCN/BNO; b) Element mapping of C; c)

Element mapping of N; d) Element mapping of O; e) Element mapping of Bi; f)

Element mapping of Nb

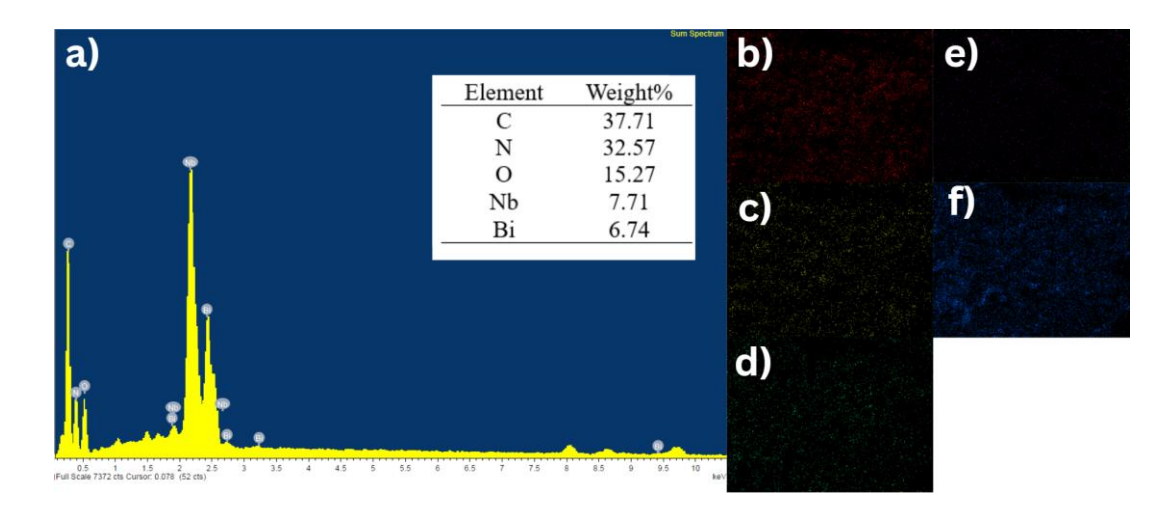


Figure 4.15: a) EDX Analysis of 0.7 GCN/BNO; b) Element mapping of C; c)

Element mapping of N; d) Element mapping of O; e) Element mapping of Bi; f)

Element mapping of Nb

## 4.1.2 X-Ray Diffraction Analysis

The crystallographic properties of the heterostructures with varying BiNbO<sub>4</sub> (BNO) and g-C<sub>3</sub>N<sub>4</sub> (GCN) compositions are illustrated in **Figure 4.16**. The XRD pattern of GCN matches ICDD card No. 01-087-1526, displaying prominent peaks at 13.35° and 27.48°. The 13.35° reflection (001) reveals a 0.66 nm in-plane arrangement of tri-striazine units, while the 27.48° peak (002) corresponds to the interlayer stacking distance of aromatic segments (Bellamkonda et al., 2019). This confirms that both materials retain their intrinsic crystalline order within the composite, which allows for the intimate contact between the two phases (Hao et al., 2017). This means more charge carriers are available to drive redox reactions, which accelerates the degradation process.

The diffraction pattern of BiNbO<sub>4</sub> aligns closely with ICDD No. 00-043-0444 (Bi<sub>7.84</sub>Nb<sub>0.16</sub>O<sub>12.16</sub>), which is associated with the orthorhombic α-phase of BiNbO<sub>4</sub>. This phase is stable at room temperature and is characterised by a distorted arrangement of Bi, Nb, and O atoms in its crystal lattice, which gives rise to its unique structural properties. The observed diffraction peaks at 27.99°, 46.25°, 47.02°, 54.27°, 55.52°, 57.8°, 68.52°, 74.52°, and 75.74° correspond to the (201), (222), (400), (203), (213), (402), (114), (423), and (601) planes, respectively, confirming the well-defined crystallinity of the α-phase (Rani et al., 2024). The orthorhombic symmetry introduces anisotropy in the material's physical properties, meaning that charge carriers may travel preferentially along certain directions (Meera et al., 2024). This anisotropic behaviour can create effective pathways for charge transport, enhancing the overall photocatalytic activity by enabling fast migration of electrons and holes to the reaction sites (Luo et al., 2022). The presence of these well-defined peaks suggests long-range order in the crystal lattice. Such order typically correlates with fewer defects that might otherwise trap charge carriers. Instead, the charges can travel through the crystal lattice more freely, reaching reactive sites quickly (Schober et al., 2016; Guerrini et al., 2021).

The XRD patterns of the g-C<sub>3</sub>N<sub>4</sub> / BiNbO<sub>4</sub> composites in their raw state reveal a combination of orthorhombic α-phase of BiNbO<sub>4</sub> and hexagonal g-C<sub>3</sub>N<sub>4</sub> phases. The detected diffraction peaks correspond to the presence of BiNbO<sub>4</sub> within the synthesised g-C<sub>3</sub>N<sub>4</sub> / BiNbO<sub>4</sub> composites. These peaks were progressively weakened and broadened with an increasing g-C<sub>3</sub>N<sub>4</sub> phase, as the structure of BiNbO<sub>4</sub> became

increasingly integrated with the thin g-C<sub>3</sub>N<sub>4</sub> layer. This integration resulted in a steady decline in the intensity of the BiNbO<sub>4</sub> peaks, indicating the gradual lamination of g-C<sub>3</sub>N<sub>4</sub> onto the surface of BiNbO<sub>4</sub>. The composite benefits from both the layered structure of g-C<sub>3</sub>N<sub>4</sub>, which provides a high surface area and active sites, and the unique anisotropic charge transport properties of BiNbO<sub>4</sub>. The synergy between these components means that the heterojunction not only enhances charge separation but also facilitates the rapid generation of reactive species like hydroxyl radicals that are critical for the degradation of pollutants (Sun et al., 2010).

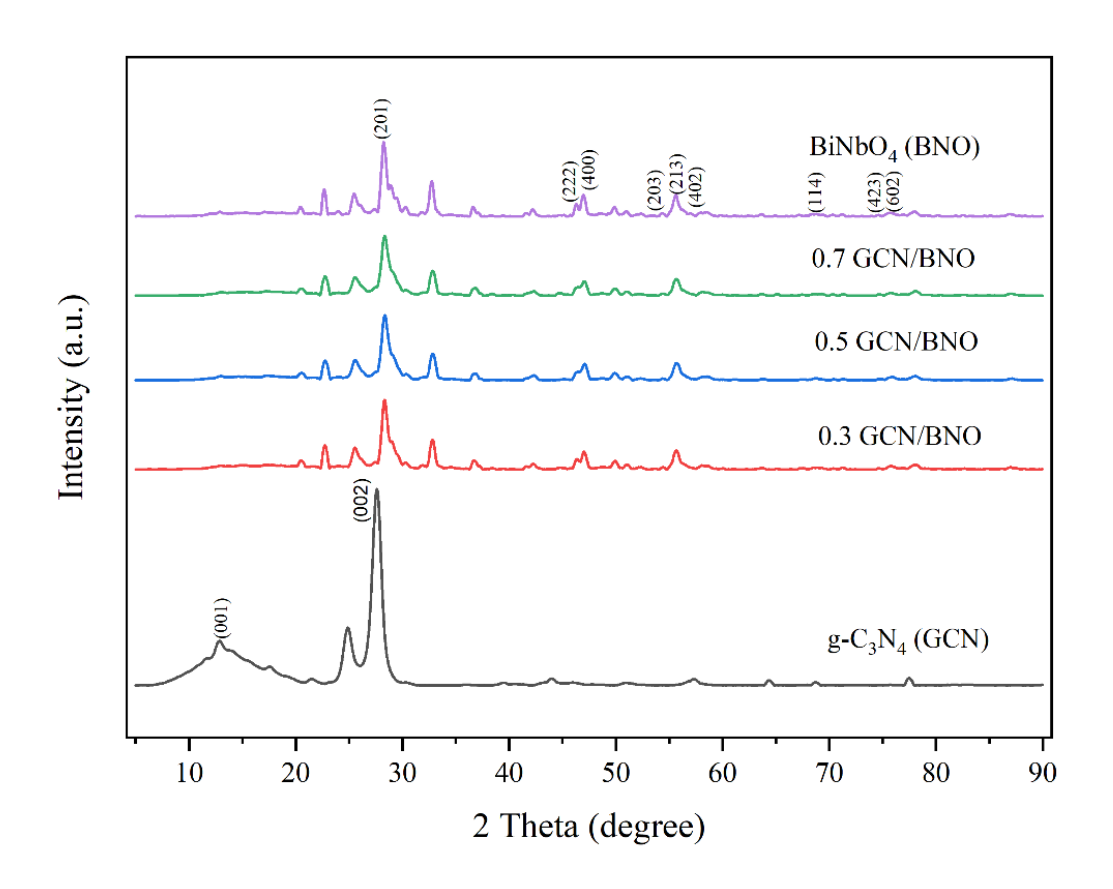


Figure 4.16: XRD patterns of Pure BNO, Pure GCN, and Different Ratio of GCN/BNO

#### 4.1.3 FTIR Analysis

The functional groups of g-C<sub>3</sub>N<sub>4</sub> and BiNbO<sub>4</sub> were determined through Fourier Transform Infrared Spectroscopy (FTIR) as shown in Figure 4.17. The FTIR spectrum of g-C<sub>3</sub>N<sub>4</sub> displays a distinct peak at 808 cm<sup>-1</sup>, representing its characteristic band attributed to the s-triazine ring vibrations (Ishak et al., 2023). The band at 1628 cm<sup>-1</sup> is attributed to C–N stretching, while the bands at 1570 cm<sup>-1</sup> and 1455 cm<sup>-1</sup> correspond to the stretching vibration modes of C-N heterocycles (Li et al., 2009; Yang et al., 2015; Dong et al., 2012). Both structures offer a high surface area and an appropriate band structure for visible-light absorption (Chang et al., 2023). Apart from that, the bands at 1234 cm<sup>-1</sup> and 1392 cm<sup>-1</sup> are associated with the vibrations of C-NH-C linked units (Yang et al., 2016). Additionally, all four samples with g-C<sub>3</sub>N<sub>4</sub> exhibited a broad band in the 3000–3500 cm<sup>-1</sup> range, attributed to N-H and O-H groups (Yan et al., 2009). The presence of N–H groups contribute to the formation of hydrogen bonds, which can stabilise the adsorption of water or pollutants on the surface (Zhu et al., 2021). For BiNbO<sub>4</sub>, the peak at 1392 cm<sup>-1</sup> corresponds to the O-H stretching vibrations of carboxyl groups (Zanetti et al., 2004). These hydroxyl groups are not merely structural features but serve as active sites on the surface of the composite. Under illumination, the absorbed photons excite electrons, and these photogenerated holes can interact with the surface –OH groups or adsorbed water molecules to produce highly reactive •OH radicals (Sun et al., 2010). These radicals are among the most potent oxidising agents, capable of breaking down complex organic molecules rapidly. On the other hand, the absorption bands near 808 cm<sup>-1</sup> and 547 cm<sup>-1</sup> are attributed to the NbO<sub>6</sub> octahedron, as noted in reported IR spectra of niobates (Liu et al., 2003). The FTIR spectra of the g-C<sub>3</sub>N<sub>4</sub>/BiNbO<sub>4</sub> composites closely resemble those of individual g-C<sub>3</sub>N<sub>4</sub> and BiNbO<sub>4</sub>, confirming that the composite contains both components. Since g-C<sub>3</sub>N<sub>4</sub> is known for its ability to absorb visible light and generate electron-hole pairs, when combined with BiNbO<sub>4</sub>, which also has semiconducting properties that are evidenced by its NbO<sub>6</sub> octahedral structure, a heterojunction is formed. This junction facilitates the effective separation and migration of electrons and holes, reducing their recombination rate (Goodarzi et al., 2023).

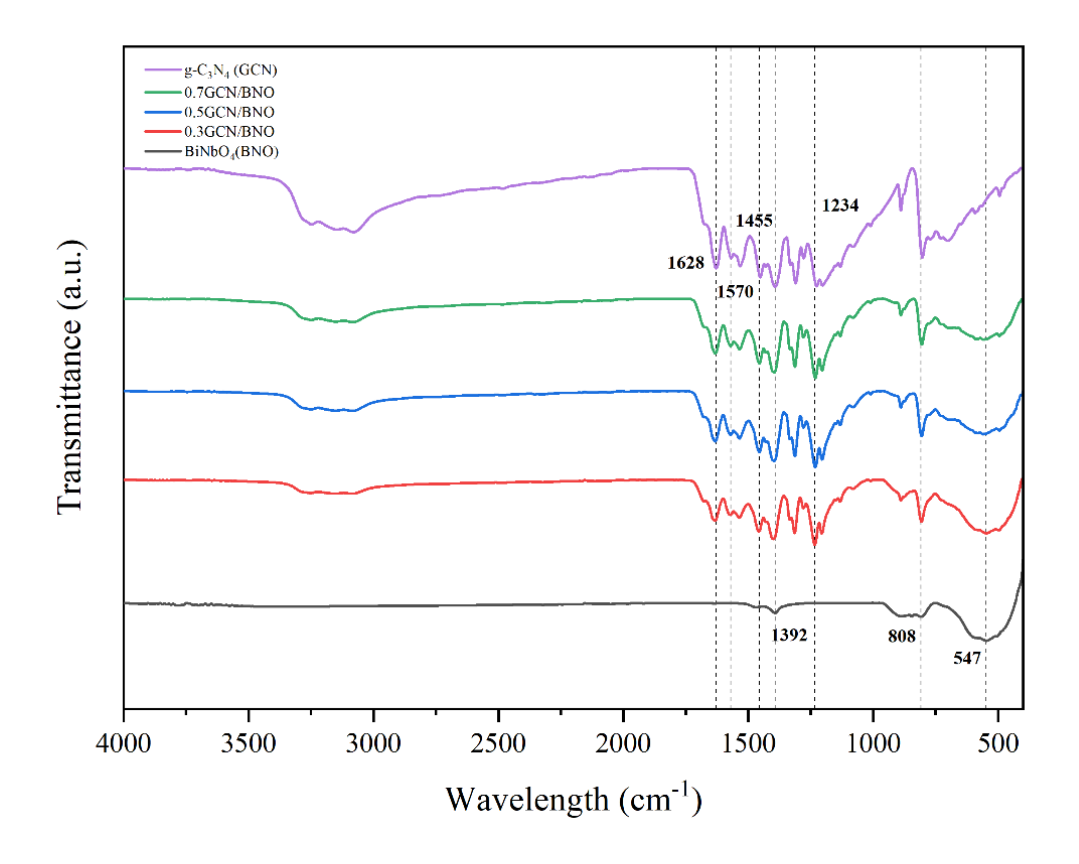
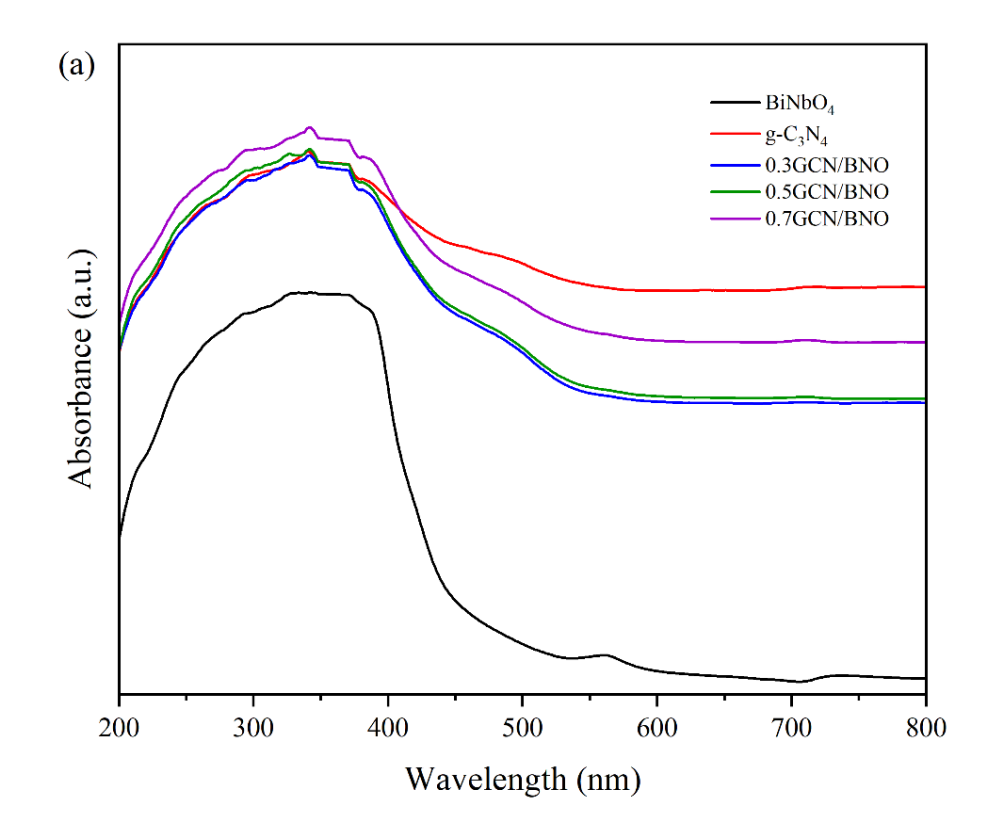


Figure 4.17: FTIR Spectra of Pure BNO, Pure GCN, and Different Ratio of GCN/BNO

#### 4.1.4 UV-Vis DRS Analysis

Figure 4.18(a) presents the UV–DRS absorption spectra for the materials under study. All samples were found to absorb visible light, with the three composites showing a more pronounced visible light edge than BNO and closely resembling GCN. BNO absorbed light effectively up to 450 nm, while GCN and the composites extended absorption up to more than 800 nm, proving that they have a high absorbance intensity even in the infrared light spectrum. This enables the composites to capture a broader portion of the solar spectrum, including the lower-energy photons that constitute a significant part of sunlight. This extended absorption range enhances the generation of charge carriers (electrons and holes) needed to drive photocatalytic reactions for pollutant degradation. By effectively harnessing infrared light, the composites can convert more solar energy into chemical energy, thereby improving overall efficiency and performance in practical applications. The formation of coupled composites also resulted in a shift of the spectral peak of g-C<sub>3</sub>N<sub>4</sub>/BiNbO<sub>4</sub> toward a higher absorbance intensity at the same wavelength.

The band gaps of BNO and the composites, determined from the Tauc plot as shown in **Figure 4.18(b)**, were approximately 2.87 eV for BNO, 2.85 eV for 0.3GCN/BNO, 2.83 eV for 0.5GCN/BNO, and 2.81 eV for 0.7GCN/BNO. Conversely, g-C<sub>3</sub>N<sub>4</sub>, which possesses an indirect band gap, exhibited a band-gap value of about 2.74 eV. This improvement enhances absorbance in the visible light and infrared light spectrum, as the coupled photocatalysts possess a lower band gap energy than pure BNO. The band-gap energy determined for pure BNO is similar to the values reported in other studies (Alcântara et al., 2018). In a similar manner, the band-gap energy calculated for GCN in this work closely corresponds to the 2.7 eV value found by other researchers (Chidhambaram and Ravichandran, 2017).



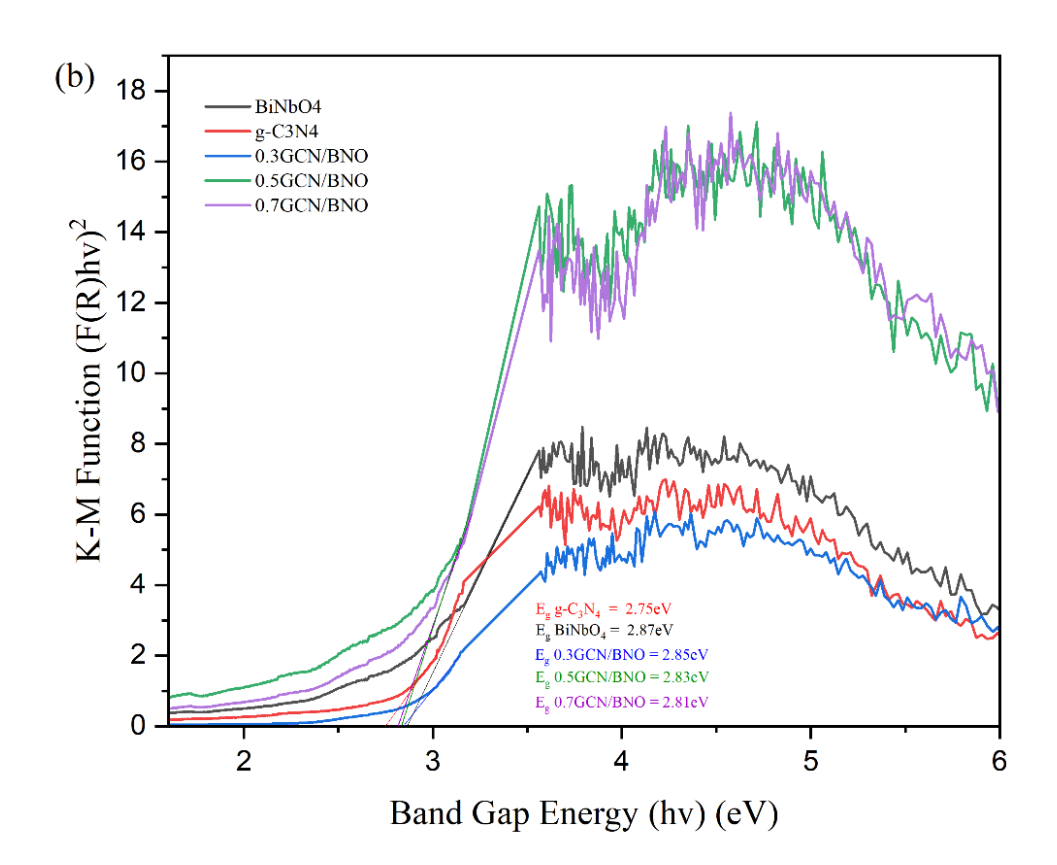


Figure 4.18: (a) UV-Vis DRS Spectrum of GCN, BNO, and composites of GCN/BNO and (b) Band Gap by Tauc Plot

#### 4.2 Photocatalytic Degradation of OTC under Sunlight

The study evaluates how effectively pure BiNbO<sub>4</sub> (BNO) and various composites of g-C<sub>3</sub>N<sub>4</sub> with BNO (denoted as GCN/BNO) break down oxytetracycline (OTC) when exposed to sunlight. As illustrated in **Figure 4.19**, the degradation rates of OTC were measured for pure GCN, 0.3 GCN/BNO, 0.5 GCN/BOC, 0.7 GCN/BNO, pure BNO, and a control sample without any photocatalyst over a 3-hour period. Initially, all samples underwent a 24-hour dark reaction to achieve adsorption–desorption equilibrium, ensuring the OTC concentration—set at 20 ppm—remained stable. Minor fluctuations during this dark phase, seen in **Figure 4.19**, are attributed to the OTC adsorbing onto the photocatalyst surfaces.

When exposed to sunlight (as shown in **Figure 4.20**), the 0.3 GCN/BNO composite outperformed the others by reaching the highest efficiency of 98%, followed by the 0.5 GCN/BNO (92.5%) and 0.7 GCN/BNO (85%), then pure GCN and pure BNO, with the blank sample showing negligible change. This further confirms that GCN/BNO composites enhance degradation compared to pure GCN and pure BNO, which primarily absorb UV light. Meanwhile, the unchanged OTC level in the blank sample confirms that OTC does not self-degrade under sunlight.

Moreover, the overall results demonstrate that coupling g-C<sub>3</sub>N<sub>4</sub> with BiNbO<sub>4</sub> improves the photocatalytic performance by lowering BNO's and GCN's high band gap energy, thereby boosting visible light absorption and slowing down the recombination of photoexcited charges. However, an excessive amount of g-C<sub>3</sub>N<sub>4</sub> can counteract this benefit by increasing the recombination rate of photogenerated electron–hole pairs, thereby reducing the overall production of reactive species needed for efficient degradation (Mamba et al., 2016). Higher amounts of g-C<sub>3</sub>N<sub>4</sub> also lead to increased light scattering (Jiang et al., 2020). This scattering prevents the light from penetrating deeply into the composite, reducing the number of photons reaching the active sites where photocatalytic reactions occur. Consequently, a ratio of 0.3g g-C<sub>3</sub>N<sub>4</sub> to 1g BNO is identified as optimal for achieving the highest OTC degradation efficiency, although 0.5 GCN/BNO and 0.7 GCN/BNO exhibits a higher absorbance intensity in the UV-Vis DRS, as shown in **Figure 4.18** (a).

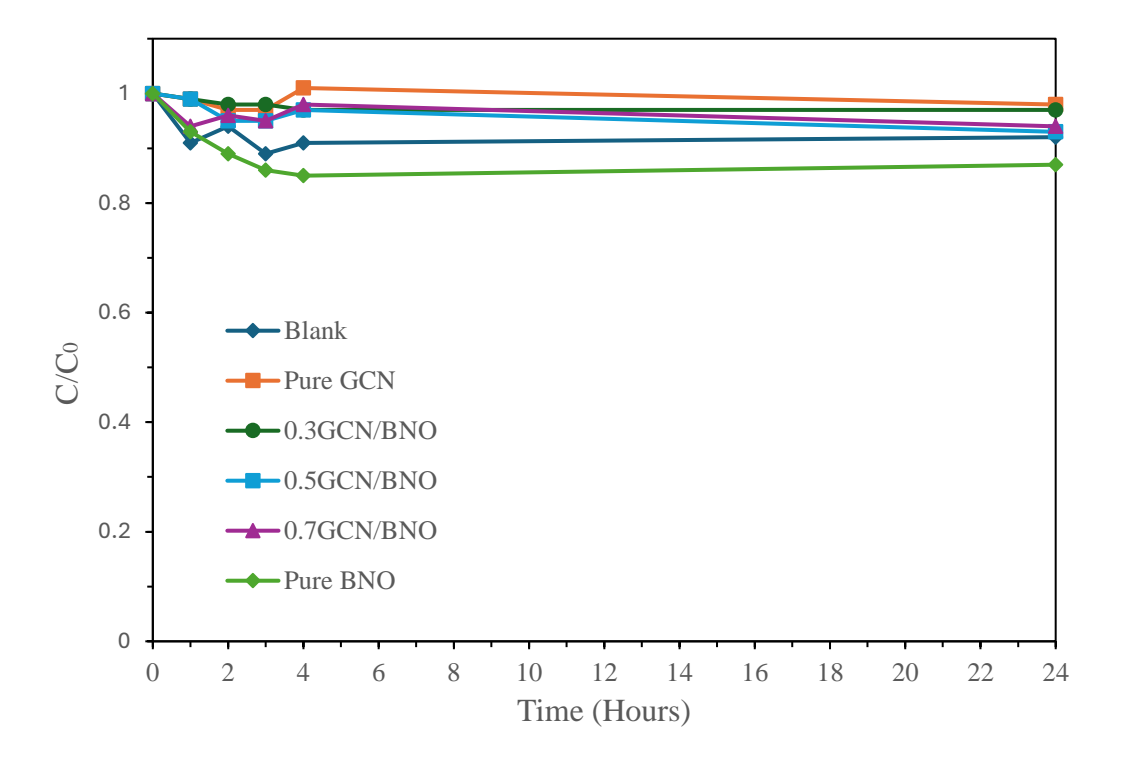


Figure 4.19: Dark reaction for 20ppm OTC

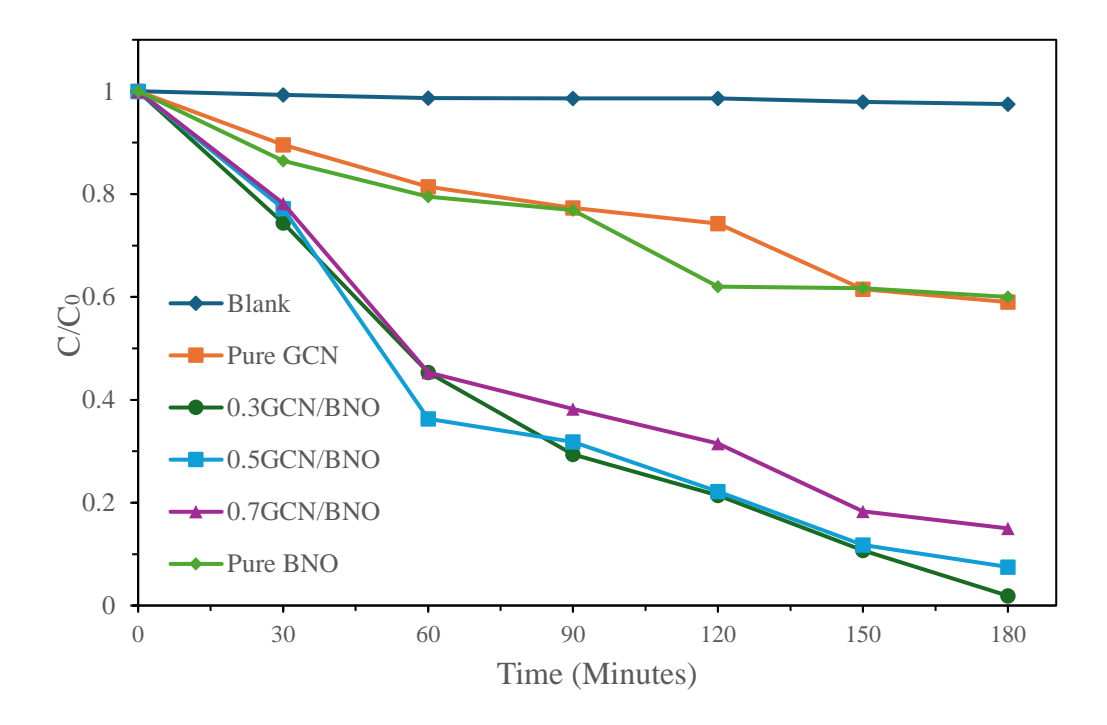


Figure 4.20: Light reaction for 20ppm OTC

## 4.3 Degradation Kinetics Model

The degradation capacity was first calculated using the Eq. (4.1) as described by Yang et al., (2022):

$$q_t = (C_i - C_e) \times \frac{V}{m} \tag{4.1}$$

Where  $C_i$  represents the initial concentration,  $C_e$  represents the equilibrium concentration, V represents the volume, and m represents the mass of the absorbent.

Two different kinetics models, pseudo-first order and pseudo-second order were then fitted to identify the most suitable model, as shown in **Figure 4.21**, with their equations provided in the table (Yang et al., 2022). Since the correlation coefficient ( $R^2$ ) of both models was relatively similar in the 0.99 region, the chi-square ( $x^2$ ) was also employed to identify the best fitting model. From the table shown in the graph, the pseudo-first order was proved to be the most suitable model, as it exhibits a higher  $R^2$  and a lower  $x^2$  to describe the adsorption mechanism.

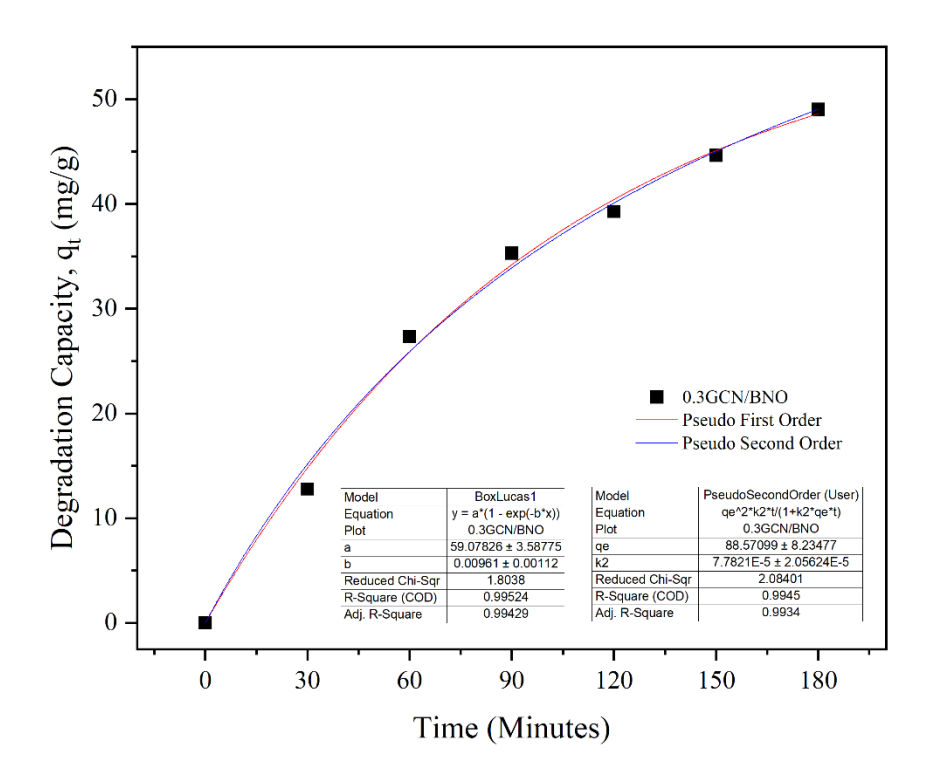


Figure 4.21: Non-linear kinetic models for the degradation of OTC using 0.3GCN/BNO

## 4.4 Determination of Active Radical Species

Scavenging tests provide valuable insight into the degradation mechanism of oxytetracycline (OTC) using the g-C<sub>3</sub>N<sub>4</sub>/BiNbO<sub>4</sub> photocatalyst. By analysing how the addition of specific scavengers affects OTC's photocatalytic breakdown, the primary reactive radical species involved can be identified. In this study, potassium dichromate (K<sub>2</sub>Cr<sub>2</sub>O<sub>7</sub>), triethylamine (TEA), iso-propyl alcohol (IPA), and p-benzoquinone (BQ) were employed as scavengers for electrons (e<sup>-</sup>), holes (h<sup>+</sup>), hydroxyl radicals (•OH), and superoxide anion radicals (•O<sub>2</sub><sup>-</sup>), respectively. **Figure 4.22** illustrates the influence of these scavengers on the photocatalytic degradation of OTC using a photocatalyst composed of 0.3 GCN/BNO.

A faster reaction was observed for the 0.3GCN/BNO catalyst when TEA and IPA were added as scavengers. Hao et al. (2017) reported a similar finding, noting that using a hole scavenger increased the reaction rate. This suggests that TEA, by capturing holes, prevents charge-carrier recombination, thereby increasing the number of electrons available at the conduction band of 0.3GCN/BNO for generating \*O2<sup>-</sup> radicals. Likewise, IPA functions in a comparable way to TEA; both serve as sacrificial agents whose continual consumption at the valence band further promotes enhanced superoxide radical production at the conduction band (Rani et al., 2024). On the other hand, K<sub>2</sub>Cr<sub>2</sub>O<sub>7</sub> had a minor impact on OTC degradation, suggesting that electrons were active in the photocatalytic reaction but not the primary active species. In contrast, the significant reduction in OTC degradation observed with BQ shows that superoxide anion radicals play the predominant role.

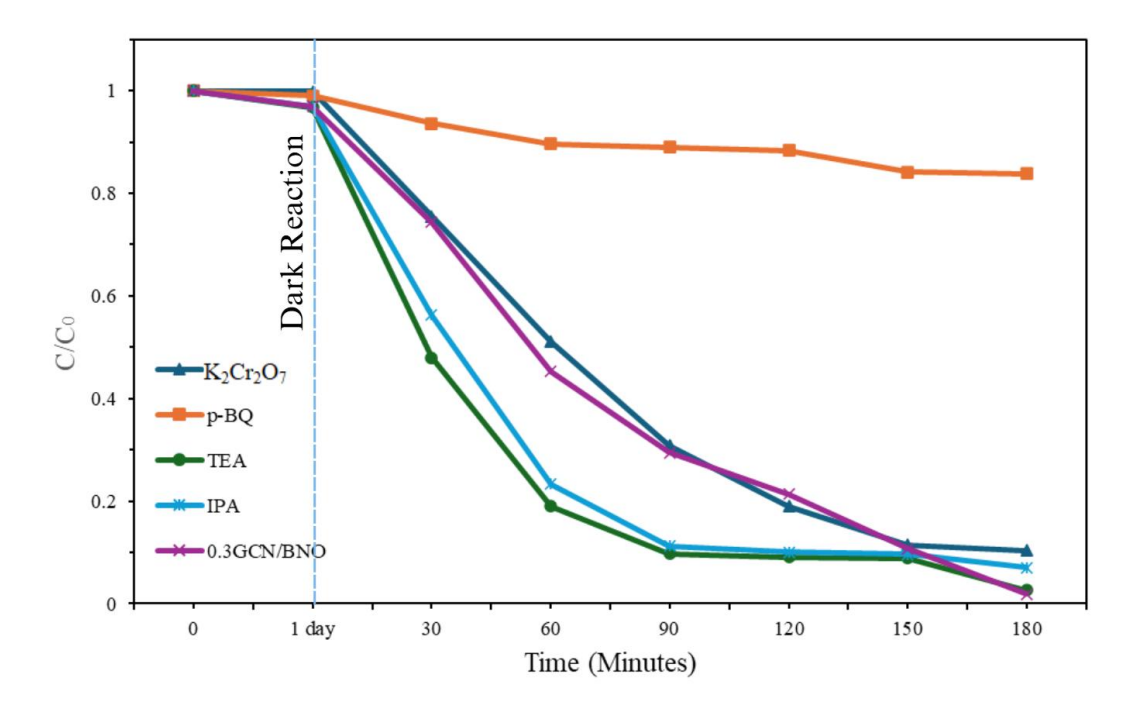


Figure 4.22: Effect of scavenging agent on degradation of OTC

## **4.5 Cycling Test**

A cycling test was carried out to assess the stability of the g-C<sub>3</sub>N<sub>4</sub>/BiNbO<sub>4</sub> photocatalyst using the 0.3 GCN/BNO composite, which exhibited the highest degradation efficiency among the composites tested. As illustrated in **Figure 4.23**, the degradation efficiency of g-C<sub>3</sub>N<sub>4</sub>/BiNbO<sub>4</sub> varied over several cycles: it initially decreased from 98.14% to 95.85%, then to 89.82% by the third cycle. This variation may be due to a relatively lower average light intensity during the second and third cycles, which likely affected the formation of certain light-dependent active species (Zhong et al., 2021). Despite this fluctuation, all three cycles produced favourable outcomes, achieving a 94.6% degradation efficiency for OTC on average. The slight drop in performance observed might also result from some loss of photocatalyst during the subsequent washing process. In conclusion, the g-C<sub>3</sub>N<sub>4</sub>/BiNbO<sub>4</sub> photocatalyst has demonstrated its stability throughout the cycling tests.

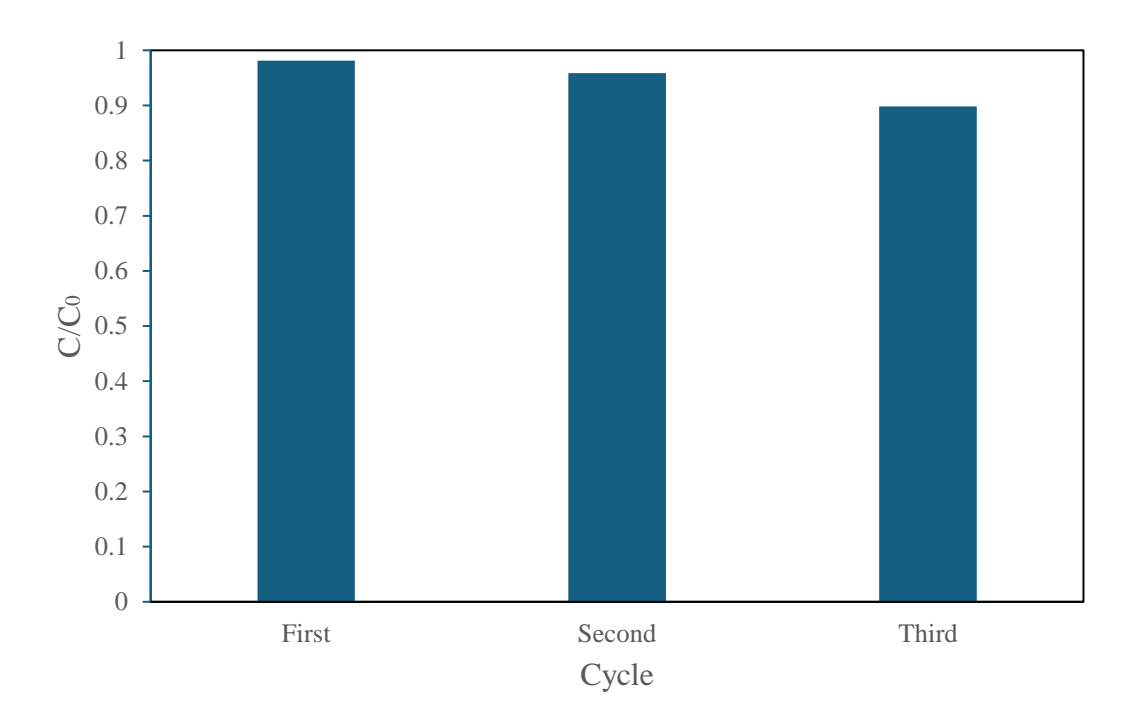


Figure 4.23: Result for Three Cycling Tests using 0.3GCN/BNO

#### 4.6 Charge Transfer Mechanism

The photocatalytic enhancement observed in the g-C<sub>3</sub>N<sub>4</sub>/BiNbO<sub>4</sub> heterostructure arises from a well-orchestrated transfer of photogenerated charge carriers between the two semiconductor components. Electrons in each material are excited from the valence band (VB) to the conduction band (CB), leaving behind positively charged holes. Whether these carriers recombine within their parent semiconductor or migrate across the interface determines the overall efficiency of the photocatalytic process.

To predict and rationalise this carrier movement, the band-edge potentials of each semiconductor at its point of zero charge must first be determined. Drawing upon established electrochemical relationships, the valence-band edge  $E_{VB}$  and conduction-band edge  $E_{CB}$  can be obtained using Eq. (4.2) and Eq. (4.3) as described by Sim et al. (2019):

$$E_{VB} = X - E_c + 0.5E_q \tag{4.2}$$

$$E_{CB} = E_{VB} - E_g \tag{4.3}$$

Where, X represents the absolute electronegativity of the semiconductor,  $E_c$  is the energy level of free electrons which is approximately 4.5 eV versus the normal hydrogen electrode (NHE), and  $E_g$  denotes the optical band-gap energy.

Literature values of electronegativity, namely X = 4.64 eV for g-C<sub>3</sub>N<sub>4</sub> and X = 6.26 eV for BiNbO<sub>4</sub>, enable direct calculation of their respective band positions (Chen et al., 2014; Lebedev et al., 2022). For g-C<sub>3</sub>N<sub>4</sub>, these equations yield a valence-band edge at 1.52 eV and a conduction-band edge at -1.23 eV. In contrast, the BiNbO<sub>4</sub> exhibits a more positive valence-band potential of 3.20 eV and a conduction-band edge of 0.33 eV. Since the conduction-band edge of g-C<sub>3</sub>N<sub>4</sub> lies at a more negative potential than that of BiNbO<sub>4</sub>, photogenerated electrons in g-C<sub>3</sub>N<sub>4</sub> readily transfer into the CB of BiNbO<sub>4</sub>. Simultaneously, holes in BiNbO<sub>4</sub> migrate into the VB of g-C<sub>3</sub>N<sub>4</sub> due to its lower VB potential. This spatial separation of electrons and holes dramatically reduces bulk recombination, prolongs carrier lifetimes, and ultimately enhances the catalytic degradation of target pollutants under light irradiation. Through this synergistic mechanism, the g-C<sub>3</sub>N<sub>4</sub>/BiNbO<sub>4</sub> heterostructure emerges as a highly effective photocatalyst.

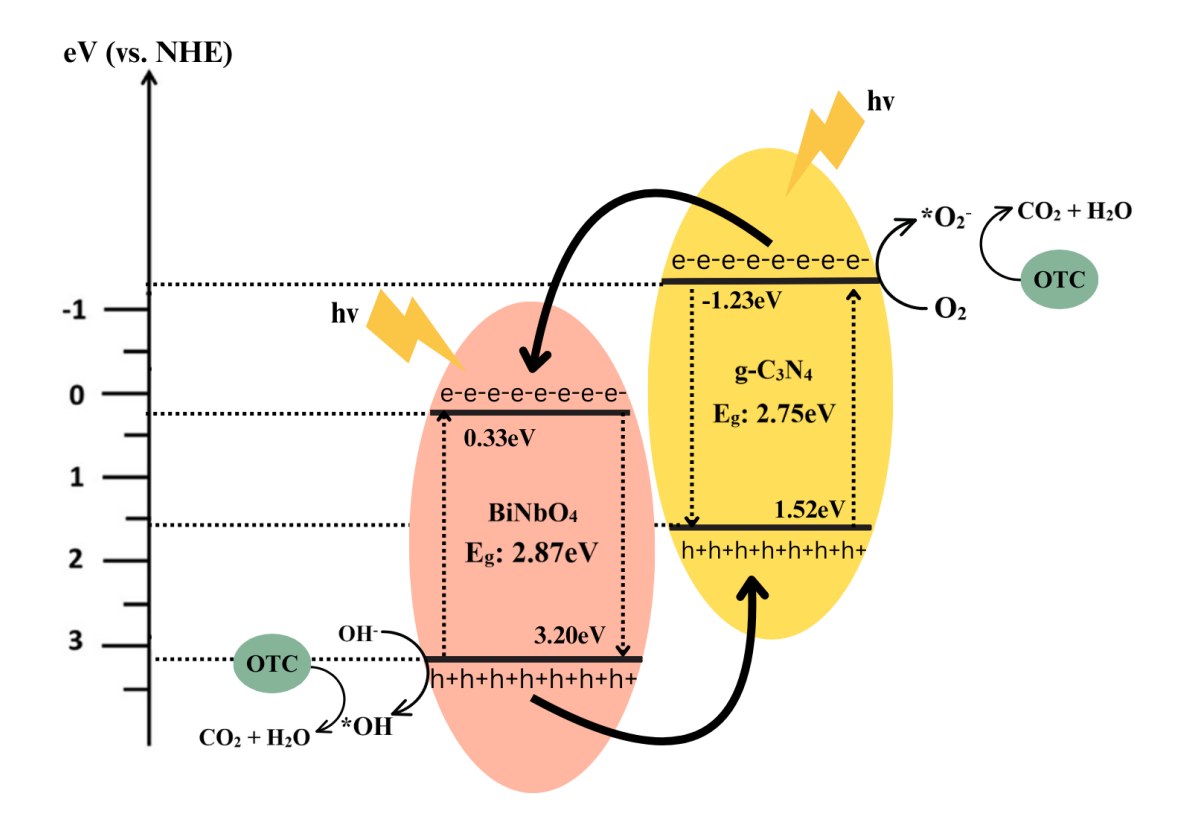


Figure 4.24: Schematic diagram of charge transfer in g-C<sub>3</sub>N<sub>4</sub>/BiNbO<sub>4</sub> heterostructures under visible light irradiation

### 4.7 Operational Cost Estimation

This section presents the cost estimation for synthesising g-C<sub>3</sub>N<sub>4</sub> and BiNbO<sub>4</sub> to assess the economic viability of using these materials for degrading persistent pollutants such as OTC.

The quantities required for each batch vary according to the g-C<sub>3</sub>N<sub>4</sub>/BiNbO<sub>4</sub> composite ratio. For example, when the target pollutant concentration is maintained at 20 ppm, 0.1 grams of photocatalyst are needed to preserve the appropriate ratio. In this study, the 0.5 GCN/BNO composite is produced using a ratio of 5 GCN to 10 BNO, while the 0.7 GCN/BNO composite requires a ratio of 7 GCN to 10 BNO. Consequently, the synthesis parameters for 0.1 grams of the 0.3 GCN/BNO composite are used to estimate the operational costs, as detailed in **Tables 4.1** and **4.2**.

Table 4.1: Cost Estimation of g-C<sub>3</sub>N<sub>4</sub> for synthesising 0.3GCN/BNO

Material	Unit	Price per unit (RM)	Total (RM)
Urea	1.0g	283.00/kg	0.283

Table 4.2: Cost Estimation of BiNbO<sub>4</sub> for synthesising 0.3GCN/BNO

Material	Unit	Price per unit (RM)	Total (RM)
Bismuth (III) Nitrate	0.125g	389.00/100g	0.486
Pentahydrate			
Niobium (V) oxide	0.0687g	331.00/25g	0.910
Ethylene glycol	1.6mL	656.00/L	1.050
Sodium Acetate	0.72g	78.00/kg	0.056
Anhydrous			
Polyethylene Glycol	0.2g	76.00/kg	0.015
		ТО	TAL 2.517

#### **CHAPTER 5**

#### **CONCLUSION**

#### 5.1 Conclusion

In summary, the synthesised 0.3 g-C<sub>3</sub>N<sub>4</sub>/BiNbO<sub>4</sub> heterojunction photocatalyst achieved a 98% removal efficiency of oxytetracycline (OTC) under solar irradiation. Given OTC's toxicity and its potential to harm human health and ecosystems, it is essential to develop an effective degradation method such as photocatalysis. Accordingly, this study prepared the g-C<sub>3</sub>N<sub>4</sub>/BiNbO<sub>4</sub> photocatalyst by physically mixing the two semiconductors, g-C<sub>3</sub>N<sub>4</sub> and BiNbO<sub>4</sub>.

Moreover, the composite's physical and chemical characteristics were thoroughly evaluated. Characterisation results confirmed the successful integration of both photocatalysts through analysis of microstructure and functional groups. Among all samples, the 0.3 g-C<sub>3</sub>N<sub>4</sub>/BiNbO<sub>4</sub> composite demonstrated the superior photocatalytic performance. Coupling with g-C<sub>3</sub>N<sub>4</sub> reduced BiNbO<sub>4</sub>'s band gap energy slightly from 2.87 eV to 2.85 eV. In addition, the heterojunction exhibited higher absorbance and extended light absorption into longer wavelengths, enhancing its ability to harness visible sunlight for photocatalysis. Finally, stability tests validated the composite's promise as an efficient photocatalyst for OTC degradation under solar irradiation. Therefore, all three objectives were successfully achieved.

#### 5.2 Recommendations

At the close of this work, several noteworthy insights have emerged that merit further exploration in future studies of g-C<sub>3</sub>N<sub>4</sub>/BiNbO<sub>4</sub>'s photocatalytic performance.

- 1) Exploring alternative synthesis routes such as hydrothermal synthesis followed by calcination for the bismuth niobate component could alter its structure in ways that either achieve full (100%) OTC removal within the same timeframe or match current degradation levels more rapidly.
- 2) Given its exceptional ability to degrade oxytetracycline, and likely other organic contaminants, g-C<sub>3</sub>N<sub>4</sub>/BiNbO<sub>4</sub> merits pilot-scale testing for industrial applications to gauge its real-world practicality.
- 3) Evaluate the effect of shortening the initial adsorption (dark) period from the current 24 hours down to 3–4 hours to significantly reduce total experimental time. This should include studying how a shorter dark phase influences pollutant adsorption equilibrium on the g-C<sub>3</sub>N<sub>4</sub>/BiNbO<sub>4</sub> surface and whether it still yields reliable photocatalytic degradation kinetic.
- 4) Investigate the photocatalytic performance of g-C<sub>3</sub>N<sub>4</sub>/BiNbO<sub>4</sub> under a range of pH values and temperatures and concurrently measure chemical oxygen demand (COD) removal efficiency, to determine its robustness across different water chemistries and its effectiveness at reducing overall organic load.

#### **REFERENCES**

- Alcântara, M.L., da Silva, J.S., Soares, R.O., Andrade, H.M.C., da Silva, L.A., Mascarenhas, A.J.S., 2018. Hydrothermal synthesis of bismuth niobates and their application in azo-dyes photo-discoloration. *Mater Res Bull*, 103, pp. 166–172. https://doi.org/10.1016/j.materresbull.2018.03.033
- American Water Chemicals., 2023. *Advanced Oxidation Processes*. Available at: https://www.membranechemicals.com/water-treatment/advanced-oxidation-plants/#:~:text=Advanced%20chemical%20oxidation%20processes%20make,to%20carbon%20dioxide%20and%20water. [Accessed 11 July 2024].
- Ameta, R., Solanki, M.S., Benjamin, S. and Ameta, S.C., 2018. Advanced Oxidation Processes for Waste Water Treatment Emerging Green Chemical Technology. Elsevier eBooks, [online], pp. 135–175. http://dx.doi.org/10.1016/B978-0-12-810499-6.00006-1
- Arikan, A., Sikora, L., Mulbry, W., Khan, S., Rice, C. and Foster, D., 2006. The fate and effect of oxytetracycline during the anaerobic digestion of manure from therapeutically treated calves. *Process Biochemistry*, 41 (3), pp. 1637–1643. http://dx.doi.org/10.1016/j.procbio.2006.03.010
- Balakrishnan, A., Chinthala, M., Polagani, R. K., & Vo, D. N., 2022. Removal of tetracycline from wastewater using g-C3N4 based photocatalysts: A review. *Environmental Research*, 216, p.114660. https://doi.org/10.1016/j.envres.2022.114660
- Bakiro M, Hussein Ahmed S, Alzamly A., 2019. Effect of pH, Surfactant, and Temperature on Mixed-Phase Structure and Band Gap Properties of BiNbO<sub>4</sub> Nanoparticles Prepared Using Different Routes. *Chemistry*, 1(1), pp. 89-110. https://doi.org/10.3390/chemistry1010008
- Bellamkonda, S., Shanmugam, R., Gangavarapu, R.R., 2019. Extending the π-electron conjugation in 2D planar graphitic carbon nitride: efficient charge separation for overall water splitting. *J. Mater. Chem.* A Mater 7, pp. 3757–3771. https://doi.org/10.1039/C8TA10580D.
- Boonsaner, M. and Hawker, D.W., 2010. Accumulation of oxytetracycline and norfloxacin from saline soil by soybeans. *Science of the Total Environment*, 408 (7), pp. 1731–1737. https://doi.org/10.1016/j.scitotenv.2009.12.032
- Bott, A.W., n.d. Electrochemistry of Semiconductors. Current Separation. Available at: http://www.currentseparations.com/issues/17-3/cs-17-3d.pdf [Accessed 21 Aug 2024]

- Cui, Y., Zhang, G., Lin, Z., Wang, X., 2016. Condensed and low-defected graphitic carbon nitride with enhanced photocatalytic hydrogen evolution under visible light irradiation. *Appl Catal B*, 181, pp. 413–419. https://doi.org/10.1016/j.apcatb.2015.08.018
- Chen, Y., Huang, W., He, D., Situ, Y., & Huang, H., 2014. Construction of Heterostructured g-C<sub>3</sub>N<sub>4</sub>/Ag/TiO<sub>2</sub> Microspheres with Enhanced Photocatalysis Performance under Visible-Light Irradiation. *ACS Applied Materials & Interfaces*, 6(16), pp. 14405–14414. https://doi.org/10.1021/am503674e
- Chang, J., Zhang, T., Qiu, S., Huang, N., Pang, D., Li, H., Masese, T., Zhang, H., Li, Z., & Huang, Z., 2023. Oxygenated Triazine-Heptazine Heterostructure Creates an Enormous Ascension to the Visible Light Photocatalytic Hydrogen Evolution Performance of Porous C<sub>3</sub>N<sub>4</sub> Nanosheets. *Small*, p.2301579. https://doi.org/10.1002/smll.202301579.
- Chidhambaram, N. and Ravichandran, K., 2017. Single step transformation of urea into metal-free g-C3N4 nanoflakes for visible light photocatalytic applications. Materials Letters, 207, pp. 44–48. https://doi.org/10.1016/j.matlet.2017.07.040.
- Christy, A.A., Kvalheim, O.M., Velapoldi, R.A., 1995. Quantitative analysis in diffuse reflectance spectrometry: A modified Kubelka-Munk equation. *Vibrational Spectroscopy* 9, pp. 19–27. https://doi.org/10.1016/0924-2031(94)00065-O
- Deng, Y., & Zhao, R., 2015. Advanced Oxidation Processes (AOPs) in Wastewater Treatment. *Current Pollution Reports*, *1*, pp. 167-176. https://doi.org/10.1007/s40726-015-0015-z
- Dong, F., Sun, Y., Wu, L., Fu, M., and Wu, Z., 2012. Facile transformation of low cost thiourea into nitrogen-rich graphitic carbon nitride nanocatalyst with high visible light photocatalytic performance. *Catal. Sci. Technol.* 2 (7), pp. 1332–1335. https://doi.org/ 10.1039/C2CY20049J.
- El Golli, A., Contreras, S., & Dridi, C., 2023. Bio-synthesized ZnO nanoparticles and sunlight-driven photocatalysis for environmentally friendly and sustainable route of synthetic petroleum refinery wastewater treatment. *Scientific reports*, 13(1), p.20809. https://doi.org/10.1038/s41598-023-47554-2
- Elia, A. C., Ciccotelli, V., Pacini, N., Dörr, A. J., Gili, M., Natali, M., Gasco, L., Prearo, M., & Abete, M. C., 2014. Transferability of oxytetracycline (OTC) from feed to carp muscle and evaluation of the antibiotic effects on antioxidant systems in liver and kidney. *Fish physiology and biochemistry*, 40(4), pp. 1055–1068. https://doi.org/10.1007/s10695-013-9905-4
- Fan, J., Shavel, A., Zamani, R., Fábrega, C., Rousset, J., Haller, S., Güell, F., Carrete, A., Andreu, T., Arbiol, J., Morante, J.R., Cabot, A., 2011. Control of the doping concentration, morphology and optoelectronic properties of vertically aligned chlorine-doped ZnO nanowires. Acta Materialia 59, pp. 6790–6800. https://doi.org/10.1016/j.actamat.2011.07.037
- Fang, J., Fan, H., Li, M., Long, C., 2015. Nitrogen self-doped graphitic carbon nitride as efficient visible light photocatalyst for hydrogen evolution. *J Mater Chem A Mater*, 3, pp. 13819–13826. https://doi.org/10.1039/C5TA02257F

- Feijoo, S., Yu, X., Kamali, M., Appels, L., & Dewil, R., 2023. Generation of oxidative radicals by advanced oxidation processes (AOPs) in wastewater treatment: a mechanistic, environmental and economic review. *Reviews in Environmental Science and Bio/Technology*, 22, pp. 205-248. https://doi.org/10.1007/s11157-023-09645-4
- Félicien Mazille and Dorothee Spuhler., 2020. *Advanced Oxidation Processes*. Available at: https://sswm.info/sswm-university-course/module-6-disaster-situations-planning-and-preparedness/further-resources-0/advanced-oxidation-processes [Accessed 11 July 2024].
- Fidan, Tuçe & Torabfam, Milad & Saleem, Qandeel & Wang, Chao & Kurt, Hasan & Yüce, Meral & Tang, Junwang & Bayazit, MK., 2021. Functionalized Graphitic Carbon Nitrides for Environmental and Sensing Applications. *Advanced Energy and Sustainability Research*, 2, p.2000073. https://doi.org/10.1002/aesr.202000073.
- Gao, W., Lu, J., Zhang, S., Zhang, X., Wang, Z., Qin, W., Wang, J., Zhou, W., Liu, H. and Sang, Y., 2019. Suppressing Photoinduced Charge Recombination via the Lorentz Force in a Photocatalytic System. *Advanced Science*, 6, p.1901244. https://doi.org/10.1002/advs.201901244.
- Goodarzi, N., Ashrafi-peyman, Z., Khani, E., & Moshfegh, A.Z., 2023. Recent Progress on Semiconductor Heterogeneous Photocatalysts in Clean Energy Production and Environmental Remediation. *Catalysts*. https://doi.org/10.3390/catal13071102
- Guerrini, M., Valencia, A., & Cocchi, C., 2021. Long-Range Order Promotes Charge-Transfer Excitations in Donor/Acceptor Co-Crystals. *The Journal of Physical Chemistry C.* https://doi.org/10.1021/acs.jpcc.1c06969.
- Hak, C.H., Leong, K.H., Chin, Y.H., Saravanan, P., Tan, S.T., Chong, W.C. and Sim, L.C., 2020. Water hyacinth derived carbon quantum dots and g-C<sub>3</sub>N<sub>4</sub> composites for sunlight driven photodegradation of 2,4-dichlorophenol. SN Applied Sciences, 2(6), p.1030. https://doi.org/10.1007/s42452-020-2840-y
- Ham, R., Nielsen, C. J., Pullen, S., & Reek, J. N. H., 2023. Supramolecular Coordination Cages for Artificial Photosynthesis and Synthetic Photocatalysis. *Chemical reviews*, 123(9), pp. 5225–5261. https://doi.org/10.1021/acs.chemrev.2c00759
- Hao, J., Wang, Q., Zhao, Z., 2017. Synthesis and characterization of g-C<sub>3</sub>N<sub>4</sub>/BiNbO<sub>4</sub> composite materials with visible light photocatalytic activity. J. Photochem. Photobiol. Chem. 335, pp. 94–101. https://doi.org/10.1016/j.jphotochem.2016.11.002.
- Hassanzadeh, P., Ganjidoust, H., Ayati, B., & Hogland, W., 2017. Focus on kinetices of removal antibiotics wastewater by nano-zero valent iron in oxidation and photoxidation process. *Linnaeus ECO-TECH*. https://doi.org/10.15626/ECO-TECH.2014.056
- Hong, J., Hwang, D. K., Selvaraj, R., Kim, Y., 2019. Facile synthesis of Br-doped g-C<sub>3</sub>N<sub>4</sub> nanosheets via one-step exfoliation using ammonium bromide for photodegradation of oxytetracycline antibiotics. *Journal of Industrial Engineering Chemistry*, 79, pp 473–481. https://doi.org/10.1016/j.jiec.2019.07.024

- Huang, M., Yang, Y., Chen, D., Chen, L. and Guo, H., 2011. Removal mechanism of trace oxytetracycline by aerobic sludge. *Process Safety and Environmental Protection*, 90 (2), pp. 141-146. https://doi.org/10.1016/J.PSEP.2011.08.008
- Hu, Z., Cai, X., Wang, Z., Li, S., Wang, Z. and Xie, X., 2019. Construction of carbondoped supramolecule-based g-C<sub>3</sub>N<sub>4</sub>/TiO<sub>2</sub> composites for removal of diclofenac and carbamazepine: A comparative study of operating parameters, mechanisms, degradation pathways. *Journal of Hazardous Materials*, 380. https://doi.org/10.1016/j.jhazmat.2019.120812.
- Ishak, N., Jeyalakshmi, V., Setka, M., Grandcolas, M., Devadas, B. and Miroslav, Š., 2023. Upgrading of g-C<sub>3</sub>N<sub>4</sub> semiconductor by a Nitrogen-doped carbon material: A photocatalytic degradation application. Journal of environmental chemical engineering, 11(2). https://doi.org/10.1016/j.jece.2023.109381.
- Jiang, Z., Zhang, X., Chen, H., Yang, P., & Jiang, S., 2020. Fusiform-Shaped g-C3 N4 Capsules with Superior Photocatalytic Activity. *Small*, p.2003910. https://doi.org/10.1002/smll.202003910.
- Jiao, J., Li, Y., Song, Q., Wang, L., Luo, T., Gao, C., Liu, L. and Yang, S., 2022. Removal of Pharmaceuticals and Personal Care Products (PPCPs) by Free Radicals in Advanced Oxidation Processes. *Materials*, 15(22). https://doi.org/10.3390/ma15228152.
- Kiran, K.S., Narayana, A., Lokesh, S.V., 2020. Synthesis of SrTiO<sub>3</sub> Nanotubes from Green TiO<sub>2</sub> Nanoparticles for Enhanced Photocatalytic Activity. *Asian Journal of Chemistry*, 32, pp. 2520–2528. https://doi.org/10.14233/ajchem.2020.22820
- Kuroda, K., & Kobayashi, J., 2020. Pharmaceuticals, Personal Care Products, and Artificial Sweeteners in Asian Groundwater: A Review. https://doi.org/10.1007/978-981-15-4599-3\_1
- Liang, Q., Li, Z., Huang, Z., Kang, F., Yang, Q., 2015. Holey Graphitic Carbon Nitride Nanosheets with Carbon Vacancies for Highly Improved Photocatalytic Hydrogen Production. Adv Funct Mater, 25, pp. 6885–6892. https://doi.org/10.1002/adfm.201503221
- Li, G., Zhang, D., Yu, J.C., Leung, M.K.H., 2010. An Efficient Bismuth Tungstate Visible-Light-Driven Photocatalyst for Breaking Down Nitric Oxide. *Environ Sci Technol*, 44, pp. 4276–4281. https://doi.org/10.1021/es100084a
- Li, J. and Wu, N., 2015. Semiconductor-based photocatalysts and photoelectrochemical cells for solar fuel generation: a review. *Catal. Sci. Technol.*, 5(3), pp. 1360–1384. https://doi.org/10.1039/C4CY00974F.
- Li, K., Yediler, A., Yang, M., Hostede, S. and Wong, M., 2008. Ozonation of oxytetracycline and toxicological assessment of its oxidation by-products. *Chemosphere*, 72 (2), pp. 473–478. https://doi.org/10.1016/j.chemosphere.2008.02.008
- Li, X., Zhang, J., Shen, L., Ma, Y., Lei, W., Cui, Q. and Zou, G., 2009. Preparation and characterization of graphitic carbon nitride through pyrolysis of melamine. *Appl. Phys.* A 94 (2) pp. 387–392. https://doi.org/10.1007/s00339-008-4816-4

- Li, Y., Wang, S., Guo, H., Zhou, J., Liu, Y., Wang, T., Yin, X., 2024. Synchronous removal of oxytetracycline and Cr(VI) in Fenton-like photocatalysis process driven by MnFe<sub>2</sub>O<sub>4</sub>/g-C<sub>3</sub>N<sub>4</sub>: Performance and mechanisms. *Chemosphere*, 352, p.141371. https://doi.org/10.1016/j.chemosphere.2024.141371.
- Liu J. F., Li, X.L. and Li, D. Y., 2003. Synthesis and characterization of nanocrystalline niobates. *Journal of Crystal Growth*, 247, pp. 419–424. https://doi.org/10.1016/S0022-0248(02)02015-8
- Liu, J., Zhang, T., Wang, Z., Dawson, G., Chen, W., 2011. Simple pyrolysis of urea into graphitic carbon nitride with recyclable adsorption and photocatalytic activity. *Journal of Material Chemistry*, 21, p. 14398. https://doi.org/10.1039/c1jm12620b
- Low, J., Cao, S., Yu, J., Wageh, S., 2014. Two-dimensional layered composite photocatalysts. Chemical Communications 50, p.10768. https://doi.org/10.1039/C4CC02553A
- Low, J., Yu, J., Jaroniec, M., Wageh, S. and Al-Ghamdi, A.A., 2017. Heterojunction Photocatalysts. *Advanced Materials*, 29(20), p.1601694. https://doi.org/https://doi.org/10.1002/adma.201601694.
- Luo, R., Zeng, W., Wu, Y., Jiang, W., Tang, B., Zhong, M., & Liu, Q., 2022. First-principles calculations on electronic, optical and photocatalytic properties of BiNbO<sub>4</sub>. *Materials Science in Semiconductor Processing*. https://doi.org/10.1016/j.mssp.2021.106391.
- Ma, J., Miao, T. J., & Tang, J., 2022. Charge carrier dynamics and reaction intermediates in heterogeneous photocatalysis by time-resolved spectroscopies. *Chemical Society reviews*, 51(14), pp. 5777–5794. https://doi.org/10.1039/d1cs01164b
- Madhura, L., Singh, S., Kanchi, S., Sabela, M.I., Bisetty, K., & Inamuddin., 2020. Removal of Targeted Pharmaceuticals and Personal Care Products from Wastewater Treatment Plants using QSAR Model. *Current Analytical Chemistry*. https://doi.org/10.2174/1573411016666200211093045
- Mahdi, R., Mohammed, E.H., Al-Keisy, A., Alsultan, M., Majid, W.H.A., 2022. Tailoring the morphology of BiNbO<sub>4</sub> of polymorph in 2D nanosheets for enhancement of photocatalytic activity in the visible range. *Physica E Low Dimens Syst Nanostruct*, 136, p.115009. https://doi.org/10.1016/j.physe.2021.115009
- Mahmoudi, K., Farzadkia, M., Rezaei Kalantary, R., Sobhi, H. R., Yeganeh, M., & Esrafili, A., 2024. Efficient removal of oxytetracycline antibiotic from aqueous media using UV/g-C<sub>3</sub>N<sub>4</sub>/Fe<sub>3</sub>O<sub>4</sub> photocatalytic process. *Heliyon*, *10*(9), p.30604. https://doi.org/10.1016/j.heliyon.2024.e30604
- Majumdar, A., Ghosh, U., Pal, A., 2021. Novel 2D/2D g-C<sub>3</sub>N<sub>4</sub>/Bi<sub>4</sub>NbO<sub>8</sub>Cl nanocomposite for enhanced photocatalytic degradation of oxytetracycline under visible LED light irradiation. *Journal of Colloid Interface Science*, 584, pp. 320–331. https://doi.org/10.1016/j.jcis.2020.09.101.
- Mamba, Gcina & Mishra, Ajay., 2016. Graphitic carbon nitride (g-C<sub>3</sub>N<sub>4</sub>) nanocomposites: A new and exciting generation of visible light driven photocatalysts for environmental pollution remediation. *Applied Catalysis B Environmental*, 198, pp. 347-377. https://doi.org/10.1016/j.apcatb.2016.05.052.

- Meera, A., Mahalakshmi, M., Jesintha, V., & Neppolian, B., 2024. The significant role of Z-scheme band alignment at the heterojunction for the enhanced photocatalytic H<sub>2</sub> production in TiO<sub>2</sub>/BiNbO<sub>4</sub>/rGO nanocomposite. *Journal of Solid State Chemistry*. https://doi.org/10.1016/j.jssc.2024.125030.
- Molina-Amaya, J.M., Ávila-Reyes, J.A., Delgado-Alvarado, E.A., González-Valdez, L.S., Torres-Ricario, R., Rojas-López, M., Almaraz-Abarca, N., & Gutiérrez-Velázquez, M.V., 2024. Potential of chitosan and activated carbon biocomposites for removing enrofloxacin and oxytetracycline from water. Revista Internacional de Contaminación Ambiental. https://doi.org/10.20937/rica.55051
- Pelosato, R., Bolognino, I., Fontana, F., & Sora, I. N., 2022. Applications of Heterogeneous Photocatalysis to the Degradation of Oxytetracycline in Water: A Review. *Molecules* (*Basel, Switzerland*), 27(9), p.2743. https://doi.org/10.3390/molecules27092743
- Rani, A., Lal, A. S., Saravanan, P. (2024). Bismuth niobate/g-C<sub>3</sub>N<sub>4</sub> heterojunction for maximised visible light photocatalytic removal of Bisphenol A. 364, p.143198. https://doi.org/10.1016/j.chemosphere.2024.143198.
- Sahoo, P., Sharma, A., Padhan, S., Udayabhanu, G., Thangavel, R. (2019). UV-assisted water splitting of stable Cl-doped ZnO nanorod photoanodes grown via facile solgel hydrothermal technique for enhanced solar energy harvesting applications. *Solar Energy*, 193, pp. 148–163. https://doi.org/10.1016/j.solener.2019.09.045
- Saravanan, R., Gracia, F., & Stephen, A., 2017. Basic Principles, Mechanism, and Challenges of Photocatalysis. In: D. and S.Y. Khan Mohammad Mansoob and Pradhan, ed. Nanocomposites for Visible Light-induced Photocatalysis. *Cham: Springer International Publishing*, pp. 19–40. https://doi.org/10.1007/978-3-319-62446-4 2.
- Schober, C., Reuter, K., & Oberhofer, H., 2016. Virtual Screening for High Carrier Mobility in Organic Semiconductors. *The journal of physical chemistry letters*, 7 19, pp. 3973-3977. https://doi.org/10.1021/ACS.JPCLETT.6B01657.
- Senasu, T., Lorwanishpaisarn, N., Hemavibool, K., Nijpanich, S., Chanlek, N., Nanan, S., 2022. 'Construction of g-C<sub>3</sub>N<sub>4</sub>/BiOCl/CdS heterostructure photocatalyst for complete removal of oxytetracycline antibiotic in wastewater', *Separation and Purification*Technology, 306, p.122735. https://doi.org/10.1016/j.seppur.2022.122735.
- Sponza, D.T., & Çelebi, H., 2012. Removal of oxytetracycline (OTC) in a synthetic pharmaceutical wastewater by sequential anaerobic multichamber bed reactor (AMCBR)/completely stirred tank reactor (CSTR) system: biodegradation and inhibition kinetics. *Journal of Chemical Technology & Biotechnology*, 87, pp. 961-975. https://doi.org/10.1002/JCTB.3706
- Shen, Y., Wu, Y., Xu, H., Fu, J., Li, X., Zhao, Q., Hou, Y., 2013. Facile preparation of sphere like copper ferrite nanostructures and their enhanced visible-light-induced photocatalytic conversion of benzene. *Material Research Bulletin* 48, pp. 4216–4222. https://doi.org/10.1016/j.materresbull.2013.06.063
- Shiraishi, Y., Kanazawa, S., Sugano, Y., Tsukamoto, D., Sakamoto, H., Ichikawa, S., Hirai, T., 2014. Highly Selective Production of Hydrogen Peroxide on Graphitic

- Carbon Nitride (g-C<sub>3</sub>N<sub>4</sub>) Photocatalyst Activated by Visible Light. *ACS Catal*, 4, pp. 774–780. https://doi.org/10.1021/cs401208c
- Sim, L. C., Koh, K. S., Leong, K. H., Chin, Y. H., Aziz, A. A., & Saravanan, P., 2019. In situ growth of g-C<sub>3</sub>N4 on TiO<sub>2</sub> nanotube arrays: Construction of heterostructures for improved photocatalysis properties. *Journal of Environmental Chemical Engineering*, 8(1), p.103611. https://doi.org/10.1016/j.jece.2019.103611
- Sun, S., Ding, J., Bao, J., Gao, C., Qi, Z., & Li, C., 2010. Photocatalytic Oxidation of Gaseous Formaldehyde on TiO<sub>2</sub>: An In Situ DRIFTS Study. *Catalysis Letters*, 137, pp. 239-246. https://doi.org/10.1007/S10562-010-0358-4.
- Tahara, S., Shimada, A., Kumada, N., Sugahara, Y., 2007. Characterization of Bi<sub>5</sub>Nb<sub>3</sub>O<sub>15</sub> by refinement of neutron diffraction pattern, acid treatment and reaction of the acid-treated product with n-alkylamines. J Solid State Chem 180, pp. 2517–2524. https://doi.org/10.1016/j.jssc.2007.05.017
- Tang, L., Zhou, S., Li, F., Sun, L., & Lu, H., 2023. Ozone Micronano-bubble-Enhanced Selective Degradation of Oxytetracycline from Production Wastewater: The Overlooked Singlet Oxygen Oxidation. *Environmental science & technology*, 57(47), pp. 18550–18562. https://doi.org/10.1021/acs.est.2c06008
- United Nations Department of Economic and Social Affairs (UN DESA)., 2023. The Sustainable Development Goals Report 2023: Special Edition. Available at: https://unstats.un.org/sdgs/report/2023/ [Accessed 20 Aug 2024]
- Vaizoğullar, A. I., 2019. ZnO/ZrO<sub>2</sub> composites: synthesis characterization and photocatalytic performance in the degradation of oxytetracycline antibiotic. *Materials Technology*, 34(8), pp. 433–443. https://doi.org/10.1080/10667857.2019.1574287.
- Wang, M., Jin C., Kang J., Liu J., Tang Y., Li Z., Li S., 2021. CuO/g-C<sub>3</sub>N<sub>4</sub> 2D/2D Heterojunction Photocatalysts as Efficient Peroxymonosulfate Activators Under Visible Light for Oxytetracycline Degradation: Characterization, Efficiency and Mechanism. *Chemical Engineering Journal*, 416, p.128118. https://doi.org/10.1016/j.cej.2020.128118.
- Wang, W., Tadé, M. O., & Shao, Z., 2015. Research progress of perovskite materials in photocatalysis- and photovoltaics-related energy conversion and environmental treatment. *Chemical Society reviews*, 44(15), pp. 5371–5408. https://doi.org/10.1039/c5cs00113g
- Wang, Z., Srivastava, V., Wang, S., Sun, H., Thangaraj, S.K., Jänis, J., and Sillanpää, M., 2020. UVC-assisted photocatalytic degradation of carbamazepine by Nd-doped Sb2O3/TiO2 photocatalyst. *Journal of Colloid and Interface Science*, 562, pp. 461–469. https://doi.org/10.1016/j.jcis.2019.11.094.
- Wee, W. Q., Sim, L. C., Leong, K. H., & Aziz, A. A., 2024. Integrated photocatalysis adsorption processes for oxytetracycline removal: using volborthite and its composite with g-C<sub>3</sub>N<sub>4</sub>. *Environmental science and pollution research international*, 10.1007/s11356-024-32802-3. Advance online publication. https://doi.org/10.1007/s11356-024-32802-3

- Xia, J., Dong, L., Song, H., Yang, J., & Zhu, X., 2023. Preparation of doped TiO2 nanomaterials and their applications in photocatalysis. *Bulletin of Materials Science*, 46, pp. 1-16. https://doi.org/10.1007/s12034-022-02847-6
- Xu, C., He, D., Liu, C., Wang, H., Zhang, L., Wang, P., Yin, S. (2013). High pressure and high temperature study the phase transitions of BiNbO<sub>4</sub>. *Solid State Commun*, 156, pp. 21–24. https://doi.org/10.1016/j.ssc.2012.11.007
- Xu, K., Yang, X., Ruan, L., Qi, S., Liu, J., Liu, K., Pan, S., Feng, G., Dai, Z., Yang, X., Li, R., & Feng J., 2020. Superior Adsorption and Photocatalytic Degradation Capability of Mesoporous LaFeO<sub>3</sub>/g-C<sub>3</sub>N<sub>4</sub> for Removal of Oxytetracycline. *Catalysts*, 10(3), e301. https://doi.org/10.3390/catal10030301
- Yan, S., Li, Z., Zou, Z., 2009. Photodegradation performance of g-C<sub>3</sub>N<sub>4</sub> fabricated by directly heating melamine, *Langmuir*, 25(17), pp. 10397–10401. https://doi.org/10.1021/la900923z.
- Yang, X., Zhang, H., Cheng, S., and Zhou, B., 2022. Optimization of the adsorption and removal of Sb(iii) by MIL-53(Fe)/GO using response surface methodology, *RSC Adv*, 12(7), pp. 4101-4112. http://dx.doi.org/10.1039/D1RA08169A
- Yang, Z., Li, J., Cheng, F., Chen, Z. and Dong, X., 2015. BiOBr/protonated graphitic C3N4 heterojunctions: intimate interfaces by electrostatic interaction and enhanced photocatalytic activity, *J. Alloy. Compd.* 634, pp. 215–222. https://doi.org/10.1016/j.jallcom.2015.02.103.
- Yentür, G. and Dükkancı, M., 2020. Synthesis of Visible-Light heterostructure photocatalyst of Ag/AgCl deposited on (040) facet of monoclinic BiVO<sub>4</sub> for efficient carbamazepine photocatalytic removal. *Applied Surface Science*, 531, p.147322. https://doi.org/https://doi.org/10.1016/j.apsusc.2020.147322.
- Yu C., Zhou W., Yu Jimmy C., Liu H., Wei L., 2014. Design and fabrication of heterojunction photocatalysts for energy conversion and pollutant degradation, *Chinese Journal of Catalysis*, 35(10), pp. 1609-1618. https://doi.org/10.1016/S1872-2067(14)60170-4.
- Yun-Ya Yang, Gurpal S. Toor and Alexander J. Reisinger., 2021. *Contaminants in the Urban Environment: Pharmaceuticals and Personal Care Products (PPCPs)—Part 2.* Available at: https://edis.ifas.ufl.edu/publication/SS633 [Accessed 11 July 2024].
- Zalfani, M., Hu, Z.-Y., Yu, W.-B., Mahdouani, M., Bourguiga, R., Wu, M., Li, Y., Van Tendeloo, G., Djaoued, Y., Su, B.-L, 2017. BiVO<sub>4</sub>/3DOM TiO<sub>2</sub> nanocomposites: Effect of BiVO<sub>4</sub> as highly efficient visible light sensitizer for highly improved visible light photocatalytic activity in the degradation of dye pollutants. *Applied Catalysis B. Environmental*, 205, pp. 121–132. https://doi.org/10.1016/j.apcatb.2016.12.019
- Zanetti, S., Silva, S.A.D., and Thim, G.P.A., 2004. A chemical route for the synthesis of cubic bismuth zinc niobate pyrochlore nanopowders. *Journal of Solid State Chemistry*, 177, pp. 4546–4551. https://doi.org/10.1016/j.jssc.2004.09.001
- Zhai, H.-F., Qian, X., Kong, J.-Z., Li, A.-D., Gong, Y.-P., Li, H., Wu, D., 2011. Abnormal phase transition in BiNbO4 powders prepared by a citrate method. *J*

- *Alloys Compd*, 509, pp. 10230–10233. https://doi.org/10.1016/j.jallcom.2011.08.077
- Zhang, H., Zuo, X., Tang, H., Li, G., Zhou, Z., 2015. Origin of photoactivity in graphitic carbon nitride and strategies for enhancement of photocatalytic efficiency: insights from first principles computations. *Physical Chemistry Chemical Physics*, 17, pp. 6280–6288. https://doi.org/10.1039/C4CP05288A
- Zhang, S., Zhao, S., Huang, S., Hu, B., Wang, M., Zhang, Z., He, L., Du, M., 2021. Photocatalytic degradation of oxytetracycline under visible light by nanohybrids of CoFe alloy nanoparticles and nitrogen-/sulfur-codoped mesoporous carbon. *Chemical Engineering Journal*, 420, p.130516. https://doi.org/10.1016/j.cej.2021.130516
- Zhang, Z., Jiang, D., Li, D., He, M., Chen, M., 2016. Construction of SnNb<sub>2</sub>O<sub>6</sub> nanosheet/g-C<sub>3</sub>N<sub>4</sub> nanosheet two-dimensional heterostructures with improved photocatalytic activity: Synergistic effect and mechanism insight. *Appl Catal B*, 183, pp. 113–123. https://doi.org/10.1016/j.apcatb.2015.10.022
- Zhao, C., Zhou, Y., D.J. de Ridder, Zhai, J., Wei, Y., Deng, H., 2014. Advantages of TiO<sub>2</sub>/5A composite catalyst for photocatalytic degradation of antibiotic oxytetracycline in aqueous solution: comparison between TiO<sub>2</sub> and TiO<sub>2</sub>/5A composite system. *Chemical Engineering Journal*, 248, pp. 280–289. https://doi.org/10.1016/j.cej.2014.03.050
- Zhu, B., Zhang, L., Cheng, B., Yu, Y., & Yu, J., 2021. H<sub>2</sub>O molecule adsorption on striazine-based g-C<sub>3</sub>N<sub>4</sub>. *Chinese Journal of Catalysis*. https://doi.org/10.1016/s1872-2067(20)63598-7.

## **APPENDICES**

## APPENDIX A: Tables

Table 5.1: g-C $_3$ N $_4$  based heterojunction for the removal of tetracycline (Balakrishnan et al., 2022)

Catalyst	Synthesis method	Type	Initial concentration	Light source	Efficiency (%)	Reference
g-C <sub>3</sub> N <sub>4</sub> /TiO <sub>2</sub> /carbon fiber	Hydrothermal	S-scheme	-	Xenon lamp	99.9% in 90	Guo et al., 2021b
$Ti_{0.7}Sn_{0.3}O_2/g$ - $C_3N_4$	Thermal polymerization and solvothermal method	S-scheme	20 mg/L	1.5Watt Light emitting diode lamp	88.3% in 40 min	Guo et al. (2022)
BiOl exfoliated g-C <sub>3</sub> N <sub>4</sub>	Thermal exfoliation and chemical precipitation	Z-scheme	20 mg/L	500 Watt xenon lamp	86% in 30 min	Liu et al., 2022a
$\mathrm{Bi}_2\mathrm{O}_2\mathrm{CO}/\mathrm{g}\text{-}\mathrm{C}_3\mathrm{N}_4/\mathrm{Bi}_2\mathrm{O}_3$	Precipitation-calcination	Z-scheme	10 mg/L	300 Watt xenon lamp	>80% in 60 min	Wu et al., 2022a
g-C <sub>3</sub> N <sub>4</sub> /Biochar/Bi <sub>25</sub> FeO <sub>40</sub>		Z-scheme	20 mg/L	300 Watt xenon lamp	92.2% in 60 min	Ma et al. (2022)
WO@ g-C <sub>3</sub> N <sub>4</sub> @ Multi walled carbon nanotubes	Simple low temperature hydrothermal	Z-scheme	20 mg/L	500 Watt halogen lamp	79.54% in 120 min	Manikandan et al. (2022)
NiCo <sub>2</sub> O <sub>4</sub> /S-c-doped one dimensional g-C <sub>3</sub> N <sub>4</sub>	Hydrothermal pyrolysis	Z-scheme	10 mg/L	300 Watt xenon lamp	99% in 60 min	Nguyen et al. (2022b)
Ag–InVO <sub>4</sub> /g-C <sub>3</sub> N <sub>4</sub>	Hydrothermal	Z-scheme	10 mg/L	30 Watt bulb	>90%	Thanh Tung et al. (2022)
(BiO) <sub>2</sub> CO/ZnFe-Layered Double Hydroxides	Simple hydrothermal	Z-scheme	15 mg/L	Visible light	98% in 120 min	Wang et al. (2022
Ag/AgVO <sub>4</sub> /g-C <sub>3</sub> N <sub>4</sub>	Surface imprinting and photo- induced polymerization	Z-scheme eme	20 mg/L	Ultraviolet lamp	>75%	Sun et al. (2019)
g-C <sub>3</sub> N <sub>4</sub> /CdS	Self-assembly method	Z-scheme	50 mg/L	35 Watt xenon lamp	_	Li et al., 2019a
AgPO <sub>4</sub> /N-graphene/g-C <sub>3</sub> N <sub>4</sub>	In-situ deposition	Z-scheme	20 mg/L	100 Watt xenon lamp	93% in 90 min	Zhang et al. (2019
MnO <sub>2</sub> /Mn-modified alkalinized g-C <sub>3</sub> N <sub>4</sub>	Calcination-impregnation	Z-scheme	10 mg/L	300 Watt xenon lamp	96.7% in 120 min	Zhang et al., 2020
Ag <sub>3</sub> PO <sub>4</sub> /AgBr/g-C <sub>3</sub> N <sub>4</sub>	Facile chemical deposition	Z-scheme	40 mg/L	300 Watt xenon lamp	80.2% in 25 min	Yu et al. (2020)
Carbon dots modified MoO/g- C <sub>3</sub> N <sub>4</sub>	Facile calcination	Z-scheme	20 mg/L	350 Watt xenon lamp	88.4% in 90 min	Xie et al. (2018)
g-C <sub>3</sub> N <sub>4</sub> /MnO <sub>2</sub> /Graphene oxide	Facile wet chemical	Z-scheme	10 mg/L	Visible light	91.4% in 60 min	Du et al. (2021)
AgPO <sub>4</sub> /g-C <sub>3</sub> N <sub>4</sub> /ZnO	Ultrasound assisted precipitation	Z-scheme	30 mg/L	45 Watt visible lamp	88.47% in 120 min	Zhu et al. (2020)
2D/2D CuInS <sub>2</sub> /g-C <sub>3</sub> N <sub>4</sub>	Facile solvothermal	Z-scheme	20 mg/L	300 Watt xenon lamp	83.7% in 60 min	Guo et al. (2019b)
g-C <sub>3</sub> N <sub>4</sub> /NaBiO	Facile hydrothermal	Z-scheme	-	300 Watt xenon lamp	>85% in 30 min	Wu et al. (2021b)
2D/2D BiOCl/g-C <sub>3</sub> N <sub>4</sub>	Simple hydrothermal	Z-scheme	20 mg/L	300 Watt xenon lamp	97% in 60 min	Sun et al. (2020)
g-C <sub>3</sub> N <sub>4</sub> /Bi <sub>2</sub> WO <sub>6</sub> /AgI	Hierarchial assembly	Z-scheme	20 mg/L	300 Watt xenon lamp	91.13% in 60 min	Xue et al. (2019)
g-C <sub>3</sub> N <sub>4</sub> /LaFeO	Electrostatic attraction method	Z-scheme	10 mg/L	300 Watt xenon lamp	~95% in 120 min	Zhang et al. (2021b)

Table 5.2: Comparison of OTC degradation by using various photocatalyst (Senasu et al., 2022)

Catalyst	Conc.	Catalyst loading	Light source	Lamp	Time (min)	Degradation (%)	Ref.
g-C <sub>3</sub> N <sub>4</sub>	10 mgL <sup>-1</sup>	50 mg	Visible	300 W xenon lamp	50	33.9	[12]
g-C <sub>3</sub> N <sub>4</sub>	10 mgL <sup>-1</sup>	40 mg/L	Visible	500 W xenon lamp	60	30.8	[50]
g-C <sub>3</sub> N <sub>4</sub>	10 mgL <sup>-1</sup>	25 mg	Visible	300 W xenon lamp	120	31.0	[73]
g-C <sub>3</sub> N <sub>4</sub>	15 mgL <sup>-1</sup>	60 mg	Visible	500 W xenon lamp	150	45.0	[76]
CdS	20 mgL <sup>-1</sup>	25 mg	Simulated sunlight	500 W xenon lamp	60	65.0	[28]
BiOCl	20 mgL <sup>-1</sup>	25 mg	Simulated sunlight	500 W xenon lamp	60	60.0	[28]
BiOCl	20 mgL <sup>-1</sup>	_	Visible	300 W xenon lamp	180	65.0	[45]
TiO <sub>2</sub>	10 mgL <sup>-1</sup>	25 mg	Visible	300 W xenon lamp	120	3.58	[73]
TiO <sub>2</sub> nanoflowers	0.5 mgL <sup>-1</sup>	10 mg	Sunlight	-	60	80.0	[78]
Br-doped g-C <sub>3</sub> N <sub>4</sub>	10 mgL <sup>-1</sup>	250 mg	Visible	LED 38.5 W	75	75.0	[3]
g-C <sub>3</sub> N <sub>4</sub> /Bi <sub>4</sub> NbO <sub>8</sub> Cl	20 mgL <sup>-1</sup>	10 mg	Visible	LED 18 W	60	87.0	[4]
ZnO/g-C <sub>3</sub> N <sub>4</sub>	10 mgL <sup>-1</sup>	20 mg	Visible	300 W xenon lamp	50	63.5	[11]
BPC/g-C <sub>3</sub> N <sub>4</sub> *	10 mgL <sup>-1</sup>	50 mg	Visible	300 W xenon lamp	150	84.0	[12]
BiOCl-CdS	20 mgL <sup>-1</sup>	25 mg	Simulated sunlight	500 W xenon lamp	60	83.7	[28]
BiOCl/TiO <sub>2</sub>	20 mgL <sup>-1</sup>	50 mg	Visible	300 W xenon lamp	120	48.0	[43]
BiOCl/RGO *	20 mgL <sup>-1</sup>	-	Visible	300 W xenon lamp	180	93.3	[45]
WO <sub>3</sub> /g-C <sub>3</sub> N <sub>4</sub>	10 mgL <sup>-1</sup>	40 mg/L	Visible	500 W xenon lamp	60	84.2	[50]
BP/g-C <sub>3</sub> N <sub>4</sub> *	10 mgL <sup>-1</sup>	30 mg	Visible	300 W xenon lamp	60	81.0	[70]
TiO <sub>2</sub> /g-C <sub>3</sub> N <sub>4</sub>	10 mgL <sup>-1</sup>	25 mg	Visible	300 W xenon lamp	120	92.8	[73]
g-C <sub>3</sub> N <sub>4</sub> /NiFe <sub>2</sub> O <sub>4</sub>	46 mgL <sup>-1</sup>	500 mg	Sunlight	-	60	97.0	[74]
Ag/g-C <sub>3</sub> N <sub>4</sub>	30 mgL <sup>-1</sup>	100 mg	Visible	300 W xenon lamp	120	81.0	[77]
CdS/TiO <sub>2</sub>	40 mgL <sup>-1</sup>	50 mg	Visible	300 W xenon lamp	50	81.0	[47]
NiCo/ZnO/g-C <sub>3</sub> N <sub>4</sub>	10 mgL <sup>-1</sup>	20 mg	Visible	300 W	50	71.3	[5]
N-ZnO/CdS/GO	20 mgL <sup>-1</sup>	50 mg	Visible	300 W xenon lamp	50	60.0	[46]
Ag/WO <sub>3</sub> /g-C <sub>3</sub> N <sub>4</sub>	10 mgL <sup>-1</sup>	40 mg/L	Visible	500 W xenon lamp	60	97.7	[50]
GO/Ag <sub>2</sub> CrO <sub>4</sub> /g-C <sub>3</sub> N <sub>4</sub>	10 mgL <sup>-1</sup>	20 mg	Visible	300 W xenon lamp	90	94.2	[75]
Au/g-C <sub>3</sub> N <sub>4</sub> /CeO2	15 mgL <sup>-1</sup>	60 mg	Visible	500 W xenon lamp	150	88.0	[76]
CT/Bi <sub>2</sub> O <sub>3</sub> /BiOCl *	46 mgL <sup>-1</sup>	50 mg	Sunlight	_	120	90.0	[79]
GSC/Bi <sub>2</sub> O <sub>3</sub> /BiOCl *	46 mgL <sup>-1</sup>	50 mg	Sunlight	_	120	86.0	[79]
g-C <sub>3</sub> N <sub>4</sub> /BiOCl/CdS	10 mgL <sup>-1</sup>	50 mg	Visible	15 W	240	87.2	This wo
g-C <sub>3</sub> N <sub>4</sub> /BiOCl/CdS	10 mgL <sup>-1</sup>	50 mg	Sunlight	_	240	99.3	This wo

 $<sup>^{*}\</sup> RGO = reduced\ graphene\ oxide;\ BP = black\ phosphorus;\ BPC = Biomass\ porous\ carbon;\ CT = chitosan;\ GSC = graphene-sand\ composite.$ 

# APPENDIX B: Figures



Figure 5.1: Synthesis of g-C<sub>3</sub>N<sub>4</sub> from urea using calcination method

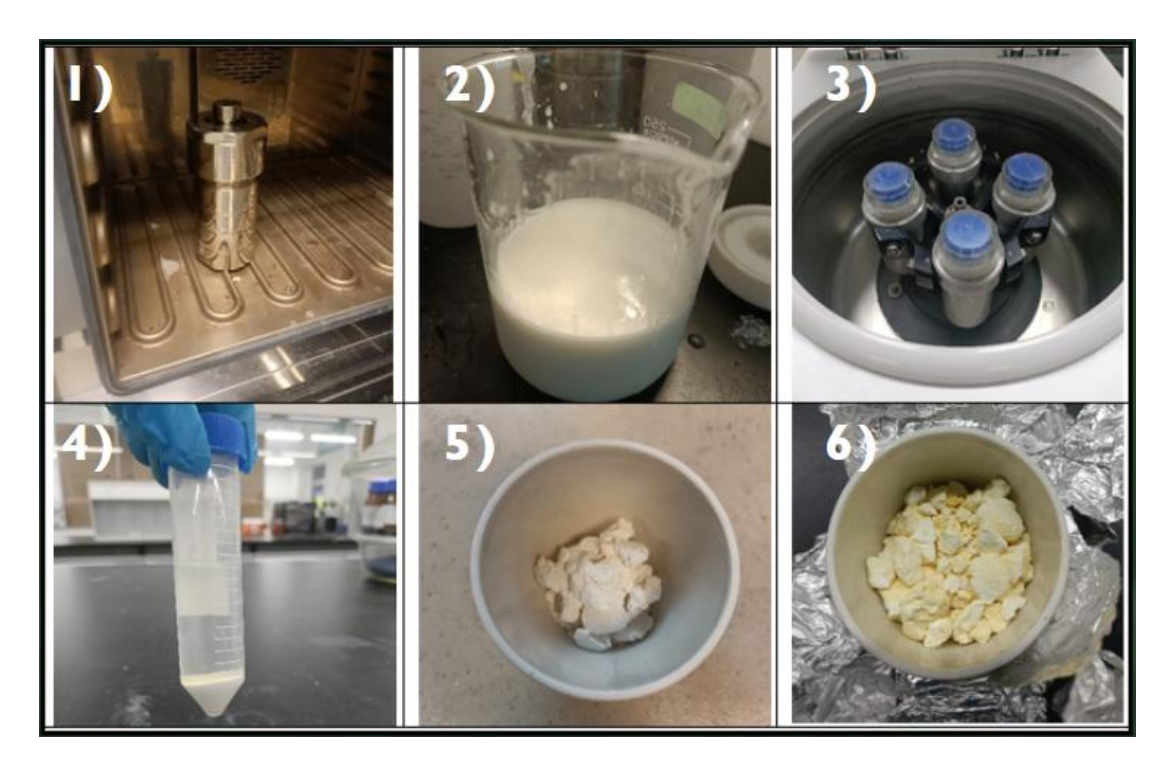


Figure 5.2: Synthesis of BiNbO4 using simple solvothermal method



Figure 5.3: Coupling of g-C3N4 and BiNbO4 using simple physical mixing method